Computational Analysis of Photon Echo and Exceptional Points Dynamics in Lossy Quantum Systems

by

Sharad Joshi

Submitted in conformity with the requirements
for the degree of Doctor of Philosophy in Physics

School of Engineering & Physical Sciences

Submitted December, 2019

Abstract

The focus of this thesis is investigating regimes where experimental realisations of theoretical hypothesis is difficult. Mainly we investigated three topics. Firstly, Photon echo in overlapping pulses regime. We showed that for overlapping carrier enveloped pulses the echo peak position is sensitive to the relative phase and depends on delay between the pulses, pulse width, dephasing times etc of the overlapping pulses. We also showed that observing the photon echo in such a regime is easier when the pulses interfere destructively as the echo signal is relatively stronger although echo peak position shifted forward in time more than constructive interference case.

Secondly, an experiment of electromagnetically induced transparency in silicon with shallow donors. In this case we explained what went wrong with this experiment and suggested a parameter regime where EIT can be observed experimentally. We also briefly explored a three-level system with losses using non-hermitian quantum mechanics and reproduced some general results(coherent population trapping, effect of loss on different state populations in a three level system) of a hermitian hamiltonian using non-hermitian hamiltonian.

Thirdly, we investigated non-hermitian quantum mechanics using two and four level systems. We observed the general properties of exceptional points namely, non-hermitian degeneracy where both the eigenvalues and the eigenvectors coalesce thus leaving the hamiltonian matrix defective, phase rigidity, topological properties and differences between encircling exceptional points quasi-statically and dynamically. We then suggested experiments to observe these exceptional points, investigated exceptional rings, compared symmetric and asymmetric non-hermitian hamiltonians with identical eigenvalues and found a regime where no matter how small the gain it always wins against loss.

Acknowledgements

I would like to thank my mentor Prof. Ian Galbraith for guiding me throughout and being patient with me while I wrote this thesis. I would also like to thank him for giving me suggestions for new projects and at the same time the complete freedom to choose a topic of my own interest. I have learnt a lot from him ranging from studies to sports. I would like to thank my wife Smriti Ajit for supporting, believing and being there for me throughout the whole process. Without her support I wouldn't be able to start or finish this journey. I would also like to thank my Parents, In-laws, Brother, Brother-in-law, Sister and Shanvi for always supporting me and believing in me. I would like to thank my friends Siddharth, Tanuj, Robert, Klaudia, Vikram, Punya, Anuja and others for making each day bright and eventful. I would also like to thank all my friends in squash club, tennis club and volleyball club for providing me the opportunity to play competitively which provided the much needed stress relief every week. In the end I would like to thank CDT/EPSRC and Heriot-Watt University for providing the funding, facilities and environment to pursue my interest and resulted in this thesis.

ACADEMIC REGISTRY

Research Thesis Submission

Please note this form should be bound into the submitted thesis.

Name:	Sharad Joshi		
School:	School of Engineering and Physics		
Version: *(i.e. First, Resubmission, Final)*	Final	Degree Sought:	PhD

Declaration

In accordance with the appropriate regulations I hereby submit my thesis and I declare that:

1. The thesis embodies the results of my own work and has been composed by myself
2. Where appropriate, I have made acknowledgement of the work of others
3. Where the thesis contains published outputs under Regulation 6 (9.1.2) these are accompanied by a critical review which accurately describes my contribution to the research and, for multi-author outputs, a signed declaration indicating the contribution of each author (complete Inclusion of Published Works Form – see below)
4. The thesis is the correct version for submission and is the same version as any electronic versions submitted*.
5. My thesis for the award referred to, deposited in the Heriot-Watt University Library, should be made available for loan or photocopying and be available via the Institutional Repository, subject to such conditions as the Librarian may require
6. I understand that as a student of the University I am required to abide by the Regulations of the University and to conform to its discipline.
7. Inclusion of published outputs under Regulation 6 (9.1.2) shall not constitute plagiarism.
8. I confirm that the thesis has been verified against plagiarism via an approved plagiarism detection application e.g. Turnitin.

* *Please note that it is the responsibility of the candidate to ensure that the correct version of the thesis is submitted.*

Signature of Candidate:		Date:	

Submission

Submitted By *(name in capitals):*	Sharad Joshi
Signature of Individual Submitting:	
Date Submitted:	

For Completion in the Student Service Centre (SSC)

Received in the SSC by *(name in capitals):*			
Method of Submission *(Handed in to SSC; posted through internal/external mail):*			
*E-thesis Submitted (**mandatory for final theses**)*			
Signature:		Date:	

Research Thesis Submission Form

ACADEMIC REGISTRY

Inclusion of Published Works

Declaration

This thesis contains one or more multi-author published works. In accordance with Regulation 6 (9.1.2) I hereby declare that the contributions of each author to these publications is as follows:

Citation details	Sharad Joshi and Ian Galbraith, Exceptional points and dynamics of an asymmetric non-Hermitian two-level system, Physical Review A, 98,4, 042117 (2018)
Author 1	Researcher
Author 2	Primary Supervisor
Signature:	
Date:	

Citation details	Sharad Joshi, Carl R. Pidgeon, Ben N Murdin and Ian Galbraith, Phase control of photon echo dynamics with overlapping pulse pairs, Physical Review A, 95, 013416 (2017)
Author 1	Researcher
Author 2	Collaborator/Supervisor : Useful discussions/guidance on the topic at hand.
Author 3	Collaborator/Supervisor : Useful discussions/guidance on the topic at hand.
Author 4	Primary Supervisor
Signature:	
Date:	

Contents

List of Publications

1. Exceptional points and dynamics of an asymmetric non-Hermitian two-level system
   Joshi, Sharad and Galbraith, Ian
   Physical Review A **98** 4 042117, 2018

2. Phase control of photon-echo dynamics with overlapping pulse pairs,
   Joshi, Sharad, Pidgeon, Carl R, Murdin, Ben N and Galbraith, Ian
   Physical Review A **95** 013416, 2017

Chapter 1

Introduction/Motivation

1.1 Introduction

Rolf Landauer stated that "information is physical"[1]. Since physics as we know now is quantum in nature it is obvious to try to study information processing tasks using principles of quantum mechanics. This led to the birth of quantum computation and information devoted to a big dream of realizing quantum computers which are more powerful and efficient than their classical counterparts. Here efficient means if the problem can be solved in polynomial time using polynomial resources.
Divincenzo gave five necessary and sufficient criteria for a system to be a scalable quantum computer [2] -

1. Identification of well-defined qubits.
2. Reliable state preparation.
3. High coherence time (low decoherence).
4. Accurate quantum logical gate operations.
5. Good quantum measurements(strong).

These criteria were given in the context of a semiconductor-based quantum computer(spins of free electrons confined in quantum dots are suggested as qubit candidates) but are applicable to any general scheme of quantum computing, namely, NMR, ion traps, SQUIDS, optics and photons, optical cavities etc. Many quantum systems are shown to satisfy several (not all) of these criteria. Silicon based quantum computing is a regime where researchers are trying to use the nuclear and electronic spins of donor atoms(phosphorus,

bismuth etc) in a silicon crystal to build a scalable quantum computer. The idea of using donors in silicon was first introduced by Kane in 1998 [3] where he suggested to use silicon nuclear spins and the donor(phosphorus) atom's electron/nuclear spins to make a scalable quantum computer. Fig. 1.1 shows a high level schematic of a Kane quantum computer.

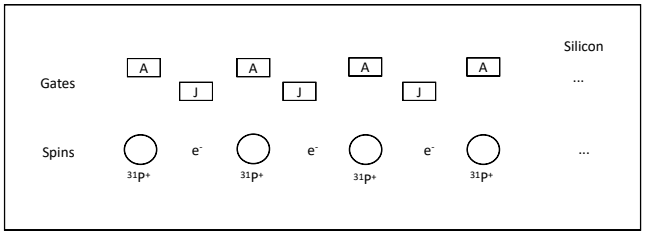

Figure 1.1: Schematic of a Kane quantum computer - phosphorous donor in silicon. The interaction between neighbouring nuclear spins is mediated using the electronic spins of the donor. The "A gates " control the resonance frequency of the nuclear spins while the "J gates" control the electron mediated interaction. Since each qubit as well as two qubit operation is individually controlled by the relevant gates, this system in principle is scalable to arbitrary number of qubits

In principle, this system is scalable to arbitrary number of qubits due to each the ability to individually address each qubit electrically. Fig. As there is no significant interaction with the neighbouring nuclear spins and we need two qubit operations, the donor electron spin was introduced to mediate that interaction. The spin of the extra electron of the donor atom can be used to encode the qubits. This method has two advantages :

1. Long coherence times. It has been shown that these hybrid systems(nuclear-electronic qubits) have long coherence times(4ms which is five orders of magnitude longer).[4] compared to pure nuclear states based systems.

2. It is scalable due to the fact that the qubits can be addressed individually by using lasers.

Because of these properties, shallow donors in semiconductors are a good candidate for the practical implementation of a solid-state quantum computer. This kind of system has a wide range of applications including quantum memories, magnetometers, atomic clocks,

coherent population trapping, quantum logical gates[5] etc.

Superconducting qubits are one of the most promising candidates for quantum computers due to their fast operation capabilities and ease of scalability [6]. But they have the big drawback of having high decoherence i.e. the system might not remain coherent during the time of computation, which will lead to errors. One solution to this problem is the use of quantum memories to support the superconducting qubits. Any good candidate for quantum memory must have the property of addressability at low magnetic field($<$ mT) [7] because of the critical field limitation of superconductors. A good candidate for this purpose is bismuth donors in silicon as they have a zero-field splitting of around 7.4 GHz which is comparable to the energy splitting of $|R\rangle$ and $|L\rangle$ states of superconducting flux qubits. Therefore these two can be coupled via a microwave photon[8]. The Si:Bi system has been extensively researched in the last 5 years including the spectroscopic analysis of electron paramagnetic resonance(EPS), electron spin relaxation time, decoherence time, super-hyperfine interaction between silicon nuclei and bismuth electrons, EPR cancellation resonances etc [9],[10],[11].

The coherent interaction of atoms with external radiation, primarily laser light has applications in physics, chemistry, electronics, information processing etc. The ability to control the transitions between the discrete energy levels of the atoms and briefly alter their structure has potential in many fields. One application of the coherent interaction of laser with donors in semiconductors is atomic clocks[12] where we can use the hyperfine splitting levels(Si:P system) to create a lambda atomic scheme. Using the phenomenon of coherent population trapping[13](accomplished by using two laser radiation fields), we can create an atomic ensemble in a desired state, together with resonant excitation. Ramsey improved Rabi's method of measuring transition frequencies by proposing that instead of using single long π pulse if we use two short $\pi/2$ pulses separated by a non-interaction period we will get a much better precision during measurement. This is advantageous because in Ramsey's case the ensemble of atoms interacts with the pulse for a very short time, thus reducing the errors due to inhomogeneities. Ramsey's method is used today in atomic clocks which in turn are used in timekeeping the definition of second because no mechanical or electric clocks are precise enough for a long enough time to maintain the definition of a second. Another potential application of this is making highly resolved magnetometers. Nitrogen vacancy centres in diamonds are being studied for this purpose [14]. A magnetometer is a device which is used to measure the strength of a magnetic

field, in some cases the direction and also the magnetisation of a magnetic material. The position(in time) of a photon echo might be used to measure the strength of the applied magnetic field because of Zeeman splitting and that's why Chapter 3 is dedicated to the theory of 3-level systems where we investigate an experiment on electromagnetically induced transparency(EIT) by our collaborators using donors in semiconductors. We explained why the particular experiment was not successful and suggested some guidelines to observe EIT in their system.

There are two ways to model laser interaction with a system with losses in the form of population decay or polarisation decay. One is to describe a hermitian system, derive the optical Bloch equations and add losses in the system phenomenologically. This set of coupled ordinary differential equations will then describe the system dynamics. Another way is to start with a non-hermitian system by encoding the losses directly in the hamiltonian and derive the optical Bloch equations as usual. This results in the same set of equations as the former method but the physics can be different due to the extension of the parameter space to the complex from the real domain. This leads to different properties of eigenvectors and eigenvalues. In non-hermitian quantum mechanics the eigenvalues can be complex where the real part is interpreted as the energy of and the imaginary part the loss/gain from that particular state. The nature of degeneracy in a non-hermitian system is significantly different than hermitian systems. Unlike hermitian system where the eigenvalues coalesce but the eigenvectors remain orthogonal, here the eigenvalues as well as the eigenvectors coalesce leaving a defective matrix. This results in interesting topological properties around the degeneracy which we explore in chapter 4. A detailed introduction to non-hermitian quantum mechanics is included in Chapter 4.

This thesis focuses on analytically and numerically understanding the dynamics of the systems by investigating optical phenomena like photon echo (automatic revival of the initial signal after some time), electromagnetically induced transparency (conversion of a three level opaque system to transparent system in the presence of appropriate laser interactions) in difficult to realize regimes and understanding the impact of non-hermitian quantum mechanics on real two and four level systems interacting with lasers.

This thesis can be divided into 3 core parts :

1. Photon echo

2. Electromagnetically induced transparency

3. Non-hermitian quantum mechanics and exceptional points

Below we give a brief introduction and motivation for investigating these particular topics. A more detailed introduction is contained in the relevant chapters.

1.1.1 Photon echo

A photon echo is the refocusing of optical polarisation after some time τ, after the application of electromagnetic pulses delayed by time τ. Photon echo has important applications in many fields - in nonlinear spectroscopy it is used to measure the dephasing time, T_2 (explained in Chapter 2), modified versions of photon echoes are being investigated for application in quantum memories as well as in quantum information processing. Even more than 50 years after its discovery by Erwin Hahn, the interest in echoes is still rising. Therefore we chose to study this phenomena in collaboration with experimentalists at University of Surrey.

We report on the dynamics of two-pulse photon echoes in a two-level system. We consider two different types of excitation pulse pairs; pulses with same carrier envelope phases (CEP pulse pairs) and pulse pairs cut from the same carrier wave train (labelled as normal pulse pairs). We show that for CEP pulse pairs when the pulses overlap somewhat, the photon echo emission time is strongly sensitive to the relative phase (i.e. delay time) between the two pulses. We also show how the photon echo emission time for such CEP pulse pairs depends on the dephasing time of the polarization (T_2) and on the pulse-width of the applied pulses. This phase sensitivity can be utilised to control the emission time of the photon echo which may prove useful in storing and retrieving light signals from an atomic ensemble. Our results also inform the interpretation of photon echo signals at short delay time when used to measure fast coherence decay rates.

1.1.2 Electromagnetically induced transparency

Electromagnetically induced transparency is the phenomenon that changes an opaque system to a transparent one for particular frequency in the presence of electromagnetic radiation. Chapter 3 details the analysis of an unsuccessful electromagnetically induced transparency experiment performed by our collaborators at University of Surrey. We report why the experiment failed and some guidelines on choosing the right parameters for the task.

1.1.3 Non-hermitian quantum mechanics and exceptional points

Decoherence and optical losses are one of the main obstacles in performing successful optical experiments. The motivation of investigating non-hermitian quantum mechanics is to find a way where decoherence/losses can be useful. We investigated two-level/four-level systems and found a small regime where even large losses in the systems can lead to a better signal to loss ratio. Chapter 4 details the theoretical investigation of non-hermitian quantum mechanics and exceptional points in real systems. In non-hermitian quantum mechanics, the notion of hermiticity is relaxed which leads to two kinds of systems -

1. Non-hermitian hamiltonians with real eigenvalues e.g. PT symmetric hamiltonians.
2. Non-hermitian hamiltonians with complex eigenvalues. These are the kinds of systems we focussed on in this thesis.

Exceptional points are the degeneracies of the non-hermitian systems where unlike the hermitian degeneracy, the eigenvalues as well as the eigenvectors coalesce thus resulting in a defective(non-diagonalisable) hamiltonian matrix. This leads to interesting topological behaviour near such points which are not present in hermitian systems. We report some of these interesting properties of exceptional points in a two-level and four-level system and describe how to observe these experimentally.

Chapter 2

Analysis of Photon Echo Dynamics

2.1 Introduction

Consider an inhomogeneous(different spins will have difference frequencies due to effects like doppler shifts, variations in local environments etc.) ensemble of spins in the presence of a magnetic field as shown later in Fig. 2.2. Every spin will have a magnetic moment on which the external magnetic field exerts torque resulting in spin precession. as shown in Eq. 2.1.

$$\vec{\tau} = \vec{\mu} \times \vec{B} = \gamma \vec{J} \times \vec{B} \tag{2.1}$$

where γ is the gyromagnetic ratio, $\vec{\mu}$ is the magnetic moment, $\vec{B}$ is the external magnetic field and $\vec{J}$ is the angular momentum. Due to inhomogeneous local effects, different spins will have different Bohr frequencies resulting in spin precession at different frequencies. There will be net magnetisation in the system in the direction of magnetic field. This net magnetisation can be manipulated by the application of electromagnetic pulses. Any pulse that rotates the magentisation by $\pi/2$ is known as $\pi/2$ pulse. In terms of energy level picture, a $\pi/2$ pulse is the excitation pulse takes the particles in the lower state to the higher state. Similarly a π pulse results in a π rotation of magnetisation or excitation-deexcitation cycle of the particles in energy level picture. The signal(net magnetisation) observed decays with time because of two main reasons -

1. Spin relaxation - This decay is irreversible in nature.

2. Inhomogeneous dephasing - Since different spins have different Bohr's frequency, they spin with different rates thus causing the net signal to dephase/decay. This is

a reversible decay.

Application of an appropriate electromagnetic pulse can reverse the effects of inhomogeneous dephasing. In magnetic resonance, the refocusing of spin magnetisation by a resonant electromagnetic radiation is known as spin echo. Spin echoes, also known as Hahn echoes[15], were first discovered by Erwin Hahn in 1950 when he applied two $\pi/2$ pulses successively, detecting a signal(echo) after some time even when no pulse was applied at that time. This idea was later extended by Carr and Purcell[16] where it was shown that a second π pulse is more effective than a $\pi/2$ pulse in producing an echo. Application of a $\pi/2$ pulse is equivalent to $\pi/2$ rotation of the net magnetisation. This magnetisation decays with time due to above mentioned reasons. The application of a second π pulse(also known as refocusing pulse) after some time τ_d inverts the magnetisation thus reviving the signal at time τ_d after its application. This can be best understood by visualising the spin magnetisation in Bloch sphere (Fig. 2.1) as illustrated in Fig. 2.2. A Bloch sphere is a geometrical representation of quantum states of a two level system. Any two level quantum state can be written as the superposition of basis states. In natural basis, a general state can be written as -

$$|\psi\rangle = e^{-i\beta}[\cos(\theta/2)|0\rangle + e^{-i\phi}\sin(\theta/2)|1\rangle]. \tag{2.2}$$

Here β is the global phase, ϕ is the relative phase and θ is some angle chosen to represent the coefficients in a way so that the total probability adds up to 1. The probabilities associated with this expression are independent of the global and relative phase.

$$P_0 = (\cos(\theta/2))^2, \tag{2.3}$$

$$P_1 = (\sin(\theta/2))^2. \tag{2.4}$$

A Bloch sphere is the representation of the statevector in terms of θ and ϕ e.g $\theta = 0$ represents the $|0\rangle$ state i.e the north pole of the Bloch sphere represents the population entirely in ground($|0\rangle$) state and $\theta = \pi$ represents the $|1\rangle$ state i.e the south pole of the Bloch sphere represents the population entirely in excited($|1\rangle$) state. Any state on the equator represent a 50:50 population distribution in both basis states. The states on the surface of the sphere are pure states and the states inside the sphere are mixed states. This can be generalised to n-level quantum system but then the visualisation is not very

useful. In optics the axis in Bloch sphere represent different types of polarisations and also known as Poincare sphere. Fig. 2.1[wikipedia] shows the Bloch sphere.

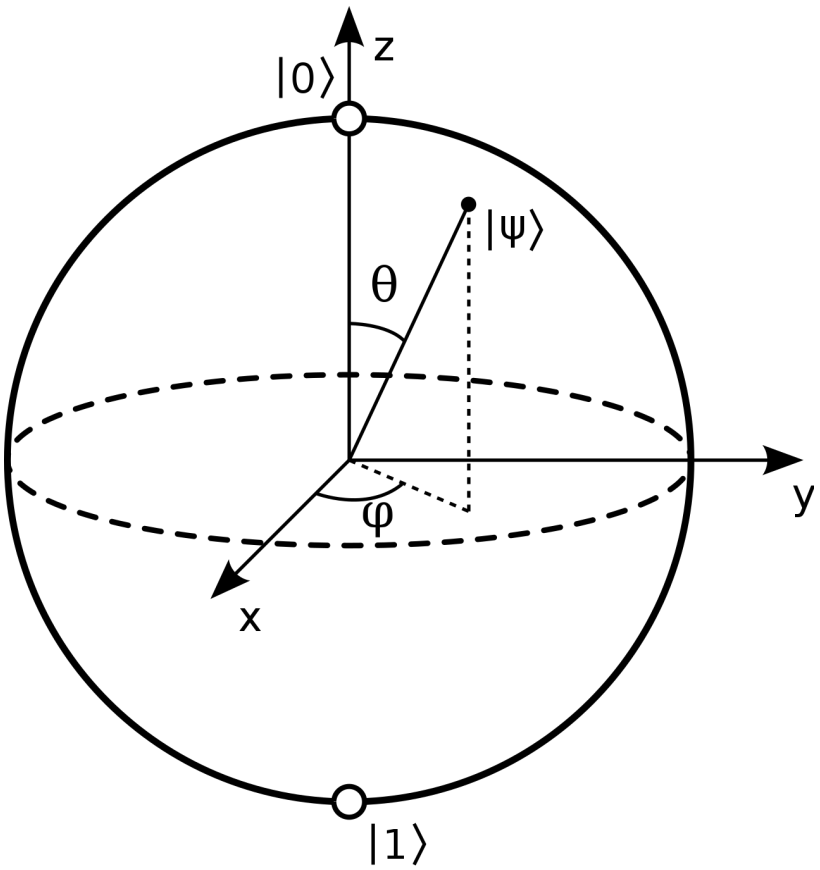

Figure 2.1: Bloch sphere. Here x,y,z are the axis directions and not the quantum states.

Fig. 2.2 illustrates all the steps of spin echo from a top view of the Bloch sphere where the upper left and lower right plots show the net magnetisation coming out of the plane and the remaining in the plane of the paper. It shows the state of a inhomogeneously broadened spin-$1/2$ system in the presence of a magnetic field(direction is out of the plane). Moving from subplots a-e, there's net magnetisation in the direction of applied field(a). Application of a $\pi/2$ pulse rotates the magnetisation by 90 degrees(b). The different spins precess(anticlockwise in this example) with different frequencies(local effects, c). After some time τ_d, application of a π pulse leads to subplot (d) where the precession of the spins are flipped. We can imagine the different spins to return to the initial position in time τ_d (as all spins are still precessing anticlockwise with slowest spin in front). This is the echo signal which appears τ_d time after the second pulse. Photon echoes are simply Hahn echoes observed at optical frequencies i.e rephasing of optical polarisation in an inhomogeneously broadened sample after application of a pulse pair.

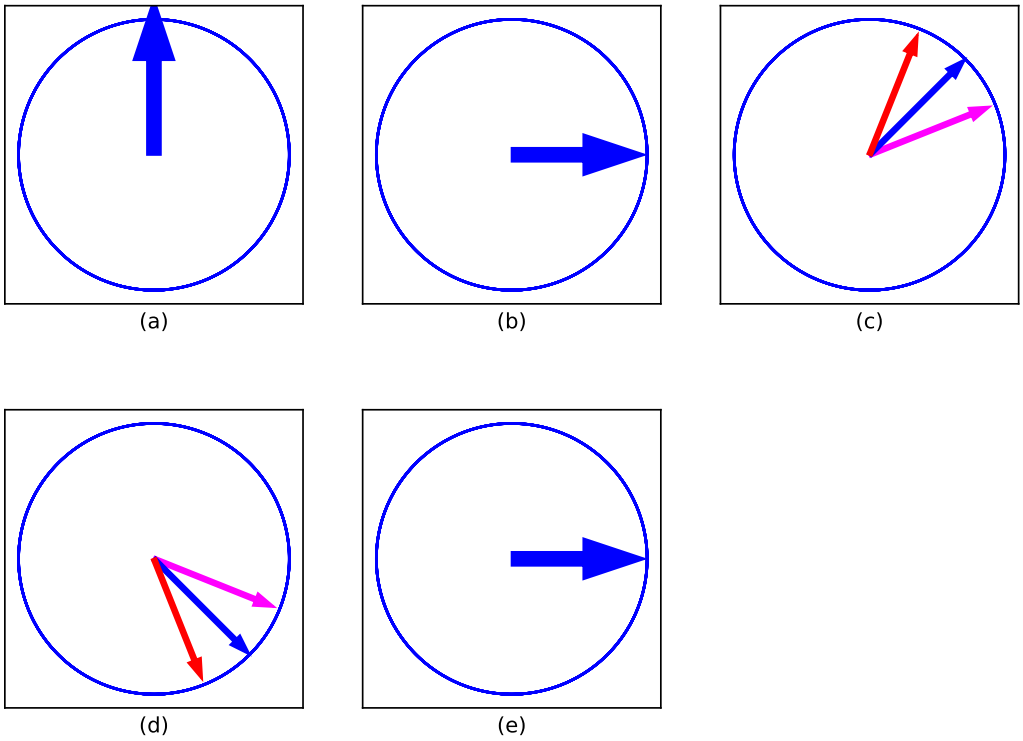

Figure 2.2: Illustrating spin echo using Bloch sphere(a-e). A magnetic field is applied to an ensemble of spins with direction out of the plane of the paper. (a) The net magnetisation in the system pointing in the direction of the applied magnetic field i.e. out of the plane of the paper, (b) Application of initial pulse($\pi/2$) rotates the net magnetisation by $\pi/2$ thus bringing it into the plane of the paper, (c) Inhomogeneous dephasing. In this plot, red is faster than blue which is faster than magenta, (d) Application of π pulse(τ_d time after the initial pulse) reverses the position of fast moving and slow moving spins. (e) All the spins re-align τ_d time after the application of π pulse

Echoes have important application in many fields including spectroscopy[17, 18], quantum information processing[19], studying magnons/phonons in single crystals[20] and measurement of spin-spin or polarization relaxation times (T_2)[21]. The photon echo is one potential candidate for quantum storage of light in an atomic ensemble and photon echoes are being investigated for application in long term optical quantum memories[22–24]. Conventional photon echoes have low signal retrieval efficiency[25] and the time of the echo appearance after the second pulse is fixed near to the inter-pulse delay. This is not a desired property in the field of quantum memories. Therefore, techniques for on-demand retrieval of the photon echo would be beneficial[26, 27] and techniques like controlled reversible inhomogeneous broadening (transverse as well as longitudinal) are being developed to increase the signal retrieval efficiency of such systems[28]. Even after sixty eight years, the interest in echo phenomena is still rising as further applications emerge, therefore it is imperative that we study and understand all aspects of photon echo dynamics.

To summarise, echoes originate from the rephasing of spin coherence (or refocusing of optical polarisations) after the application of a pair of radio frequency(or optical) excitation pulses delayed by time τ_d. Increasing the delay between the two pulses increase the time of the appearance of echo. This also reduces the echo strength. Measuring how echo strength varies with the inter-pulse delay leads to the measurement of spin-spin relaxation Due to the exponential nature of spin-spin relaxation, it's difficult to experimentally observe photon echo in sample where spin-spin relaxation rate is high. One way around this problem is to use short pulses with low inter-pulse delay. This leads to the cases when the pulses slightly overlap thus changing the dynamics(position and strength) of echo depending on the overlap. We explored this regime and quantified echo dynamics in such situations.

2.2 Bloch equations

A general two level state can be written as a superposition state

$$\psi = C_1\psi_1 + C_2\psi_2, \tag{2.5}$$

where $\psi_{1,2}$ forms the basis. The electric field is,

$$E(t) = \varepsilon(t)\cos(\omega t - \phi), \tag{2.6}$$

The Hamiltonian of a two level system interacting with light is,

$$H = \begin{bmatrix} \hbar\omega_1 & V \\ V^* & \hbar\omega_2 \end{bmatrix}, \tag{2.7}$$

where $\omega_{1,2}$ are the frequencies of the energy levels of the system in the absence of any interaction and V is the interaction energy between light and the system. Without loss of generality we can assume ω_1=0 i.e ground state at zero energy. Applying Schrödinger's equation

$$i\hbar\frac{d\psi}{dt} = H\psi, \tag{2.8}$$

we get,

$$i\hbar\begin{bmatrix} \dot{C}_1 \\ \dot{C}_2 \end{bmatrix} = \begin{bmatrix} VC_2 \\ V^*C_1 + \hbar\omega_2 C_2 \end{bmatrix}, \tag{2.9}$$

The dipole interaction can be calculated by

$$\begin{aligned} V &= -d.E(t), \\ V &= -d\varepsilon(t)\cos(\omega t-\phi), \\ V &= \hbar\Omega\cos(\omega t-\phi), \\ V^* &= \hbar\Omega^*\cos(\omega t-\phi), \end{aligned} \tag{2.10}$$

where Ω = -$d\varepsilon(t)/\hbar$ is the rabi frequency. Hence

$$\begin{bmatrix} \dot{C}_1 \\ \dot{C}_2 \end{bmatrix} = -i \begin{bmatrix} \Omega\cos(\omega t-\phi)C_2 \\ \Omega^*\cos(\omega t-\phi)C_1+\omega_2 C_2 \end{bmatrix}. \tag{2.11}$$

Similarly,

$$\begin{bmatrix} \dot{C}_1^* \\ \dot{C}_2^* \end{bmatrix} = i \begin{bmatrix} \Omega^*\cos(\omega t-\phi)C_2^* \\ \Omega\cos(\omega t-\phi)C_1^*+\omega_2 C_2^* \end{bmatrix}. \tag{2.12}$$

These equations describe the wave-function evolution with time by calculating $C_{1,2}$ at all times. Physically, we are more interested in the populations of the energy levels as well as the polarisation in the system. These physical parameters can be defined in terms of $C_{1,2}$ as -

$$n_1 = C_1^*C_1, \tag{2.13}$$

$$n_2 = C_2^*C_2, \tag{2.14}$$

where n_1 is the ground state population and n_2 is the excited state population.

$$\begin{aligned} \frac{d(C_1^*C_1)}{dt} &= C_1^*\dot{C}_1+\dot{C}_1^*C_1, \\ &= C_1^*(-i\Omega\cos(\omega t-\phi)C_2)+(i\Omega^*\cos(\omega t-\phi)C_2^*)C_1, \\ &= i[\cos(\omega t-\phi)(C_2^*C_1\Omega^*-\Omega C_1^*C_2]. \end{aligned} \tag{2.15}$$

Similarly,

$$\frac{d(C_2^*C_2)}{dt} = -i[\Omega^*\cos(\omega t-\phi)C_2^*C_1-\Omega\cos(\omega t-\phi)C_2C_1^*], \tag{2.16}$$

$$\frac{d(C_2^*C_1)}{dt} = -i[\Omega\cos(\omega t-\phi)C_2^*C_2-\Omega\cos(\omega t-\phi)C_1^*C_1-\omega_2 C_2^*C_1]. \tag{2.17}$$

Multiplying both side by $e^{-i\omega t}$ and defining the polarisation as P=$C_2^* C_1 e^{-i\omega t}$

$$\frac{dP}{dt} - (-i\omega)e^{-i\omega t}C_2^* C_1 = -i\Omega(C_2^* C_2 - C_1^* C_1)\cos(\omega t - \phi)e^{-i\omega t} + i\omega_2 C_2^* C_1 e^{-i\omega t}.$$

Using Euler's formula to write cosine in terms of exponential and applying the Rotating Wave Approximation (ignoring fast oscillating terms i.e. terms with 2ω frequencies) we get,

$$\frac{dP}{dt} = i[\Omega\frac{(|C_1|^2 - |C_2|^2)}{2}e^{-i\phi} + iP(\omega_2 - \omega). \tag{2.18}$$

This implies

$$\frac{dn_1}{dt} = i\frac{\Omega}{2}[Pe^{i\phi} - (Pe^{i\phi})^*], \tag{2.19}$$

$$\frac{dn_2}{dt} = -i\frac{\Omega}{2}[Pe^{i\phi} - (Pe^{i\phi})^*], \tag{2.20}$$

$$\frac{dP}{dt} = i[\frac{\Omega}{2}e^{-i\phi}(n_1 - n_2) + P\Delta]. \tag{2.21}$$

where $\Delta = \omega_2 - \omega$. For multiple pulses and taking population/polarisation radiative relaxation times into account, we get [29]

$$\frac{dn_1}{dt} = i\sum_j \frac{\Omega_j(t)}{2}[Pe^{i\phi_j} - P^* e^{-i\phi_j}] + \frac{n_2}{T_1}, \tag{2.22}$$

$$\frac{dn_2}{dt} = -i\sum_j \frac{\Omega_j(t)}{2}[Pe^{i\phi_j} - P^* e^{-i\phi_j}] - \frac{n_2}{T_1}, \tag{2.23}$$

$$\frac{dP}{dt} = i\sum_j \frac{\Omega_j(t)}{2}e^{-i\phi_j}(n_1 - n_2) + iP\Delta - \frac{P}{T_2}, \tag{2.24}$$

where the summation over j covers multiple pulses and T_1, T_2 are respectively the population and polarisation radiative relaxation times with $T_1 = 2T_2$. The relaxation times are added phenomenologically in the equations. These can be derived directly by considering a non-hermitian Hamiltonian which forms the basis for chapter 4. Analytically solving these differential equations is intractable for general pulses(except top-hat pulses). Therefore, we solve the Bloch equations numerically to understand the photon echo dynamics in different regimes.

Before proceeding to numerical simulations in the regime of overlapping pulses, we'll describe a perturbative solution to (2.11). Changing the frame to the rotating frame of the

applied laser and applying RWA, we get

$$\frac{d}{dt}C_1 = \frac{-i}{2}\Omega(t)C_2(t), \tag{2.25}$$

$$\frac{d}{dt}C_2 = \frac{-i}{2}\Omega(t)C_1(t) - i\Delta C_2(t), \tag{2.26}$$

where Ω is the Rabi frequency and Δ is the detuning frequency. A first order perturbative solution of these differential equations can be found by using the integrating factor method,

$$C_2(t) = C_2(0) - \frac{i}{2}e^{-i\Delta t}\int^t e^{i\Delta t'}\Omega(t')C_1(t')dt'. \tag{2.27}$$

Now consider that initially the whole population is in ground state. And assuming very small perturbation by the application of pulse we can approximate that the population in the ground state remains almost unchanged i.e. $C_1(t) \approx 1$. Using this approximation, we can get the expression for $C_2(t)$

$$C_2(t) \approx -\frac{i}{2}e^{-i\Delta t}\tilde{\Omega}(\Delta), \tag{2.28}$$

where, $\tilde{\Omega}$ is the Fourier transform of the Rabi frequency function. Defining $n_2 = |C_2|^2$ as the population of excited state,we get

$$n_2 \approx \frac{1}{4}|\tilde{\Omega}(\Delta)|^2. \tag{2.29}$$

This implies the population of the excited state depends on the *Fourier transform* of the Rabi frequency function(which in turn depends on the amplitude of the applied electric field) at the detuning frequency. For a 2-pulse case -

$$\begin{aligned} n_2 &\approx \frac{1}{4}[|\tilde{\Omega}_1(\Delta)|^2 + |\tilde{\Omega}_2(\Delta)|^2 + \Omega_1^*(\Delta)\Omega_2(\Delta) + \Omega_2^*(\Delta)\Omega_1(\Delta)], \\ &= \frac{1}{4}[\tilde{\Omega}_1(\Delta) + \tilde{\Omega}_2(\Delta)]^2 \end{aligned} \tag{2.30}$$

For two identical Gaussian pulses in a $\pi/2 - \pi/2$ sequence separated by some delay in time -

$$n_2 \approx \frac{1}{2}\Omega_0[\delta^2\pi e^{-\frac{\delta^2\Delta^2}{2}}](1+\cos(\tau_d\Delta)), \tag{2.31}$$

where, $\Omega_0 = \sqrt{\pi}/(2\delta)$ for a $\pi/2$ pulse, δ is the pulsewidth and τ_d is the delay between the pulses. From this equation we can infer that the excited state population will have a gaussian envelope, the overall envelope of the fringes will have a pulse-width dependence as the exponential factor includes δ i.e the pulse-length and the fringe separation/fringe-width/number of fringes will depend on the pulse delay(τ_d). This result is true in the case of weak pulses but Fig. 2.3 shows a simple photon echo experiment simulation using a top hat(uniformly distributed) inhomogeneous ensemble of 600 two level atoms (with absorption linewidth of 0.028THz) interacting with gaussian pulses. At time t=50ps, a $\pi/2$ pulse(50ps pulse-width) is applied which is followed by a π pulse at time t=170ps. This implies that pulse delay τ_d is 120ps. We can see the echo appears at time t=(170-50)ps i.e.120ps after the application of π pulse or at t = 290ps even when no pulse was applied at time 290ps. In this case, the pulses are well separated so the echo appears at the expected position i.e. if τ_d is the difference between the first two pulses then the echo appears at time τ_d after the second pulse. Later we study the photon echo dynamics when the pulses overlap in time domain.

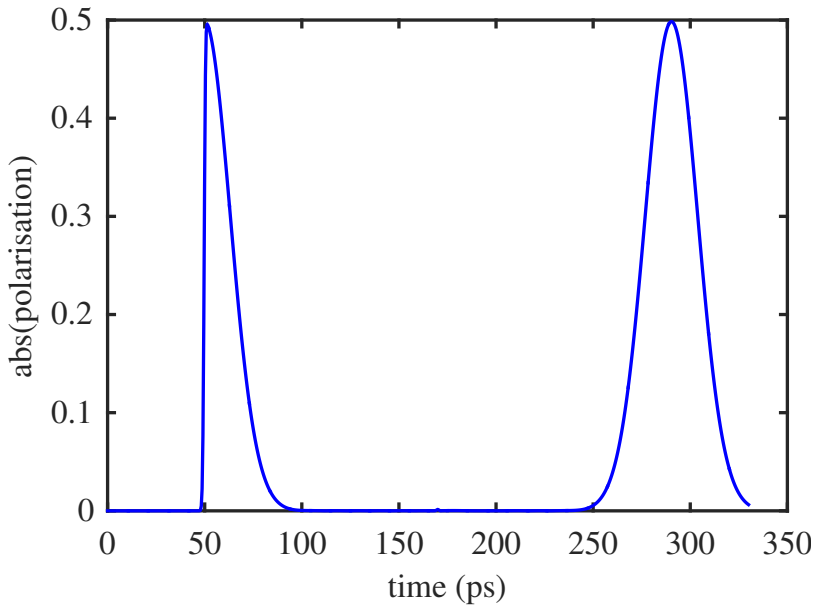

Figure 2.3: Illustration of photon echo with gaussian pulses. The first pulse($\pi/2$) is applied at 50ps and the refocusing pulse (π) is applied at 170ps). The echo appears at 290ps i.e 120ps after the application of refocusing pulse.

2.3 Carrier envelope pulses and two level physical system

In this section, we describe the physical system and the two types of pulses used to study the photon echo dynamics when pulses overlap. These define the parameters used in the numerical simulations.

2.3.1 Physical system

The two level system used in our studies correspond to 1s - $2p_+$ transitions of phosphorus doped silicon (Si:P) which has potential for quantum information processing[30, 31]. This particular system was chosen according to the experimental convenience of our collaborators at University of Surrey where the aim was to measure the echo signal electrically by measuring the polarisation of the donor electrons. The behaviour we report however is generic and can be easily applied with appropriate scaling, to other materials/systems. The pulses are chosen to be gaussian and most of the work focuses in the regime where pulses are overlapping in time domain.

2.3.2 Two kinds of pulse pairs

First, we describe two kinds of pulse-pairs. This is important as our collaborators at University of Surrey can use one kind of pulses, therefore, we need to differentiate between the effect of choosing those pulses over the other kind. If there's significant difference introduced by the kind of pulses then this will also help in choosing parameters for future experiments. For pulse pairs that each have the same carrier envelope phase, denoted *CEP* pulse pairs, the electric field can be written as

$$E(t) = \sum_{j=1,2} E_j(t) = \sum_{j=1,2} \mathscr{E}_j \; e^{-(t-t_j)^2/2\delta^2} \cos(\omega(t-t_j)),$$

where $\mathscr{E}_j$ is the pulse peak amplitude, t_j locates the pulse Gaussian envelope in time and ω is the driving laser frequency and δ the temporal pulsewidth. Typically $\mathscr{E}_1, \mathscr{E}_2$ and δ are chosen to yield $\pi/2$ and π pulse areas respectively but this is not crucial to the photon echo phenomenon. For pulse pairs that are cut out from the same carrier wave train,

denoted here as *normal* pulses, the electric field can be written as,

$$E(t) = \sum_{j=1,2} \mathscr{E}_j \; e^{-(t-t_j)^2/2\delta^2} \cos(\omega(t-t_1)).$$

Notice that the phase term inside the cosine is the same for all values of j.

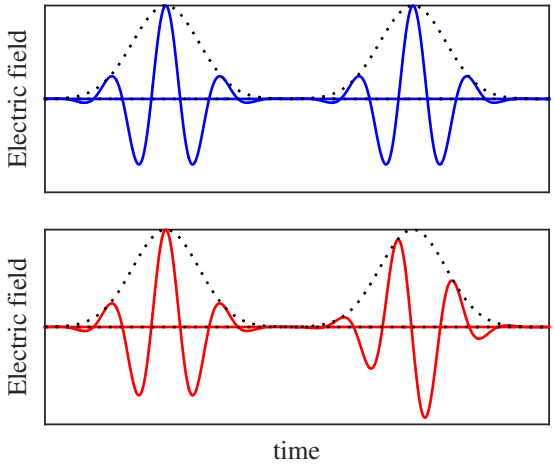

Figure 2.4: Illustration of a *CEP*-pulse pair (blue) and a *normal* pulse pair (red). The gaussian envelope (dotted) highlights the difference between CEP and normal pulses.

Figure 2.4 illustrates both kinds of pulse pairs. We can see that the phasing of the envelope and the carrier wave of both pulses in a CEP pulse pair is identical whereas for normal pulse pairs this is not the case. Most of the studies (and applications hitherto) of photon and spin echoes consider only non-overlapping pulses. By exploring the regime where pulses partially overlap, we found that the photon echo signal is very sensitive to the *relative* phase (i.e. inter-pulse delay, τ_d) between the pulses when a CEP pulse pair is used. Unsurprisingly the absolute value of the carrier envelope phase has no influence on the echo dynamics other than defining the phase of the underlying polarization oscillations. Using numerical simulations and approximate analytic solutions to the optical Bloch equations we find that large shifts in the echo emission time are possible by controlling parameters such as the delay between the pulses, the inhomogeneous broadening of the two-level ensemble, the pulse-widths of the applied pulses and the polarization dephasing time. Results from this study show that we can achieve control over the emission time of the echo signal while using the same pulse sequence($\pi/2$-π) as the conventional echoes. This was not possible before in a two-level system. Therefore, just by overlapping the pulses we can increase the storage time of the signal (limited by T_2) significantly as shown in the numerical simulations in the Section 2.4.

Photon echo experiments which attempt to measure dephasing times which are close to the available pulse durations will naturally make some measurements with partially overlapping excitation pulses. Our results show that, depending on the relative phase difference between the pulses, strongly shifting (in time) photon echoes will arise. This may be misinterpreted as jitter or noise when, as we shall show, it is in fact a consequence of interference.

We next distinguish our results from previous published results where the phase difference between pairs of excitation pulses have proven useful in nonlinear spectroscopy. Reference [17] shows how the real/imaginary part of the nonlinear response function can be measured independently using non-overlapping phase-locked pulses by changing the phase between the two pulses to be in-phase and in-quadrature. Using heterodyne-detected phase-locked femtosecond stimulated photon echo and phase-locked, pump-probe techniques [32, 33] it has been shown that the relative phase between two initial pulses and the relative phase between the last two pulses are both important individually rather than only their difference. Here again the second and third pulses never overlap in time. A shift in echo maximum with delay between the pulses is plotted and a quantum beat like pattern is shown on the scale of 1 ps with a pulse-width of 14 fs, i.e. much longer than the frequency and therefore not an interference phenomenon. A deformation of pulses when overlapped in the time domain is not considered here which is the distinguishing feature in the results. The paper of Yano and Shinojima[34] considers a comparison between CEP and normal pulses for photon echoes and coherent population control using a perturbative approach which neglects any pulse overlap. Their results predict a shift in echo temporal position with respect to pulse-widths when the dephasing and decay times differ, but this shift does not arise from the changing overlap between the pulses (as this is neglected from the start).

In coherent photon echo simulations, there are five independent energy/time quantities which come into play

1. the inter-pulse delay
2. the pulse-widths,
3. the inhomogeneous line-width,
4. the detuning of the excitation from the centre of the inhomogeneous line
5. the dephasing time.

In this large phase space there is no natural scaling, so we choose to present simulations for physical parameters corresponding to the 1s - $2p_+$ transitions of phosphorus doped silicon (Si:P) which has potential for quantum information processing.[30, 31] The behaviour we report however is generic can be easily applied with appropriate scaling, to other materials/systems. In the Bloch equations, normal pulses have, $\phi = 0$ and CEP pulses have $\phi = \omega\tau_d$ where τ_d is the delay between the pulses.

To include the influence of different local environments (i.e. inhomogeneous broadening) we simply solve the Bloch equations for two-level systems having a distribution of transition frequencies, Integrating over this distribution yields the total polarization, P_{total} for an ensemble of systems with the chosen inhomogeneous broadening i.e.,

$$P_{total} = \int^{\Delta'} P(\Delta')\, g(\Delta')\, d\Delta', \tag{2.32}$$

where Δ' is the detuning between transition and driving frequencies and $g(\Delta')$ is the normalized inhomogeneous distribution of two-level atoms with,

$$g(\Delta') = \mathscr{N} e^{-(\Delta'-\Delta)^2/(2\sigma^2)}. \tag{2.33}$$

In all our simulations the center frequency of the pulses is chosen to coincide with the center of the inhomogeneous distribution.

2.4 Numerical simulations

Here we present numerical simulations of Eqs. (2.22-2.33) to investigate the dependence of the photon echo emission dynamics on parameters such as relative phase between the pulse pair, pulse duration and dephasing. All the simulations in this chapter are for CEP pulses unless otherwise noted.

2.4.1 Photon echo dynamics for partially overlapping pulses

In this section, we show the results for the cases when the applied laser pulses partially overlap/interfere in time domain and how this affect the position of photon echo peak in time. In Fig. 2.5 we show the absolute value of the polarization for the cases where the two pulses partially overlap in time for different pulse interference conditions, i.e when pulses interfere constructively or destructively or somewhere in between. We see a large

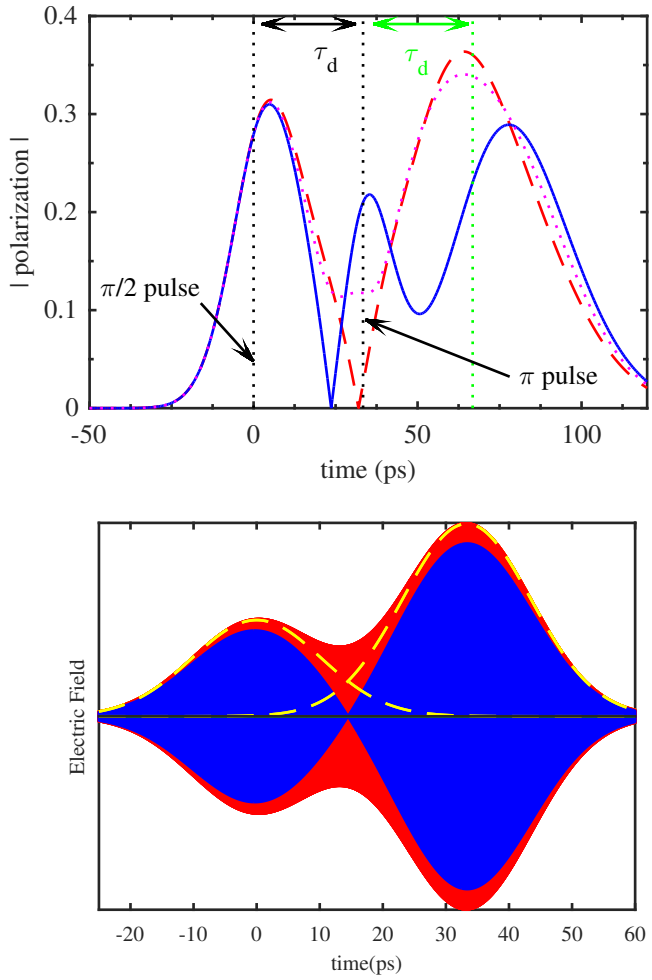

Figure 2.5: (Upper panel) Absolute value of the polarization vs time for different delays (τ_d) between the CEP pulses. Blue line (destructive interference, τ_d=33.4057 ps), dashed red line (constructive interference, τ_d=33.3531 ps), dotted magenta (quarter of an oscillation, τ_d=33.3794 ps). The transition frequency is 9.50437 THz, the detuning is zero and the first pulse has an area of $\pi/2$ and the second an area of π. The intensity FWHM pulse-width of both pulse envelopes is 17 ps, the FWHM inhomogeneous broadening is 0.028 THz and the dephasing time T_2 is infinite. $t = 0$ corresponds to the arrival of the peak of the first pulse. (Lower panel) Illustration of net driving electric field from overlapping $\pi/2$ and π-pulses under constructive red (light) and destructive blue (dark) interference conditions. Individual pulse envelopes are shown as the dashed yellow lines and the fast carrier frequency oscillation is not resolved. The amplitude of the destructive interference case (blue) has been reduced by 10% for clarity

shift (≈ 13 ps) in the arrival time of the echo even when the delay between the pulses is changed by only 0.05 ps, a very small fraction of the interpulse delay of around 33.4 ps.
To get the full picture of how the echo signal is changing with respect to the delay between the pulses we solved the Bloch equations numerically for many different delays and plotted the echo signal as a heatmap as shown in Fig. 2.6. As we change the delay, the relative phase between the pulses also changes ($\phi = \omega\tau_d$) where τ_d is the delay between the pulses, where ω is the laser frequency) resulting in change of interference(constructive, destructive or between them). This shows that the echo peak position and to a lesser extent the echo strength is very sensitive to the relative phase between the pulses.
When pulses don't overlap in the time domain we don't observe this phase sensitivity of the echo signal emission time whether the pulses used are CEP or normal. So the observed delay sensitivity is only seen for partially overlapping CEP pulses. This indicates that the origin of the phase sensitivity lies in the interference between the electric fields of the pulses and not between the polarization oscillation induced by the first pulse interfering with the second pulse. The result of such interference is seen in the lower panel of Fig. 2.5; the constructive interference case (red) resembles a single pulse with an amplitude modulation while the nodal structure in the destructive interference case (blue) produces two slightly shorter but sequential pulses. We will use this observation to construct an analytical model of the system in the Section 2.5. This phase sensitivity has implications for the use of photon echo techniques to measurements of dephasing (T_2) times. If the dephasing times are similar to the pulse length, care must be taken to either use normal pulse pairs or to account for the phase difference between the pulses in the analysis.

2.4.2 Influence of pulse overlap area

We next investigate how the area of overlap between the pulses quantitatively affects the photon echo emission time and its dependence on the relative phase between the two pulses. This overlap area can be changed either by (i) changing the pulse-width keeping the delay between the applied pulses constant or (ii) changing the delay between the applied pulses while keeping the pulse-width constant.
Figure 2.7 shows the effect of changing the pulse-width while keeping all other parameters, including the pulse areas, fixed. For destructive interference, around τ_d=33.4 ps, as we increase the pulse-width the shift in the echo peak position in time increases by over 15 ps. Also interesting are the qualitative changes that increasing the pulse-width brings mid-way

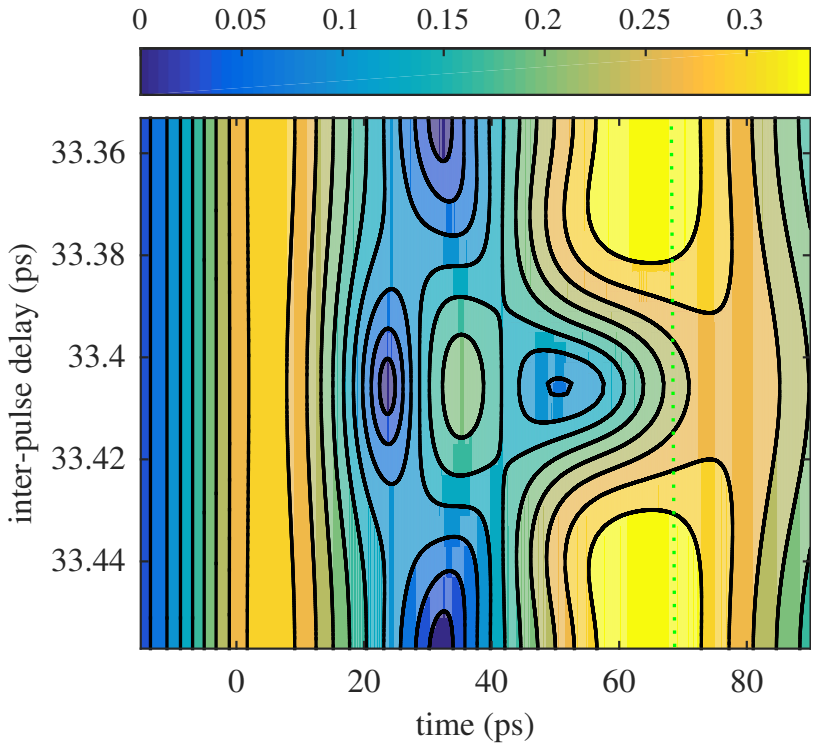

Figure 2.6: Heatmap of absolute value of polarization versus time for different delays(τ_d) between the pulses for photon echo using CEP pulses. The green dotted line indicates the time τ_d after the second pulse peak. Parameters are as in figure 2.5.

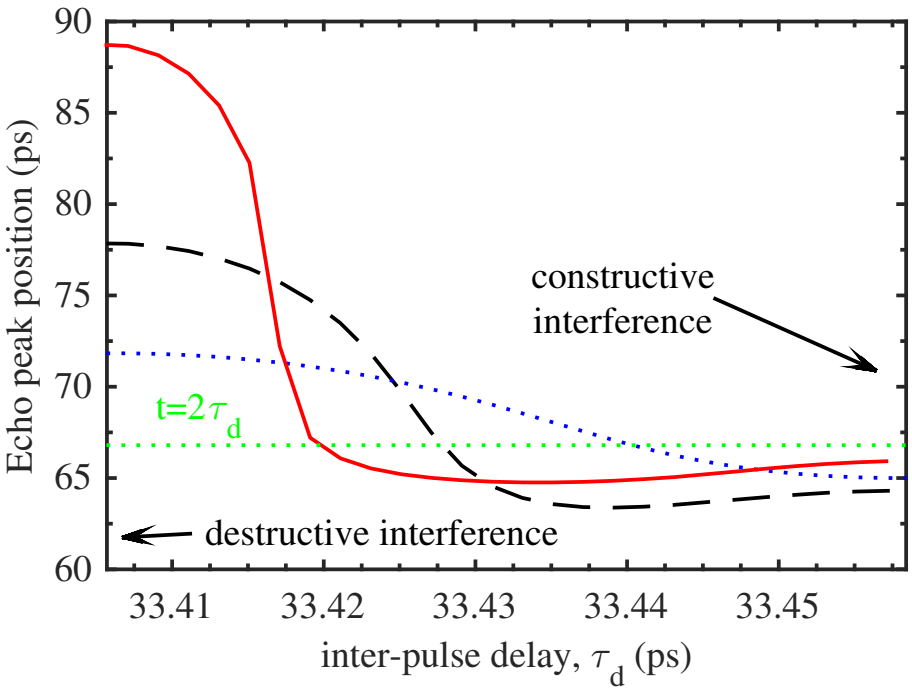

Figure 2.7: Echo peak position in time vs delay between the pulses for different (intensity) pulse-durations - dotted blue line, FWHM=12 ps; dashed black line, FWHM=17 ps; red line, FWHM=23.5 ps. Across the figure the interference condition passes from destructive(left) to constructive(right). The horizontal green dotted line indicates the time τ_d after the second pulse peak. Other parameters are as in figure 2.5.

between constructive and destructive interference conditions around a delay τ_d=33.43 ps; the echo peak position is not even monotonic with the pulse-width. For constructive interference between the pulses, the shifts seen are rather small indicating an insensitivity to pulse width in this regime. Figure 2.8 shows the photon echo peak position in time versus delay between the pulses for a fixed (intensity) pulse-duration of 17 ps (FHWM). We show scans from destructive interference through to constructive for three different delays around (a) τ_d=40 ps, (b) τ_d=33.4 ps and (c) τ_d=25.1 ps . The change in overlap area of the two pulses is negligible within one scan but appreciable between the three subplots. We can see that here also the qualitative nature of the echo signal changes as we increase the delay; for shorter delays constructive interference echoes are emitted at latter times than for mixed quadrature excitation. Overall, for all interference conditions, longer pulse excitation tends to bring the emission back towards the $t = 2\tau_d$ line.

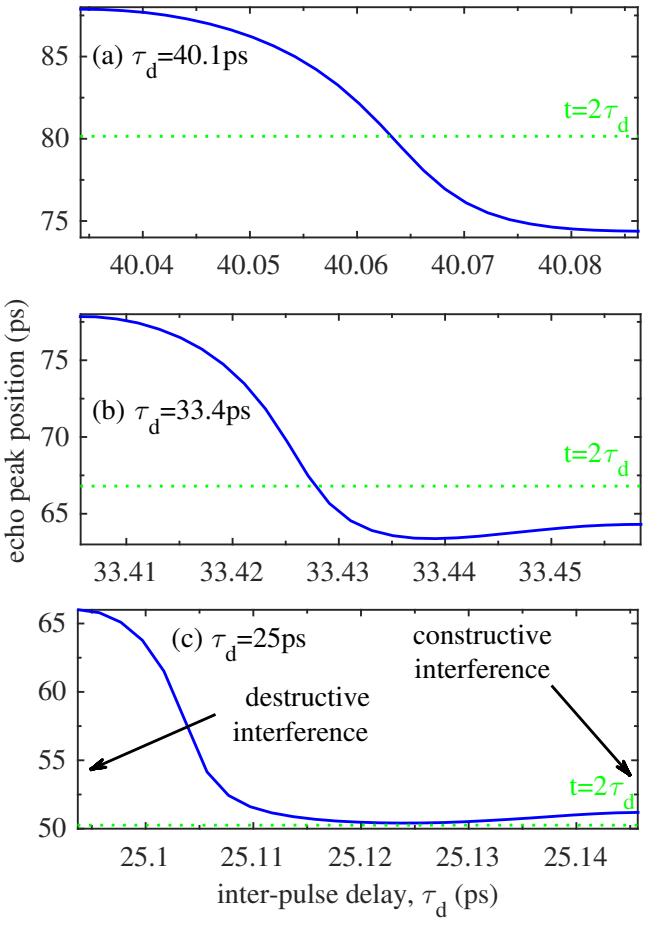

Figure 2.8: Echo peak position in time vs delay between the pulses for different delays around (a) τ_d=40.1 ps, (b) τ_d=33.4 ps and (c) τ_d=25 ps. Across the figure the interference condition passes from destructive(left) to constructive(right). The green dotted line indicates the time τ_d after the second pulse peak. Other parameters are as in figure 2.5.

We conclude from these simulations that it is the specific combination of pulse-width and

inter-pulse delay that determines the qualitative behaviour of echo not simply the area of overlap between the pulses. We have also run simulations where by changing both the pulse duration and the inter-pulse delay we hold the pulse overlap constant and find no universal dependence on overlap area.

2.5 Analytical formulae for photon echo signals

In this Section we describe three special cases where we can derive an analytical formulae for the shifts in the position of photon echo in the CEP case. The electric field of the pulses are assumed to be top hat in time and have the same amplitude. The second pulse is twice as long as the first and thus has the required area for a π pulse. The three cases are - (A) when the applied pulses don't overlap, (B) when the applied pulses interfere destructively and (C) when the applied pulses interfere constructively.

2.5.1 Non-overlapping pulses

For comparison in case when pulses don't overlap in time there is an existing result[29],

$$P(t_4) = -2\ \mathscr{P}_0\, e^{-\sigma^2(t_{43}-t_{21}-1/\Omega_1)^2/2} \sin(\omega t_4), \tag{2.34}$$

where $P(t_4)$ is the polarization after the application of the second pulse, $\mathscr{P}_0$ is a constant,Ω_1 is the Rabi frequency of the initial $\pi/2$ pulse. t_{21} is the time interval between the two pulses and t_{43} is the time coordinate relative to the end of the second pulse. As can be seen from (2.34) the echo appears when these two are almost equal, with a small correction due to the finite pulse width (See Fig. 2.9).

2.5.2 CEP pulses - destructive interference

In the case of CEP pulses the total electric field can be written as a piecewise constant field of varying amplitude (see Fig. 2.9(a)). When the pulses overlap the electric field is zero so instead of overlapping $\pi/2$ and π pulses we have two pulses with smaller area and a period of free nutation in between. This gives rise to a modified echo which is the origin of the phase control of the photon echo dynamics we report here. In each section of the pulse sequence, we can write the solution in the Rabi form [35] and by multiplying the matrices together an analytic solution for the polarization can be found. This only works

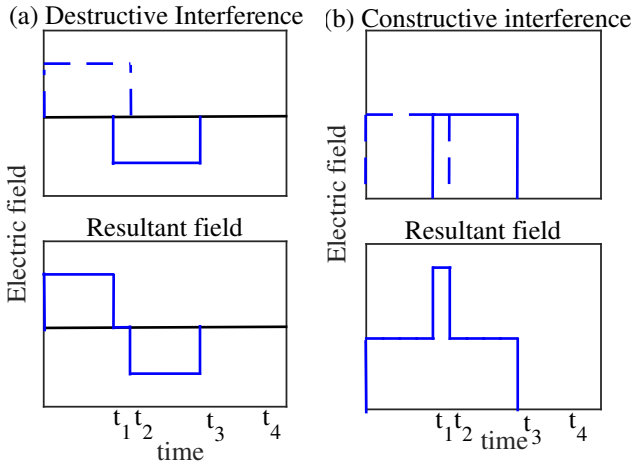

Figure 2.9: The envelope of two top hat pulses interfering (a) destructively and (b) constructively. The destructive interference provides a region of zero field when the pulses are overlapping which allows an interval of free polarization oscillation and rephasing. For the constructive case interference in the interval (t_1, t_2) causes the amplitude of the electric field to double at those times. In effect this results in three consecutive finite field regions.

for perfectly constructive or destructive interference but still we can gain some insight by studying these limits. Following the same calculation as in[29] but with CEP pulses we derive the result for destructively interfering pulses,

$$\begin{aligned} P(t_4) &= \mathscr{P}_0[\cos A\ (e^{-\sigma^2(t_{43}+t_{21}-C)^2/2} - e^{-\sigma^2(t_{43}-t_{21}-C)^2/2}) \\ &- \cos^2 A\ (e^{-\sigma^2(t_{43}+t_{21}+D)^2/2} + e^{-\sigma^2(t_{43}-t_{21}+D)^2/2}) \\ &+ 2\sin^2 A\ e^{-\sigma^2(t_{43}+E)^2/2}\ ]\sin(\omega t_4), \end{aligned} \tag{2.35}$$

with

$$\begin{aligned} C &= (1+\sin 2A)/\Omega_1, \\ D &= (\sin A \sec^2 A - \sec^2 A - \tan A)/\Omega_1, \\ E &= (\cot A + \csc A)/\Omega_1, \end{aligned}$$

where A is the area of overlap between the pulses (between 0 and $\pi/2$), ω is the applied laser frequency, $t_{21} = t_2 - t_1$, $t_{43} = t_4 - t_3$ are the times as shown in Fig. 2.9. As pulse area A is always less than $\pi/2$, C and E are always positive while D is always negative. Superposition of the first four terms in the formula defines the echo profile and arrival time, while the last term doesn't actually contribute to the echo signal after time t_3 because E is always positive which implies that the peak of the gaussian lies before t_3 and hence

doesn't affect the echo that comes at times later than t_3. The shift in the position of echo depends on the area of overlap(A) between the pulses and the Rabi frequency of the applied pulses. For $A = 0$ this result reduces to (2.34) as it must.

(2.35) describes well the observed behaviors for destructive interference. Increasing the pulse duration for a fixed delay, or decreasing the delay time for a fixed pulse duration increases the pulse overlap area A. As A increases, C becomes larger and D more negative and both these trends lead to an increase in the shift of the echo emission time. Both these trends are seen in the full numerical simulations of Figs. 2.7 and 2.8.

The FWHM of each term in (2.35) is inversely related to the FWHM of the inhomogeneous broadening distribution i.e the broader the ensemble line-width (larger σ), the narrower the gaussians in each term of the formula. Therefore, the superposition between these four terms will change if we change the inhomogeneous broadening distribution. This implies that the echo position also depends on the ensemble line-width. By controlling the area of overlap between the pulses as well as the pulse-width we can have control over the emission time of the echo which might be important in storing light using atomic ensembles.

2.5.3 CEP pulses - constructive interference

For constructive interference between the CEP pulses (see figure 2.9(b)), we find,

$$P(t_4) = -\mathscr{P}_0\, e^{-\sigma^2(t_{43}-1/\Omega_1)^2/2}\, \sin(\omega t_4).$$

This result is independent of the overlap between the pulses which is consistent with the rather weak shifts seen for constructive interference in Figs. 2.7 and 2.8. This formula is only valid when $A \neq 0$ and therefore it's not equivalent to (2.34). Effectively within this analytic model there is no real echo emitted. This can be understood by noting that there is no free precession interval (the electric field in the interval t_{21} is not zero) between the two pulses. This means the macroscopic polarization does not have time to freely unphase, therefore we don't get a distinct photon echo signal from the rephasing of oscillators after the excitation pulses are gone.

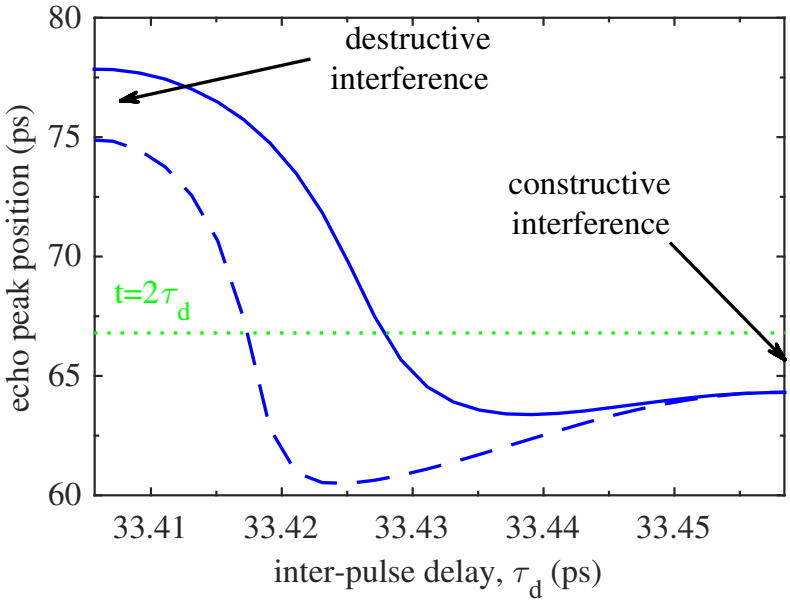

Figure 2.10: Echo peak position in time vs delay between the pulses for different dephasing times. Solid (dephasing time - infinite) and dashed (dephasing time T_2 =120 ps). The green dotted line indicates the time τ_d after the second pulse peak. Other parameters are as in figure 2.5.

2.6 The influence of dephasing

In Fig. 2.10 we show the effect of introducing a finite polarization dephasing time, T_2=120 ps, on the echo peak position in time. For destructive interference we find that the finite dephasing time shifts the curve to earlier times while for constructive interference we find essentially no effect. For shorter pulses (not shown) there is also a shift for constructive interference to earlier times too but a full exploration of this phase-space is beyond the scope of this project.

Photon echo decay with a non-overlapping $(\frac{\pi}{2},\pi)$ pulse sequence is the conventional technique to measure the polarization relaxation times (T_2). The echo signal strength is measured for a range of inter-pulse delays and an exponential decay in strength (with the rate of decay depending on T_2) is observed. Such measurements are most easily done when the dephasing time is considerably longer than the pulse duration allowing for time discrimination over a decade or more in signal decay. Our results on the strong phase sensitivity of the echo arrival time inform such measurements in two ways. Firstly at early times when the pulses overlap to some degree, unless care is taken over the precise inter-pulse phase at each delay selected there will appear in the data some scatter reflecting the spread of excitation phases used. Without an appreciation of the source of this scatter it may be wrongly interpreted as due to some other source of noise. Secondly, often it

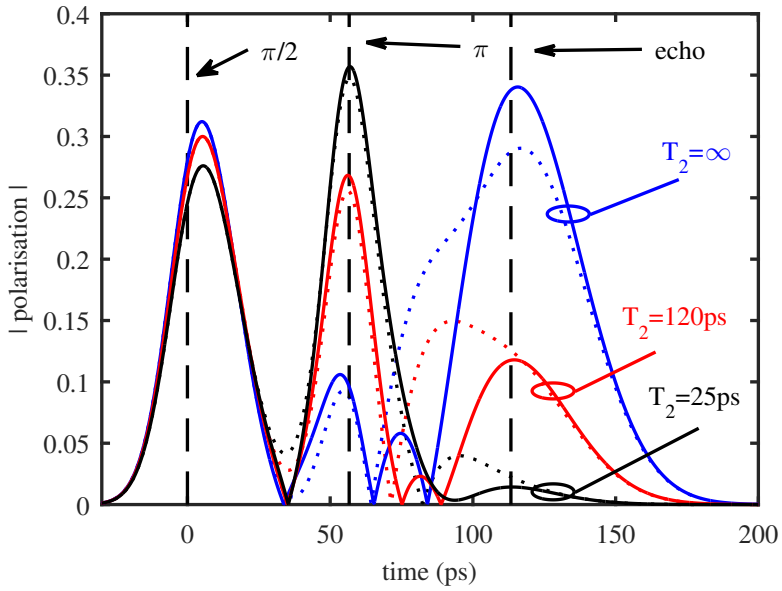

Figure 2.11: Polarization amplitude vs time for constructive interference (dotted) and destructive interference(solid) delays with $T_2 = \infty$ (blue), $T_2 = 120$ ps (red) and $T_2 = 25$ ps (black). The inter-pulse delay is 56ps, the (intensity) FWHM pulse duration is 17ps and other parameters are as in figure 2.5.

is desirable to push the techniques to measure dephasing times which approach the pulse duration and hence the phase sensitivity reported here would come into play. To explore if new information could be gained with knowledge of the interference condition we show in Fig. 2.11 the echo signal for constructive and destructive interference. using a range of T_2 values. The FWHM pulse duration is 17ps which corresponds to around 24 ps FWHM in the electric field. So with an inter-pulse delay of 56 ps there is still appreciable overlap between the CEP-pulses.

The echo signal for destructive interference is distinct and remains identifiable (but reduced in intensity) even for dephasing times similar to the field pulse duration. At constructive interference and for the longest dephasing times the echo peak positions are close to the expected location, whereas for shorter dephasing times the echo signal is mixed in a complex way with the driven polarization of the system. Unravelling what is echo signal and what is driven polarization is impossible preventing a T_2 determination. This suggests that to measure a fast dephasing time one should measure it using CEP pulses at delays corresponding to destructive interference. In essence one receives an advantage by using the destructive interference to shape the overlapping pulses into two shorter bursts of electric field.

2.7 Proof of principle experiment

In this section, we'll describe the proof of principle experiment(schematic in Fig. **??**) that our collaborators at University of Surrey performed. The aim was to measure photon echo not via the detection of the emitted light but via the polarisation of the donor electrons in the sample(Si:P) at the time of echo. The pulse sequence used was $\pi/2 - t_{12} - \pi - t_{23} - \pi/2 - t_{34} - Probe$. The echo was produced by the first two pulses. The second $\pi/2$ pulse arrives at the same time as the echo, projecting the polarisation into a definite state. The probe arriving some time later measures the ground state population. The echo signal produced by the first two pulses was scanned by the third pulse and then the transmission of the probe measured the ground state population.

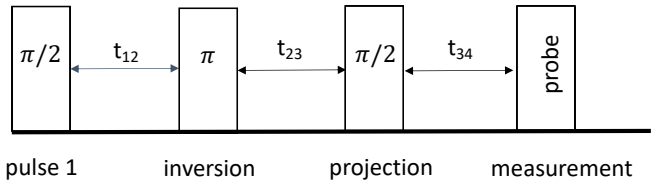

Figure 2.12: Schematic of photon echo experiment. The first pulse creates the signal, the second pulse reverses the polarisation vectors thus removing the inhomogeneous broadening effect, the third pulse projects the polarisation to population and the probe then measures the echo signal.

Fig. 2.13 shows the photocurrent(probe intensity) in arbitrary units for different values of t_{12}. The x-axis is t_{23} i.e. the third pulse($\pi/2$) that scans the echo. It is the processed experimental data. The legend identifiers correspond to the numbering scheme for the different delays. The last number in the legend is how many free space oscillations of the field are there between the first two pulses(i.e. constructive or destructive interference between the first two pulses). The curves have been offset vertically for clarity. The observations from Fig. 2.13 are summarised below.

1. The main feature of interest is the phase sensitivity of the echo signal at around 27ps. We see that for near a whole number of cycles in the delay there is an echo feature (blue and red) and for a half number of cycles this is washed out which is consistent with the theory.

2. The echo position in the red and blue cases is some 6ps earlier than a simple picture would suggest, which is also consistent with the effect of pulse overlap and dephasing.

3. For the longer delays of around 40 and 46 ps (black, yellow and cyan) it is hard to discern any clear feature which one could identify as an echo. With an optimistic eye one could posit a feature at 35ps in the black and yellow traces which behaves as expected ie whole number of cycle (yellow) trace is higher than the half integer number of cycles. The signal is however down in the noise level.

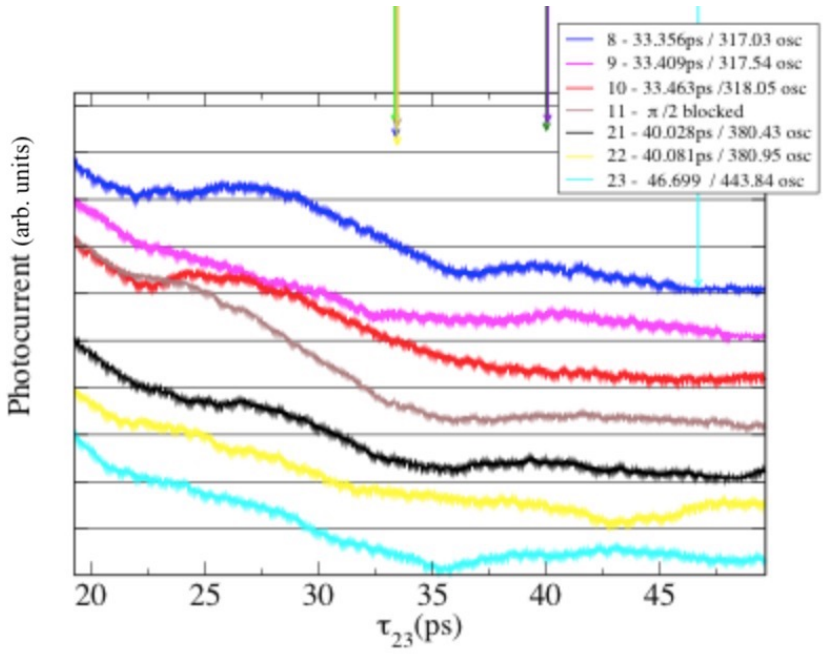

Figure 2.13: Photocurrent vs delay as a function of delay between the second pulse(π) and the third($\pi/2$) pulse for different τ_{12}. The probe scans the output of this echo experiment to measure the population. The arrows on the top of the figure points to the theoretically expected position of the photon echo.

Fig. 2.14 shows the curves for 8,9,10 from Fig. 2.13 plotted on the same scale. The fast oscillations in the photocurrent is due to the thin film interference effect. There are 3 points of interest in these curves at 15ps, 25ps and 40 ps. We're not sure of the reason for a bump around 15ps. One can infer that the bumps around 25ps looks like echo and matches with the theoretical expectation of observing an echo for constructive interference delays between the first two pulses and a washed out echo for destructive interference delay. The bump at 40ps in the green curve makes sense as for destructive interference the echo is always shifted to later times but the same happens for the blue curve (constructive interference case) which poses the question of whether this effect is

due to echo or there is some other explanation for these bumps. So given the bumps around 15ps and the blue curve bump around 40ps makes it difficult to draw conclusions.

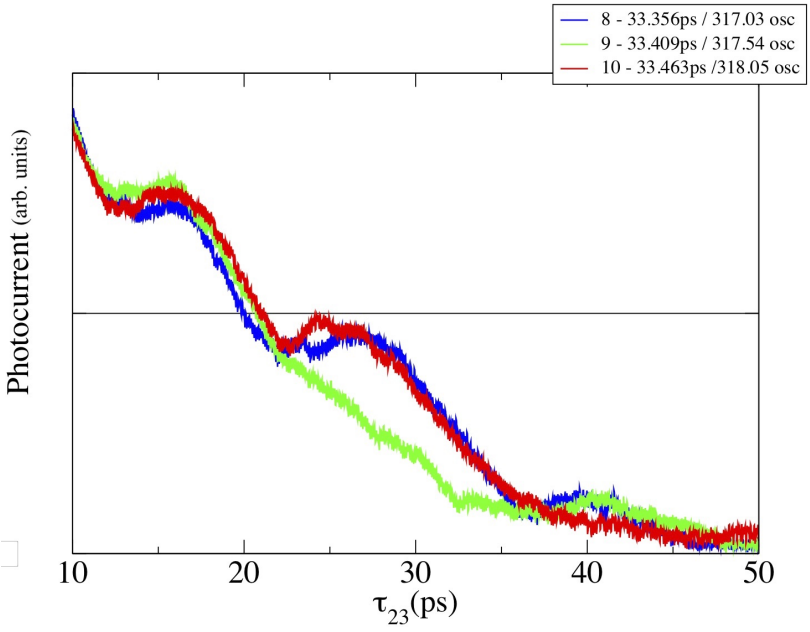

Figure 2.14: Selected plots from Fig. 2.13.

Fig. 2.15 shows the corresponding simulated curve. The theoretical observations are -

1. We can see that the echo appears for the constructive interference case while it is washed out for destructive interference case.

2. Comparing Fig. 2.15 with Fig. 2.14 with, we can say that the position of the echo do not match quantitatively.

These observations coupled with the unexplained bumps around 15ps and 40ps (blue curve) in Fig. 2.14 let us infer that assuming the bumps around 27ps are echo, the results are qualitatively consistent while quantitatively far from the theory. Therefore the results are not conclusive enough as a proof of principle experiment as it requires the assumption that the bump iaround 27ps is the echo signal while ignoring the bumps at earlier and later times.

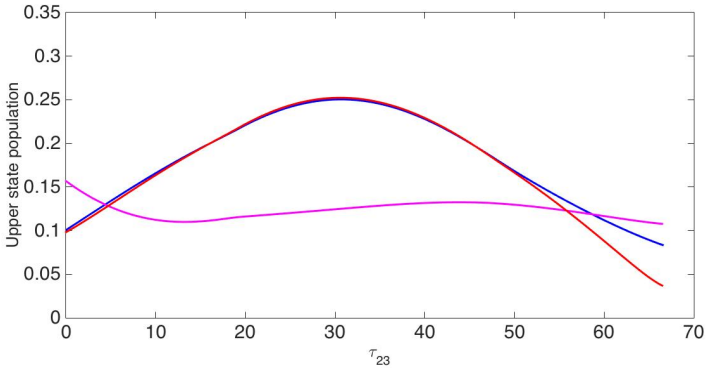

Figure 2.15: Theoretical plots for the same case as Fig. 2.14. Here blue and red corresponds to blue and red in Fig. 2.14 and magenta in this figure corresponds to green in Fig.2.14.

2.8 Conclusions

To conclude, we have shown numerically and analytically that when CEP pulses overlap, we see a strong phase dependence of the echo position(in time). Shifts of over 10 ps have been seen. The qualitative nature of this phase (delay) dependence changes depending on the pulse overlap area, pulse-width of the applied pulses, dephasing time and the inhomogeneous line-width of the system. In the case of well separated CEP pulses, the echo peak position (in time) is independent of the phase difference between the applied pulses. For all "normal" pulses, the echo peak position (in time) is insensitive to wavelength-scale changes of the delay between the applied pulses. In all cases, there is an inherent small shift in the echo peak position in time due to finite pulse-width of the applied pulses. Our results inform both the interpretation and design of ultrafast polarization relaxation measurements using photon echo techniques as they guide the interpretation of the measured signals when the pulses overlap. Making photon echo measurements in the destructive interference condition should allow the resolution of shorter dephasing times than in the constructive interference configuration.

Chapter 3

Analysis of an EIT Experiment in doped Silicon

3.1 Introduction

The coherent interaction of light with three or higher level systems can lead to interesting optical responses via quantum interference. Electromagnetically induced transparency(EIT) (a quantum interference phenomena that transforms an absorbing medium into a transparent medium for particular frequency), slow light and Autler-Townes Splitting(ATS) are some examples of this. There are different configurations of three-level systems depending on energy levels, the driving fields and optical matrix elements. The most common level schemes for a 3-level system with two driving fields are - ladder, Λ and V systems. This is shown in Fig 3.1. Loosely speaking the V scheme is an inverted Λ scheme.

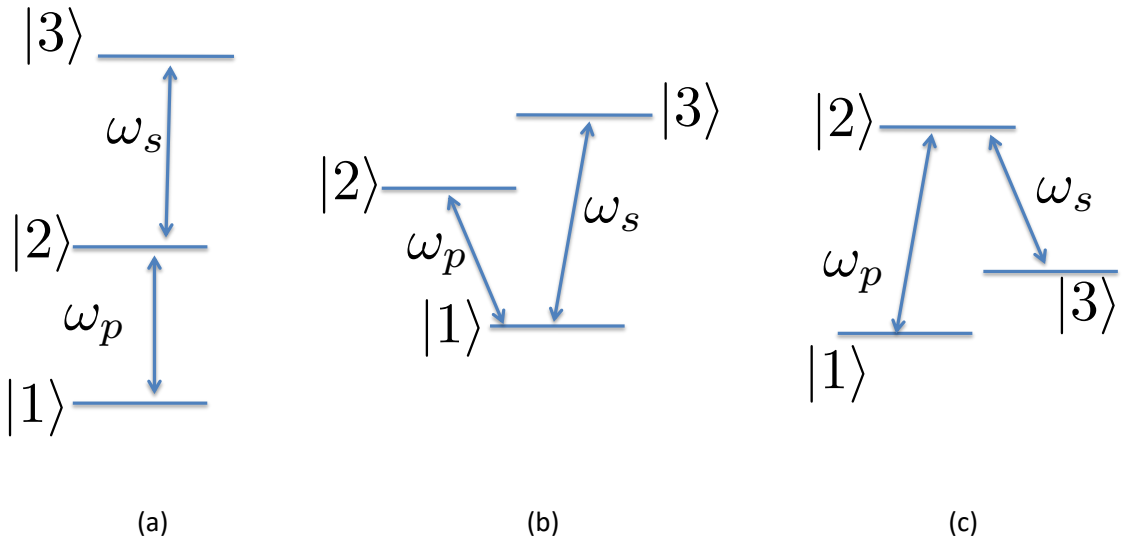

Figure 3.1: Different linkages of a 3-level system with two driving fields. a) ladder , b) V and c) Λ scheme. The ground state is only interacting with one state directly in the ladder and lambda scheme but to two states in V scheme.

ATS and EIT both result in a doublet structure in the absorption spectrum leading to a transparent window at resonance but the physics behind both is different. While the EIT is achieved by Fano interference between different excitation pathways and can be present even when the pump is arbitrarily weak, ATS happens only at high pump intensities even in the absence of Fano interference. EIT happens due to destructive interference of probability amplitudes of both transitions when the pump intensity is weaker than the probe doppler width while ATS is a gap induced between two absorption peaks when pump intensity is stronger than probe transition doppler width. Distinguishing between ATS and EIT in an experiment is challenging and there is literature reporting on measures which can be used to do that [36, 37]. EIT can be seen in a number of different three-level systems configurations but is hardest to see in the 'V' (Fig. 3.2) configuration because of emptying of the common ground state($|1\rangle$) with the strong pump beam [38].

In this chapter we analyse an initial EIT experiment by our collaborators at University of Surrey and explain why the experiment failed and then suggest some parameters where EIT can be observed in the Bismuth doped Silicon sample(Si:Bi). In the initial experiment, because of the transition frequencies, the sensitivity of detectors at different wavelengths and other experimental constraints a "V" system was chosen. The experiment was performed on the $1s-2p_{\pm}$ transition as probe(ω_s) and $1s-2p_0$ transition as pump(ω_p) in Si:Bi sample (see Fig. 3.2).

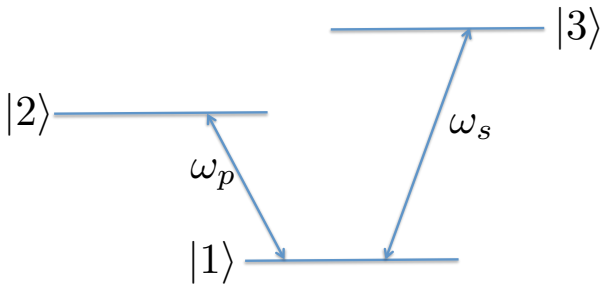

Figure 3.2: 3 level 'V' system

Our aim is to explain the absence of splitting in the EIT experiment as well as provide suggestions for future experiments to our collaborators at University of Surrey. The experiment is performed by keeping the pump beam constant(resonant to the $1s - 2p_0$ transition) and varying the probe beam wavelength. The probe beam was varied to four different wavelengths and at each wavelength the fractional transmission(with pump/without pump) was measured. Fig. 3.3 is a theoretical plot showing the four probe wavelengths for the experiment and the expected effect of EIT on the absorption of probe beam. From this figure, we can expect the absorption to drop for the wavelength 1 (black arrow), remain almost constant for wavelength 2 (red arrow) and increase for the wavelength 3 (blue arrow). We also do not expect to see a measurable signal at laser 4.

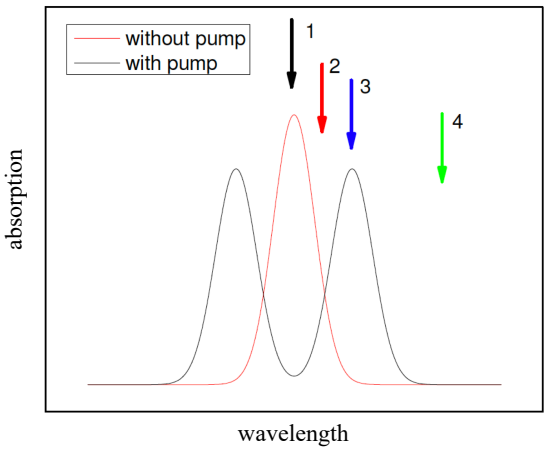

Figure 3.3: This figure shows the expected effect of EIT on the absorption of the probe beam(black curve). The absorption of the probe in the absence of the pump is shown by the red line. The four arrows show the chosen probe absorption wavelength for the experiment.

Fig. 3.4 shows the experimentally observed transmission values (with arbitrary units) for

the parameters in Fig. 3.3. We see that the transmission has increased for the resonant probe laser (black dots in Fig. 3.4 and black arrow in Fig. 3.3) with increasing pump intensity. The transmission remained almost constant for slightly off-resonant laser (red dots in Fig. 3.4 and red arrow in Fig. 3.3) and the transmission decreased for the further off-resonant laser (blue dots in Fig. 3.4 and blue arrow in Fig. 3.3). As expected there was no measurable signal for the laser 4. We can see that the results for the different probe wavelengths are in line with the expected results from EIT but from this figure alone, we cannot infer the observation of EIT.

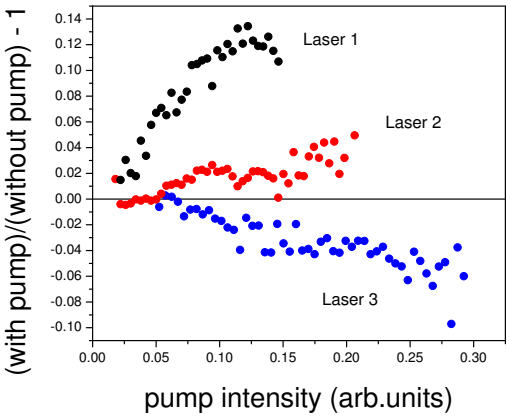

Figure 3.4: Fractional transmission of probe at different wavelengths (as shown by arrows in Fig. 3.3) with varying pump intensity.

The problem of inference in the experiment is that the fractional transmission is measured at 3 different laser frequencies and absorption is plotted by subtracting the transmission change from unity. A decrease in this fractional absorption is measured on resonance while an increase was measured at the off resonance position. From this alone it is not possible to say if there is a splitting or just broadening and reduction at the line centre. Therefore, we looked at the parameter space in which the experiment was performed and checked whether it was even possible to see EIT at those parameters. Our investigation suggested that the parameters for the experiment would not have resulted in EIT and we also suggested general guidelines to choose parameters for such an experiment.

3.2 Bloch equations

We begin by deriving Bloch-equations for a three-level system. Consider the laser's electric field to be

$$\mathbf{E}(t) = \varepsilon_p(t)Re(e^{-i\omega_p t+i\phi_p}\hat{e}_p) + \varepsilon_s(t)Re(e^{-i\omega_s t+i\phi_s}\hat{e}_s), \tag{3.1}$$

where $\omega_{p,s}$ are the carrier frequencies, $\phi_{p,s}$ are the phases, $\varepsilon_{p,s}$ are the pulse envelopes and $\hat{e}_{p,s}$ are the complex unit vectors. The general wavefunction of the whole system can be written as

$$\psi(t) = C_1(t)e^{-i\zeta_1(t)}\psi_1 + C_2(t)e^{-i\zeta_2(t)}\psi_2 + C_3(t)e^{-i\zeta_3(t)}\psi_3, \tag{3.2}$$

where the time dependent phases are explicitly introduced to eliminate explicit appearance of time varying rapid oscillations terms in the Bloch equations by choosing the values of these phases. Now, the interaction between laser pulses and the system can be described by

$$V = -\mathbf{d}\cdot\mathbf{E}(t). \tag{3.3}$$

where, $\mathbf{d}$ is the dipole moment between the levels. The overall Hamiltonian matrix for the system is given by

$$H = \begin{bmatrix} E_1+V_{11} & V_{12} & V_{13} \\ V_{21} & E_2+V_{22} & V_{23} \\ V_{31} & V_{32} & E_3+V_{33} \end{bmatrix},$$

Applying Schrodinger's Equation,

$$i\hbar\frac{d\psi}{dt} = H\psi, \tag{3.4}$$

$$i\hbar\frac{d}{dt}\begin{bmatrix} C_1(t)e^{-i\zeta_1(t)} \\ C_2(t)e^{-i\zeta_2(t)} \\ C_3(t)e^{-i\zeta_3(t)} \end{bmatrix} = \begin{bmatrix} E_1+V_{11} & V_{12} & V_{13} \\ V_{21} & E_2+V_{22} & V_{23} \\ V_{31} & V_{32} & E_3+V_{33} \end{bmatrix}\begin{bmatrix} C_1(t)e^{-i\zeta_1(t)} \\ C_2(t)e^{-i\zeta_2(t)} \\ C_3(t)e^{-i\zeta_3(t)} \end{bmatrix},$$

$$i\hbar\begin{bmatrix} \dot{C}_1(t)e^{-i\zeta_1(t)} - i\dot{\zeta}_1 C_1(t)e^{-i\zeta_1(t)} \\ \dot{C}_2(t)e^{-i\zeta_2(t)} - i\dot{\zeta}_2 C_2(t)e^{-i\zeta_2(t)} \\ \dot{C}_3(t)e^{-i\zeta_3(t)} - i\dot{\zeta}_3 C_3(t)e^{-i\zeta_3(t)} \end{bmatrix} =$$

$$\begin{bmatrix} (E_1+V_{11})e^{-i\zeta_1(t)}C_1(t) & V_{12}e^{-i\zeta_2(t)}C_2(t) & V_{13}e^{-i\zeta_3(t)}C_3(t) \\ V_{21}e^{-i\zeta_1(t)}C_1(t) & (E_2+V_{22})e^{-i\zeta_2(t)}C_2(t) & V_{23}e^{-i\zeta_3(t)}C_3(t) \\ V_{31}e^{-i\zeta_1(t)}C_1(t) & V_{32}e^{-i\zeta_2(t)}C_2(t) & (E_3+V_{33})e^{-i\zeta_3(t)}C_3(t) \end{bmatrix},$$

Equating both sides we get,

$$\begin{aligned} i\hbar\dot{C}_1(t)e^{-i\zeta_1(t)} &= (E_1+V_{11}-\hbar\dot{\zeta}_1)e^{-i\zeta_1(t)}C_1(t)+V_{12}e^{-i\zeta_2(t)}C_2(t)+V_{13}e^{-i\zeta_3(t)}C_3(t), \\ \dot{C}_1 &= -\frac{i}{\hbar}[(E_1+V_{11}-\hbar\dot{\zeta}_1)C_1(t)+V_{12}e^{i(\zeta_1(t)-\zeta_2(t))}C_2(t)+V_{13}e^{i(\zeta_1(t)-\zeta_3(t))}C_3(t)]. \end{aligned}$$

Similarly,

$$\begin{aligned} \dot{C}_2 &= -\frac{i}{\hbar}[V_{21}e^{i(\zeta_2(t)-\zeta_1(t))}C_1(t)+(E_2+V_{22}-\hbar\dot{\zeta}_2)C_2(t)+V_{23}e^{i(\zeta_2(t)-\zeta_3(t))}C_3(t)], \\ \dot{C}_3 &= -\frac{i}{\hbar}[V_{31}e^{i(\zeta_3(t)-\zeta_1(t))}C_1(t)+V_{32}e^{i(\zeta_3(t)-\zeta_2(t))}C_2(t)+(E_3+V_{33}-\hbar\dot{\zeta}_3)C_3(t)]. \end{aligned}$$

Leading to,

$$\begin{bmatrix} \dot{C}_1 \\ \dot{C}_2 \\ \dot{C}_3 \end{bmatrix} = -\frac{i}{\hbar}\begin{bmatrix} W_{11} & W_{12} & W_{13} \\ W_{21} & W_{22} & W_{23} \\ W_{31} & W_{32} & W_{33} \end{bmatrix}\begin{bmatrix} C_1 \\ C_2 \\ C_3 \end{bmatrix}, \tag{3.5}$$

where,

$$W = \begin{bmatrix} (E_1+V_{11}-\hbar\dot{\zeta}_1) & V_{12}e^{i(\zeta_1(t)-\zeta_2(t))} & V_{13}e^{i(\zeta_1(t)-\zeta_3(t))} \\ V_{21}e^{i(\zeta_2(t)-\zeta_1(t))} & (E_2+V_{22}-\hbar\dot{\zeta}_2) & V_{23}e^{i(\zeta_2(t)-\zeta_3(t))} \\ V_{31}e^{i(\zeta_3(t)-\zeta_1(t))} & V_{32}e^{i(\zeta_3(t)-\zeta_2(t))} & (E_3+V_{33}-\hbar\dot{\zeta}_3) \end{bmatrix}. \tag{3.6}$$

Now we will do the calculation for the interaction term V(defined in Eq. 3.3)

$$d_{12} = \langle 1|\vec{d}.\hat{e}_p|2\rangle, \tag{3.7}$$

$$d_{13} = \langle 1|\vec{d}.\hat{e}_s|3\rangle, \tag{3.8}$$

$$V_{12} = -\frac{1}{2}\varepsilon_p(t)(d_{12}e^{-i\omega_p t+i\phi_p}+d_{21}e^{i\omega_p t-i\phi_p}), \tag{3.9}$$

$$V_{13} = -\frac{1}{2}\varepsilon_s(t)(d_{13}e^{-i\omega_s t+i\phi_s}+d_{31}e^{i\omega_s t-i\phi_s}). \tag{3.10}$$

In our case $V_{23} = 0$ (dipole forbidden transition). In the "V" scheme we can choose the arbitrary phases ζ so as to make the calculations convenient.

$$\hbar\dot{\zeta_1} = \hbar\dot{\zeta_2} - \hbar\omega_p, \tag{3.11}$$

$$\hbar\dot{\zeta_2} = E_2 + V_{22}, \tag{3.12}$$

$$\hbar\dot{\zeta_3} = \hbar\dot{\zeta_2} - \hbar\omega_s. \tag{3.13}$$

Thus,

$$\zeta_2 = \zeta_1 + \omega_p t + \phi_2, \tag{3.14}$$

$$\zeta_3 = \zeta_2 - \omega_s t + \phi_3 = \zeta_1 + \omega_p t - \omega_s t + \phi_2 + \phi_3. \tag{3.15}$$

Also defining Rabi frequencies as

$$\Omega_p = -d_{12}\varepsilon_p/\hbar, \tag{3.16}$$

$$\Omega_s = -d_{23}\varepsilon_s/\hbar, \tag{3.17}$$

we get

$$W_{12} = -\frac{\Omega_p}{2}(e^{-2i\omega_p t + i\phi_p - i\phi_2}) - \frac{\Omega_p^*}{2}(e^{-i\phi_p - i\phi_2}) = W_p^*, \tag{3.18}$$

$$W_{23} = -\frac{\Omega_s}{2}(e^{i\phi_s - i\phi_3}) - \frac{\Omega_p^*}{2}(e^{2i\omega_s t - i\phi_s - i\phi_3}) = W_s. \tag{3.19}$$

Hence,

$$W = \begin{bmatrix} 0 & W_p^* & 0 \\ W_p & \Delta_p & W_s \\ 0 & W_s^* & \Delta_p - \Delta_s \end{bmatrix}, \tag{3.20}$$

where,

$$\Delta_p = (E_2 + V_{22} - E_1 - V_{11} - \hbar\omega_p), \tag{3.21}$$

$$\Delta_s = (E_2 + V_{22} - E_3 - V_{33} - \hbar\omega_s), \tag{3.22}$$

are the detunings.

3.2.1 Calculation of the density matrix

We now calculate the density matrix of our system. Later we will calculate the Bloch equations for the density matrix of the system as it is straightforward to add dephasing time/loss from states(thermal etc.) in the density matrix formulation.

$$|\psi(t)\rangle = C_1(t)e^{-i\zeta_1(t)}|\psi_1\rangle + C_2(t)e^{-i\zeta_2(t)}|\psi_2\rangle + C_3(t)e^{-i\zeta_3(t)}|\psi_3\rangle, \tag{3.23}$$

$$\langle\psi(t)| = C_1^*(t)e^{i\zeta_1(t)}\langle\psi_1| + C_2^*(t)e^{i\zeta_2(t)}\langle\psi_2| + C_3^*(t)e^{i\zeta_3(t)}\langle\psi_3|, \tag{3.24}$$

$$\rho(t) = |\psi(t)\rangle\langle\psi(t)| = \begin{bmatrix} C_1(t)C_1^*(t) & e^{i(\zeta_2-\zeta_1)}C_1(t)C_2^*(t) & e^{i(\zeta_3-\zeta_1)}C_1(t)C_3^*(t) \\ e^{i(\zeta_1-\zeta_2)}C_2(t)C_1^*(t) & C_2(t)C_2^*(t) & e^{i(\zeta_3-\zeta_2)}C_2(t)C_3^*(t) \\ e^{i(\zeta_1-\zeta_3)}C_3(t)C_1^*(t) & e^{i(\zeta_2-\zeta_3)}C_3(t)C_2^*(t) & C_3(t)C_3^*(t) \end{bmatrix},$$

where ζ are defined above. As an example, the polarization term between $|1\rangle$ and $|2\rangle$ corresponds to

$$e^{i(\zeta_2-\zeta_1)}C_1C_2^* = e^{i(\omega_p t+\phi_2)}C_1C_2^*. \tag{3.25}$$

Therefore,

$$\hbar\frac{d}{dt}C_1 = -iW_p^*C_2, \tag{3.26}$$

$$\hbar\frac{d}{dt}C_1^* = iC_2^*W_p, \tag{3.27}$$

$$\hbar\frac{d}{dt}C_2 = -i(W_pC_1 + \Delta_pC_2 + W_sC_3), \tag{3.28}$$

$$\hbar\frac{d}{dt}C_2^* = i(C_1^*W_p^* + C_2^*\Delta_p^* + C_3^*W_s^*), \tag{3.29}$$

$$\hbar\frac{d}{dt}C_3 = -i(W_s^*C_2 + (\Delta_p - \Delta_s)C_3), \tag{3.30}$$

$$\hbar\frac{d}{dt}C_3 = i(C_2^*W_s + C_3^*(\Delta_p^* - \Delta_s^*)). \tag{3.31}$$

Therefore,

$$\hbar\frac{d}{dt}(C_1) = -iW_p^*C_2, \tag{3.32}$$
$$\hbar\frac{d}{dt}(C_1)C_1^* = -iW_p^*C_2C_1^*, \tag{3.33}$$
$$\hbar\frac{d}{dt}(C_1C_1^*) - \hbar C_1\frac{dC_1^*}{dt} = -iW_p^*C_2C_1^*, \tag{3.34}$$

$$\hbar\frac{d}{dt}(C_1C_1^*) = C_1iC_2^*W_p - iW_p^*C_2C_1^*, \tag{3.35}$$
$$\hbar\frac{d}{dt}(C_1C_1^*) = i(C_1C_2^*W_p - W_p^*C_2C_1^*). \tag{3.36}$$

Similarly, multiplying equation 4.26 by C_2^* we get,

$$\hbar\frac{d}{dt}(C_1)C_2^* = -iW_p^*C_2C_2^*, \tag{3.37}$$
$$\hbar\frac{d}{dt}(C_1C_2^*) - \hbar C_1\frac{d}{dt}C_2^* = -iW_p^*C_2C_2^*, \tag{3.38}$$
$$\begin{aligned}\hbar\frac{d}{dt}(C_1C_2^*) &= iC_1(C_1^*W_p^* + C_2^*\Delta_p^* + C_3^*W_s^*) - iW_p^*C_2C_2^*,\\ &= iW_p^*(|C_1|^2 - |C_2|^2) + iC_1C_2^*\Delta_p^* + iC_1C_3^*W_s^*.\end{aligned} \tag{3.39}$$

Similarly the other equations are derived -

$$\hbar\frac{d}{dt}(C_1C_1^*) = i(C_1C_2^*W_p - W_p^*C_2C_1^*), \tag{3.40}$$
$$\hbar\frac{d}{dt}(C_2C_2^*) = i[(C_2C_1^*W_p^* - W_pC_1C_2^*) + (C_2C_3^*W_s^* - W_sC_3C_2^*)], \tag{3.41}$$
$$\hbar\frac{d}{dt}(C_3C_3^*) = i(C_3C_2^*W_s - W_s^*C_2C_3^*), \tag{3.42}$$
$$\hbar\frac{d}{dt}(C_1C_2^*) = iW_p^*(|C_1|^2 - |C_2|^2) + iC_1C_2^*\Delta_p^* + iC_1C_3^*W_s^*, \tag{3.43}$$
$$\hbar\frac{d}{dt}(C_1C_3^*) = iC_1C_3^*(\Delta_p - \Delta_s) + iC_1C_2^*W_s - iW_p^*C_2C_3^*, \tag{3.44}$$
$$\hbar\frac{d}{dt}(C_2C_3^*) = iW_s(|C_2|^2 - |C_3|^2) - iW_pC_1C_3^* - i\Delta_sC_2C_3^*. \tag{3.45}$$

Now to reflect the physical meaning behind the Bloch equations, we use the following

nomenclature -

$$P_{12} = e^{i(\zeta_2-\zeta_1)}C_1C_2^*, \tag{3.46}$$
$$P_{13} = e^{i(\zeta_3-\zeta_1)}C_1C_3^*, \tag{3.47}$$
$$P_{23} = e^{i(\zeta_3-\zeta_2)}C_2C_3^*, \tag{3.48}$$
$$n_1 = C_1C_1^*, \tag{3.49}$$
$$n_2 = C_2C_2^*, \tag{3.50}$$
$$n_3 = C_3C_3^*. \tag{3.51}$$

Since,

$$\zeta_2 = \zeta_1 + \omega_p t + \phi_2, \tag{3.52}$$
$$\zeta_3 = \zeta_2 - \omega_s t + \phi_3 = \zeta_1 + \omega_p t - \omega_s t + \phi_2 + \phi_3, \tag{3.53}$$
$$\phi_2 = 0 = \phi_3. \tag{3.54}$$

We have,

$$P_{12} = e^{i\omega_p t}C_1C_2^*, \tag{3.55}$$
$$P_{13} = e^{i(\omega_p t-\omega_s t)}C_1C_3^*, \tag{3.56}$$
$$P_{23} = e^{-i(\omega_s t)}C_2C_3^*. \tag{3.57}$$

Using the same approach (i.e multiplying by a factor and then solving the derivates to get the desired equations the final results in this nomenclature are)

$$\hbar\frac{d}{dt}n_1 = ie^{-i\omega_p t}[P_{12}W_p - W_p^*P_{12}^*], \tag{3.58}$$
$$\hbar\frac{d}{dt}n_3 = ie^{i\omega_s t}[P_{23}^*W_s - W_s^*P_{23}], \tag{3.59}$$
$$\hbar\frac{d}{dt}n_2 = -ie^{-i\omega_p t}[P_{12}W_p - W_p^*P_{12}^*] - ie^{i\omega_s t}[P_{23}^*W_s - W_s^*P_{23}], \tag{3.60}$$
$$\hbar\frac{d}{dt}P_{12} = i[P_{12}(\Delta_p + \omega_p) + e^{i\omega_p t}W_p^*(n_1 - n_2) + e^{i\omega_s t}P_{13}W_s^*], \tag{3.61}$$
$$\hbar\frac{d}{dt}P_{13} = i[(\Delta_p + \omega_p - \Delta_s - \omega_s)P_{13} + e^{-i\omega_s t}P_{12}W_s - e^{i\omega_p t}P_{23}W_p^*], \tag{3.62}$$
$$\hbar\frac{d}{dt}P_{23} = i[e^{-i\omega_s t}W_s(n_2 - n_3) - (\Delta_s + \omega_s)P_{23} - W_pP_{13}e^{-i\omega_p t}]. \tag{3.63}$$

3.3 Numerical simulations of 3-level 'V' system

In this section we present the numerical simulations of a three-level system interacting with laser pulses. The parameters used in these simulations are chosen according to the exprimental requirements from our collaborators at University of Surrey i.e. the experiment was performed on $1s-2p_{\pm}$ transition as probe and $1s-2p_0$ transition as pump in a Si:Bi sample.

$|1\rangle$ - $|2\rangle$ transition frequency - 14.39 THz,

$|1\rangle$ - $|3\rangle$ transition frequency - 15.62 THz,

$|2\rangle$ population decay rate (τ_{12}) - 6.5 ps,

$|3\rangle$ population decay rate (τ_{13}) - 26 ps,

unless otherwise mentioned. Gaussian pulses of 1.5ps FWHM (in electric field) or equivalently 1.06ps (in intensity) are used. The population is measured 15ps after the application of the pulses. There are two ways to observe EIT -

1. Excited state population vs detuning plots for various intensities of pump-probe pulses.

2. Fourier transform of polarisation (P(t)) to produce the absorption spectrum.

We have investigated the differences and similarities of both approaches to help understand the experimental failure to observe EIT.

Fig. 3.5 shows the splitting and dip in the absorption spectrum by plotting the population of level 3(n_3) against the probe detuning(Δ_p) when the pump intensity is varied while keeping the probe intensity constant. We can see that for the same probe intensity, higher pump intensity results in splitting of absorption profile. This suggests that for a constant probe intensity there might be a threshold pump intensity, above which the absorption(population in excited state) line splits and results in very low absorption near resonance while high absorption at certain probe detunings.

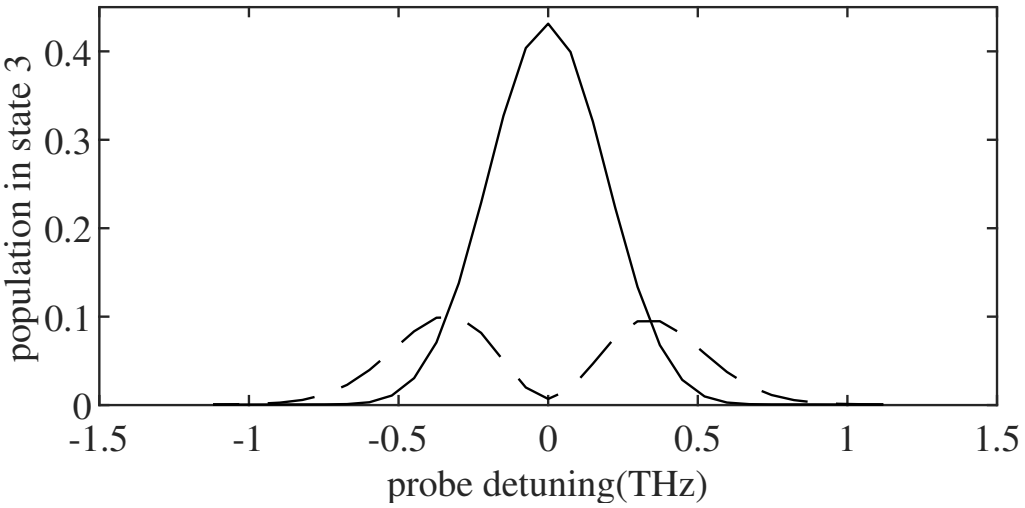

Figure 3.5: Population in state 3 vs detuning for probe intensity $= \pi/2$ THz, solid line - pump intensity$= \pi/20$ and dotted line - pump intensity$= 2\pi$

To observe this we calculate the population of level 3 (n_3) with respect to pump intensity and probe detuning which is shown in Fig. 3.6 for constant probe intensity.

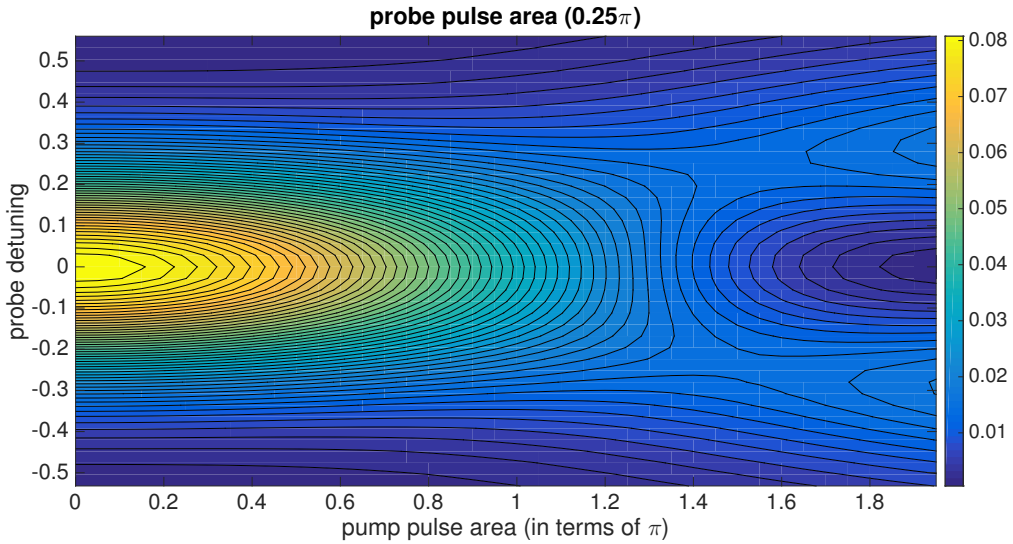

Figure 3.6: Heatmap of population in state 3 as a function of pump intensity and probe detuning.

It shows that, near resonance, as we increase the pump intensity the population decreases in state 3 but far from resonance we see an increase in population in state 3 as we increase the pump intensity. We can also see the peaks of the splitting appearing around probe detuning of ± 0.3THz. These behaviours can also be seen in Fig. 3.5 for particular pump and probe intensity. Also, for particular detuning frequency the population decreases but only for pump intensity less than a certain value (dependent on the Rabi frequencies of the applied fields), after which the population increases near that particular detuning thus

implying splitting with minimum absorption at resonance i.e EIT.

Since the population vs detuning plot is not an actual absorption spectrum (it is actually a convolution of probe pulse with the absorption line and thus depends on the probe pulse width), we calculated the absorption spectrum of the weak probe pulse (ω_s) in presence of a strong pump pulse (ω_p). The three level Bloch equations with Lindblad dephasing terms are numerically solved in time. The pump and probe pulses have their centre frequencies tuned to the resonance frequencies of the two transitions in Fig. 3.2. Both pulses are dipole coupled to both of the transitions (but are off-resonance with one). This means, for long pulses each pulse only couples to one transition but for short(spectrally broad) pulses there is coupling to both transitions from both pulses. First the polarisation, $P_p(t)$, of the system was calculated in the case when there is no probe pulse. Then the total polarisation, $P_{p+s}(t)$ is calculated with a finite weak probe and the difference between these two polarisations, $\Delta P(t) = P_{p+s}(t) - P_p(t)$, gives the polarisation induced by the probe pulse. Then the Fourier transform of this induced polarisation change, ΔP, is calculated and divided by the Fourier transform of the probe field to get the probe susceptibility. The imaginary part of the probe susceptibility is proportional to the probe absorption [39]. This is equivalent to using the probe pulse as a weak continuum source to measure the linear absorption. Another approach is to measure the population in the system and plot it against probe detuning. Both of these approaches result in similar results with CW pump and weak gaussian probe pulse (the only difference is that the population vs detuning plots are governed by probe pulse-width i.e the spectral overlap between the probe and the transition) but they differ in case of short pump and short probe which was the regime in which the experiment was done.

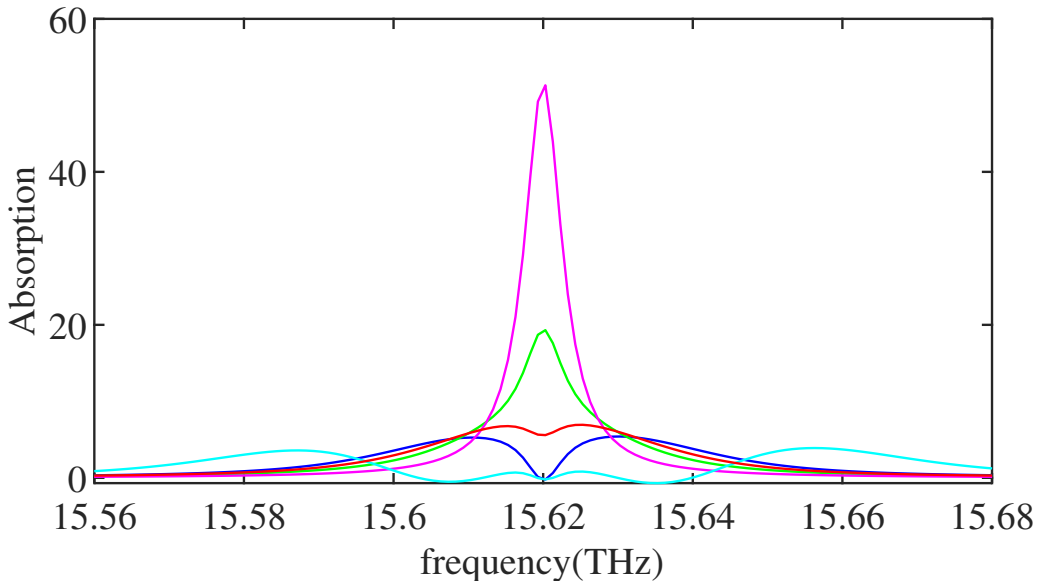

Figure 3.7: Probe absorption spectra for various pump intensities. The pulse-widths quoted are FWHM of the intensity profile. The parameters are - probe pulsewidth = 1.5ps, pump pulsewidth=50ps, τ_{12}=6.5ps, τ_{13}=26ps, probe intensity = 0.0695THz radians, The pump intensities are. - cyan(0.5 THz-rad), blue(0.2 THz-rad), red(0.15 THz-rad), green(0.1 THz-rad) and magenta(0.0 THz-rad)

Fig. 3.7 shows the absorption spectra of the 'V' system for different pump intensities using a long pump pulse to simulate the usual CW treatments of EIT. We see that the splitting appears as we increase the pump intensity. At the line centre gain (negative absorption) can develop, which is the source of the lasing without inversion [40] phenomenon. For these pulses the magnitude of the splitting is still affected by the finite pulse duration and is not exactly twice the Rabi frequency. Doing simulations for longer pump pulses (>250ps) recovers this limit correctly.

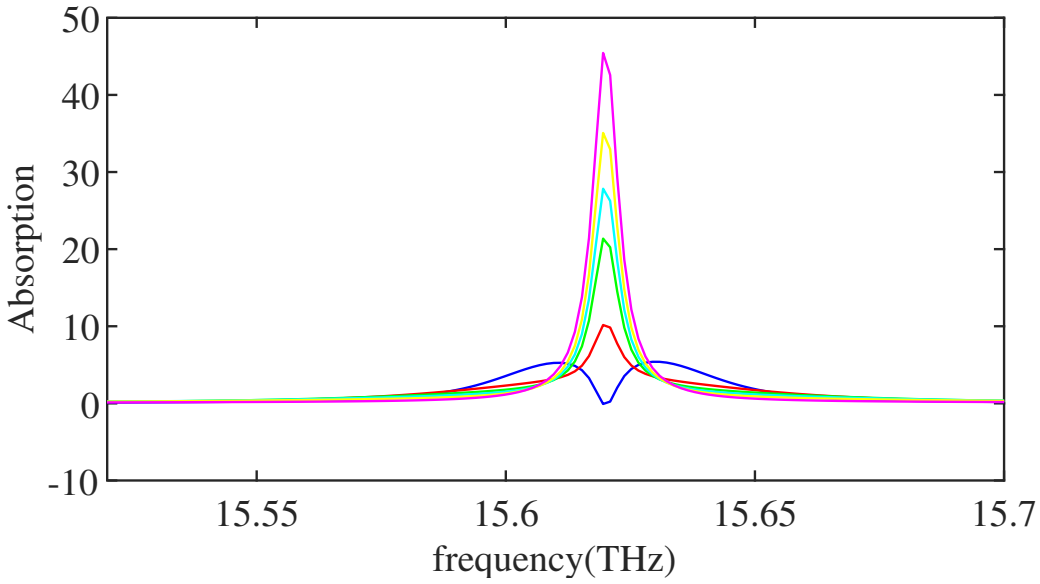

Figure 3.8: Probe absorption spectra for various pump pulse widths. The pulse-widths quoted are FWHM of the intensity profile. The parameters are - probe pulsewidth = 1.5ps, τ_{12}=6.5ps, τ_{13}=26ps, probe intensity = 0.0695THz radians, pump intensity = 0.2 THz-rad. The pump pulse-widths are - blue(50 ps), red(15 ps), green(10 ps), cyan(8 ps), yellow(6 ps) and magenta(3 ps)

In Fig. 3.8 we show the effect of changing the pump pulse-width on the absorption spectrum keeping other parameters as in Fig. 3.7. We see that the splitting disappears as we decrease the pump pulse-width. In fact this is the main reason why the the experiment failed. The short pulses in the experiment doesn't result in any splitting in the absorption spectrum as shown in Fig. 3.8. The same experiment with a quasi-CW pulses results in expected splitting behaviour. The reasons for the strong pulse width dependence lie in a combination of the broader spectral spread of the pump pulse (hence coupling directly to both transitions), the changing of the pump intensity during the probe pulse, hence smearing out any splitting and the pump pulse length in time being comparable to the dephasing times.

3.4 Summary and suggestions for experiment

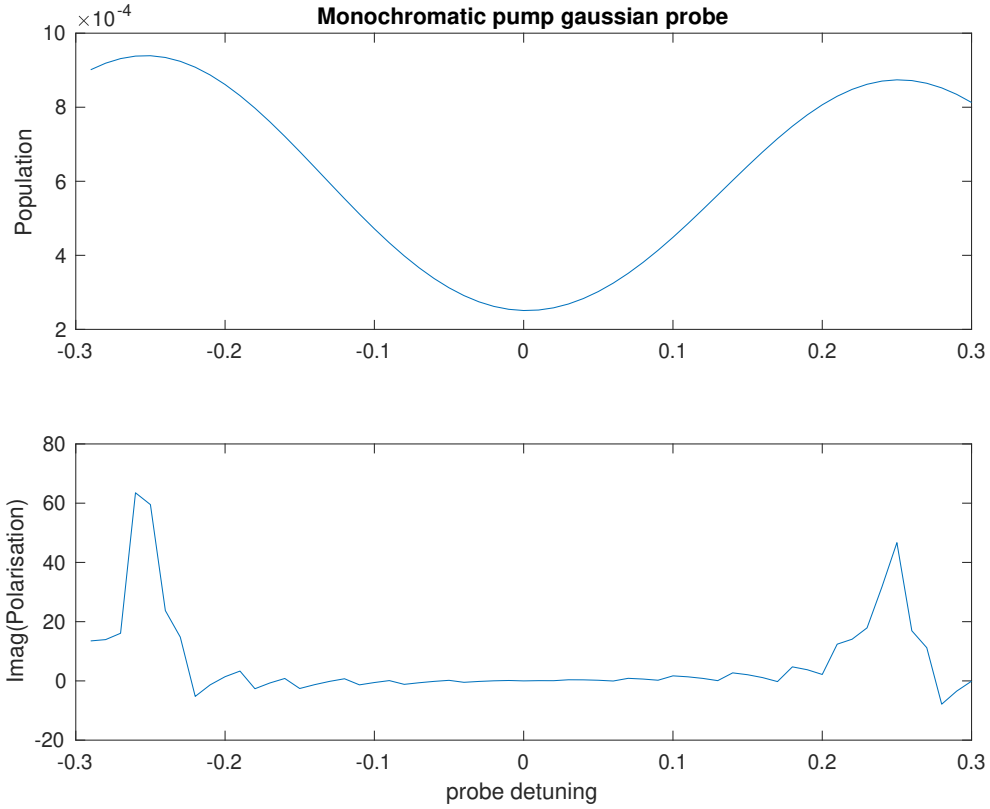

Figure 3.9: top: Population vs detuning, bottom: Susceptibility vs frequency plots for a continuous wave pump and weak gaussian probe. We see that the two approaches results in same splitting around ± 0.25. We also notice that the bottom plot is very noisy, this is due to the resolution being low in this case. This is the regime where EIT can be observed in experiments.

We took two approaches to understand the experiment. One based on susceptibility calculation from polarisation and other on population vs detuning plots. Here are our observation/findings -

1. The issue was that the results from the population vs detuning approach weren't matching(the peaks were at different frequencies) the results from the susceptibility approach in case of the experimental parameters i.e short pump and short probe. Fig. 3.9 shows that both approaches agree when the pump is a monochromatic (CW) pulse while the probe is a weak gaussian pulse.

2. Also, as we increase the gaussian pulse-width of the pump (in the time domain) for a fixed intensity the EIT splitting approaches the exact value of the Rabi frequency. This suggests that the difference in the two approaches (population calculation and

susceptibility calculation) arises because of the pulse-width and hence spectral width of the pump.

3. To observe EIT in a "V" systems it is imperative that we use a very long pump pulse(more than FWHM 50ps) and a weak/short gaussian probe pulse (around FWHM 1.5 ps). Short pump pulse experiments can give rise to the splitting seen in the population of the excited state but are not EIT in the conventional sense as they arise also from the direct pumping of the second level by the pump.

3.5 Motivation for non-hermitian quantum mechanics

The difficulties of experimental realisations of theoretical hypotheses piqued our interest and we changed our focus towards investigating real systems with gains and losses. Instead of phenomenologically adding losses to the Bloch equation the idea of deriving lossy Bloch equations from non-hermitian hamiltonian drove our interest towards Non-Hermitian Quantum Mechanics. The rest of the thesis will focus on non-hermitian quantum mechanics with the aim of taking advantage of the losses in the system to uncover interesting physics and find a regime where losses might be important for experimental realisation of optical phenomena, if possible. Here we report the results for a three-level systems using a non-hermitian hamiltonian formalism rather than the general approach of hermitian system with phenomenologically added losses in Bloch equations. We have chosen a Λ system interacting with two lasers for this simulation as shown in Fig. 3.10.

The non-hermitian hamiltonian for this system can be written as -

$$H = \begin{bmatrix} 0 & \Omega & 0 \\ \Omega & \Delta_1 - i\gamma_1 & \kappa \\ 0 & \kappa & \Delta_2 - i\gamma_2 \end{bmatrix}, \tag{3.64}$$

where $\gamma_{1,2}$ describes the losses in the system, Ω, κ describes the laser interaction with the system and $\Delta_{1,2}$ are the detuning frequencies. The most general state of the system can be is -

$$\psi(t) = C_0(t)\psi_0 + C_1(t)\psi_1 + C_2(t)\psi_2, \tag{3.65}$$

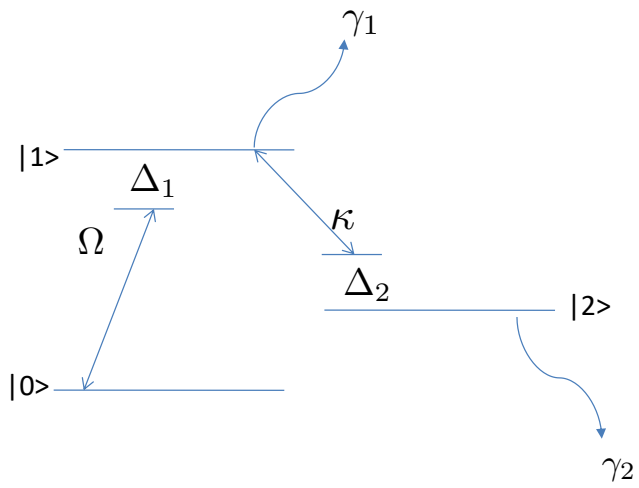

Figure 3.10: Λ system

where $\psi_{0,1,2}$ are the vectors in the natural basis. Applying Schrödinger's equation we get,

$$\hbar \frac{d}{dt} \begin{bmatrix} C_0 \\ C_1 \\ C_2 \end{bmatrix} = -i \begin{bmatrix} 0 & \Omega & 0 \\ \Omega & \Delta_1 - i\gamma_1 & \kappa \\ 0 & \kappa & \Delta_2 - i\gamma_2 \end{bmatrix} \begin{bmatrix} C_0 \\ C_1 \\ C_2 \end{bmatrix} \tag{3.66}$$

We use (3.66) for numerical simulations.

We have chosen a simple case where both the transitions are resonant i.e. $(\Delta_{1,2} = 0)$. Fig. 3.11 shows that the populations of all three levels in the absence of losses. We can see that the population in level one is never more than half the total population with twice the frequency of oscillations(because level one is directly interacting with two states) compared to the populations in other states(direct interaction with only one state) which is in line with the general results usually obtained via hermitian systems with phenomenologically added losses [41]

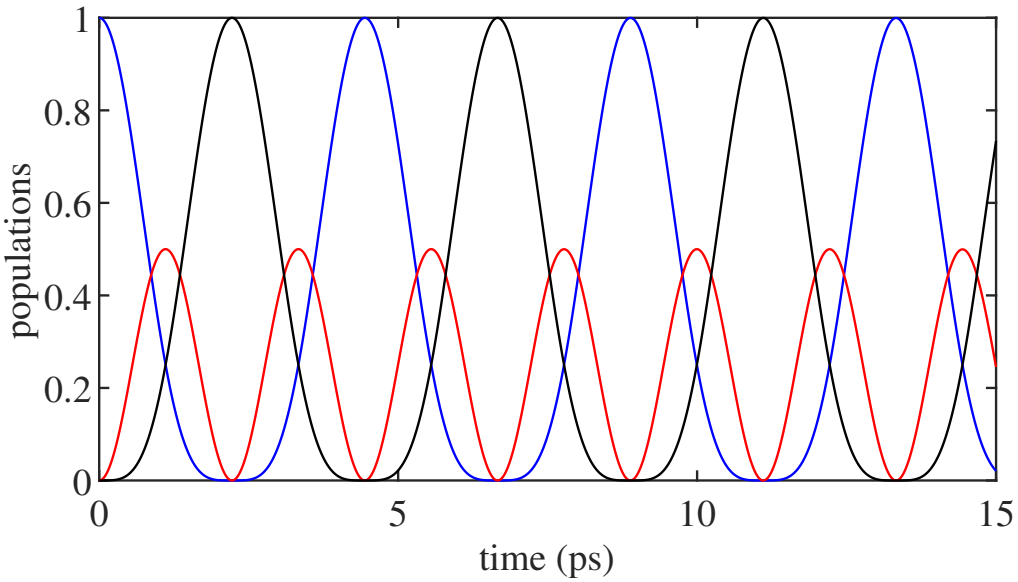

Figure 3.11: Population vs time for a three level Λ system with parameters - Ω=$\kappa = 1$ THz, Δ_1=Δ_2=0 THz and $\gamma_1 = \gamma_2 = 0$ THz.

Fig. 3.12 is the case when there is a finite loss ($\gamma_2 \neq 0$) from level three. As expected in this case, the population drops to zero after some time i.e the population undergoes damped oscillations and become completely lost after some time. Fig. 3.12 coupled with (3.66) suggests that the imaginary part of the eigenvalues corresponds to loss as in this case only γ_2 is nonzero i.e loss is only from level two. Such behaviour is seen in hermitian systems with phenomenologically added losses to only level two [41]. Comparing these two cases we can infer that the imaginary parts of the non-interacting hamiltonians($\Omega = \kappa = 0$) in the hamiltonian adds losses in the Bloch equations.

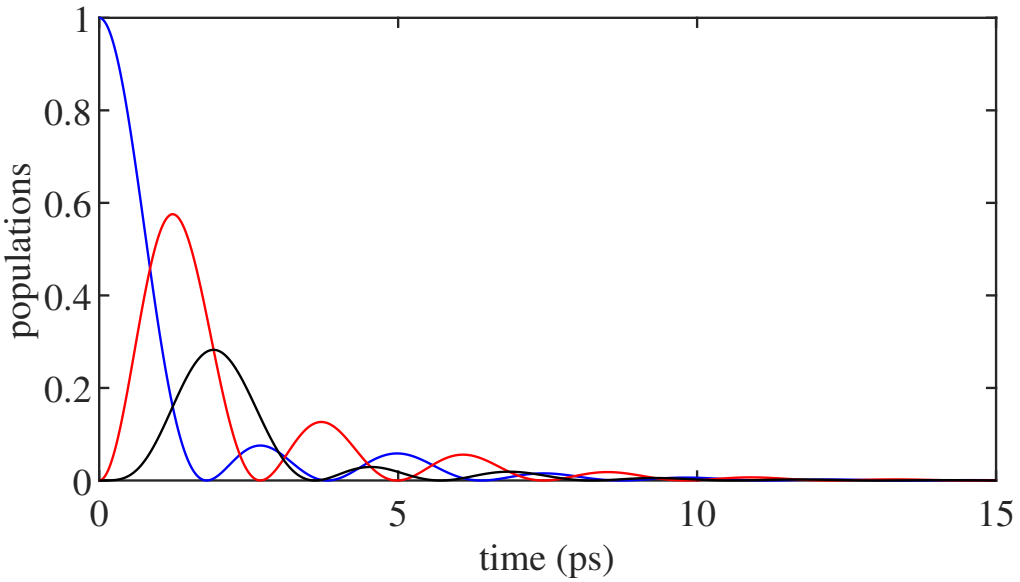

Figure 3.12: Simulation of three level Λ system with parameters - Ω=κ = 1 THz, Δ_1=Δ_2=0, γ_1 = 0 THz and γ_2 = 1 THz.

Fig. 3.13 shows coherent population trapping i.e. the population is in a superposition state of level zero and level two when there's loss from level one.

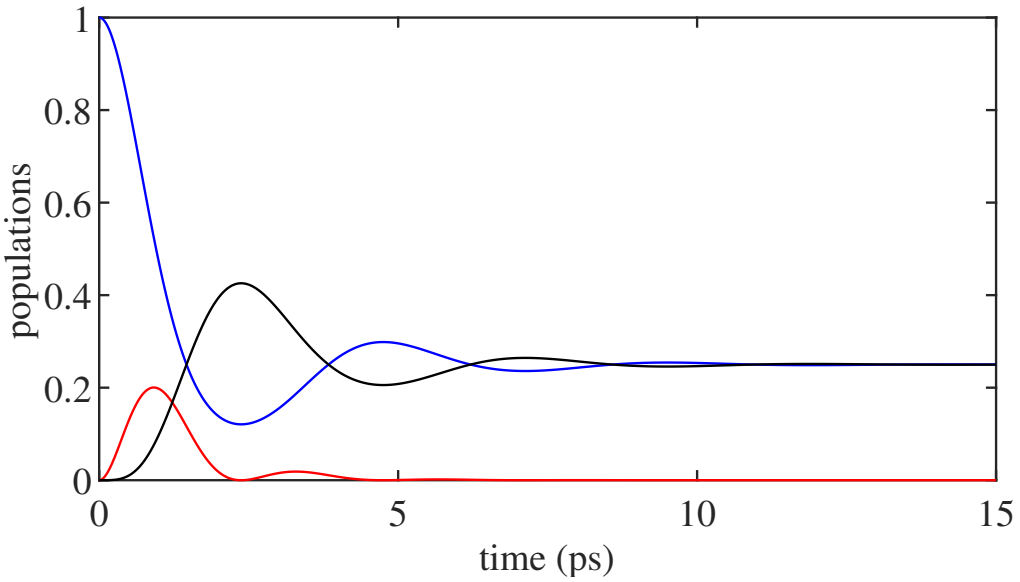

Figure 3.13: Simulation of three level lambda system with parameters - Ω=κ = 1, Δ_1=Δ_2=0 THz, γ_1 =1 and γ_2 = 0 THz. This corresponds to the case of coherent population trapping as the loss is from level one.

We have shown that using a three level non-hermitian system yields the same results as using a hermitian system with phenomenologically added losses in Bloch equations. The added advantage of the non-hermitian system is the easy calculation of lifetime of eigenstates i.e. metastable(eigenstates with finite lifetime) eigenstates and exact losses

from the hamiltonian. In the next chapter we solely focus on non-hermitian quantum mechanics in two and four level systems and discuss/investigate some important/and interesting properties of such hamiltonians. We have also derived the Bloch equations for non-hermtiian systems to show the equivalence with the hermitian systems with added losses in Bloch equations.

3.6 Conclusions

To conclude, we've shown that long pump and relatively short probe pulses are needed to observe EIT experimentally. We first noticed that the experimental results are inconclusive and then succeeded in explaining why no splitting could be observed in the experimental results. We then explored real systems with losses and showed some simulations of three level systems including coherent population trapping using non-hermitian quantum mechanics.

Chapter 4

Exceptional Points in few level Systems

4.1 Introduction

The third postulate of quantum mechanics supposes that every physical observable has a corresponding quantum mechanical operator. From here, the usual conclusion is that these QM operators should be hermitian thereby leading to real eigenvalues or observables. This applies naturally to closed quantum systems but not for open driven quantum systems which are ubiquitous in real life. Hermiticity of observables is a sufficient condition but not a necessary one for the observable value to be real. This leads to the study of non-hermitian systems. A more general condition is PT symmetry[42–44]. PT symmetric hamiltonians are non-hermitian but have real spectra. Beyond PT symmetry, the non-hermitian hamiltonian have complex spectra[45, 46] where the imaginary part of the eigenvalues define the lifetime of the states. Since open/lossy systems are ubiquitous in nature, non-hermitian systems have generated great interest recently. Starting from hermitian Hamiltonians, equations of motion for the observables (or the density matrix) can be derived and interactions with the environment can be included by phenomenologically adding decays to these rate equations. This approach ignores the details of feedback from the environment which limits the scope of standard quantum mechanics. Non-hermitian hamiltonians include the environment(continuum of scattering wavefunctions) and the embedded system interaction allowing the eigenvalues to be complex where the imaginary part generally relates to dissipation from system to environment. The finite lifetime of the states is thus calculated directly from the non-hermitian hamiltonian[47, 48] unlike

in (small)hermitian systems where it is calculated via a tunnelling process which ignores the environment feedback. Non-hermitian Hamiltonians can describe these metastable states quite efficiently[45, 46]. This leads to the study of open quantum systems with non-hermitian Hamiltonians where the feedback/damping from the environment is explicitly included in the Hamiltonian[49].

Some counterintuitive results that show the limitations of standard quantum theory approaches include phase-lapses in mesoscopic systems [50–52] where quantum phase transitions are experimentally observed in the transmission process in Aharonov-Bohm rings containing a quantum dot. This phenomenon can only be explained by considering from the start a non-hermitian Hamiltonian[53] which showed that this is related to the phenomenon of resonance trapping which can be explained by considering the feedback from the environment. Another counterintuitive example is dynamical phase transition(DPT). Dynamical phase transitions in many body open quantum systems results in a spectroscopic redistribution which leads to the robust existence of short lived states with long lived ones (width bifurcation)[54] and is similar to Dicke superradiance in optics[55]. Dynamical phase transition in many body systems can happen via width bifurcation while in a two level system via strong coupling to the environment[54]. This spectroscopic redistribution is related to the violation of Fermi's rule. DPT is observed experimentally and theoretically in spin swapping operation[56]. Fermi's golden rule is violated above the DPT[57] and is replaced by an anti-golden rule[54].

We now outline a few key properties of non-hermitian quantum mechanics which we shall use in this chapter. For a thorough introduction to non-hermitian quantum mechanics, see Refs [49, 58]. Unlike hermitian systems where the eigenstates are orthogonal to each other, in non-hermitian systems the states are bi-orthogonal i.e. the eigenvectors of hamiltonian and its adjoint form a bi-orthogonal basis.

4.1.1 Properties of non-hermitian systems

Consider a symmetric open quantum system -

$$H = H_h - i\Gamma_h, \tag{4.1}$$

$$H^\dagger = H_h^\dagger + i\Gamma_h^\dagger. \tag{4.2}$$

where, $H_h = H_h^\dagger$ and $\Gamma_h = \Gamma_h^\dagger$ are hermitian. The left and right eigen-equations for this hamiltonian (H) are -

$$H|\phi_n\rangle = \kappa_n|\phi_n\rangle, \tag{4.3}$$
$$\langle\phi_n|H^\dagger = \tilde{\kappa}_n\langle\phi_n|. \tag{4.4}$$

We will now calculate the inner product of left and right eigenvectors of H i.e. $\langle\phi_m|\phi_n\rangle$.

$$H|\phi_n\rangle = \kappa_n|\phi_n\rangle, \tag{4.5}$$
$$\langle\phi_m|H^\dagger = \tilde{\kappa}_m\langle\phi_m|. \tag{4.6}$$

Multiplying (4.5) with $\langle\phi_m|$ and (4.6) with $|\phi_n\rangle$ we get,

$$\langle\phi_m|H|\phi_n\rangle = \kappa_n\langle\phi_m|\phi_n\rangle, \tag{4.7}$$
$$\langle\phi_m|H^\dagger|\phi_n\rangle = \tilde{\kappa}_m\langle\phi_m|\phi_n\rangle, \tag{4.8}$$
$$\implies \langle\phi_m|H - H^\dagger|\phi_n\rangle = (\kappa_n - \tilde{\kappa}_m)\langle\phi_m|\phi_n\rangle, \tag{4.9}$$
$$\implies \langle\phi_m|\phi_n\rangle = 2i\frac{\langle\phi_m|\Gamma_h|\phi_n\rangle}{\tilde{\kappa}_m - \kappa_n}. \tag{4.10}$$

Similarly the eigen-equation for $H^\dagger$ is -

$$H^\dagger|\chi_n\rangle = \nu_m|\chi_n\rangle, \tag{4.11}$$
$$\langle\chi_n|H = \tilde{\nu}_m\langle\chi_n|. \tag{4.12}$$

and the inner product $\langle\chi_m|\chi_n\rangle$ is

$$\langle\chi_m|\chi_n\rangle = 2i\frac{\langle\chi_m|\Gamma_h|\chi_n\rangle}{\tilde{\nu}_n - \tilde{\nu}_m}. \tag{4.13}$$

These equations show that the eigenstates of the non-hermitian systems are not identically orthogonal i.e. not all the states are orthogonal to each other. This implies that the general superposition and projection techniques in standard quantum mechanics cannot be applied here. Therefore, we need a new formalism for non-hermitian systems. It can be shown that the eigenstates of H_h are linearly independent of each other and form a complete basis. We will now calculate the inner product between eigenvectors of H_h and $H_h^\dagger$.

Multiplying (4.12) with with $|\phi_m\rangle$ from the right and using the eigen-equations (4.12) and (4.5) results in two expressions for the same product calculation -

$$\langle\chi_n|H|\phi_m\rangle = \tilde{v}_n\langle\chi_n|\phi_m = \kappa_m\langle\chi_n|\phi_m\rangle, \tag{4.14}$$

$$(\tilde{v}_n - \kappa_m)\langle\chi_n|\phi_m\rangle = 0. \tag{4.15}$$

This condition implies that either $(\tilde{v}_n - \kappa_m) = 0$ or $\langle\chi_n|\phi_m\rangle = 0$. It is not possible for $\langle\chi_n|\phi_m\rangle$ to be identically zero, because that would mean that for all values of m, ϕ_m states are not orthogonal to each other but orthogonal to χ_n where n is fixed. This is not possible as both H and $H^\dagger$ have the same basis dimension. This means that at least for one pair of $(n.m)$ this expression is non-zero. Assuming that the states are non-degenerate results in only one state in $K^\dagger$ being orthogonal to one state in H i.e.

$$\langle\chi_n|\phi_m\rangle = \delta_{mn}\langle\chi_n|\phi_n\rangle. \tag{4.16}$$

This is known as bi-orthogonality where the states of an operator and its adjoint are orthogonal. Orthogonality in hermitian systems can be seen as a special case of bi-orthogonality as in the case $H^\dagger = H$.

Degeneracy in non-hermitian Hamiltonians is different than hermitian degeneracy. Here, the eigenvectors as well as the eigenvalues coalesce at the degeneracy. These points in parameter space are called exceptional points after the pioneering work of Kato[59]. The Hamiltonian at these non-hermitian degeneracies is non-diagonalisable and the matrix is known as defective in mathematics. At these points, associated eigenvectors appear due to Jordan chain relations. The associated eigenvectors are explained later. The geometric phase at exceptional points differs from the Berry phase at diabolic points by a factor of 2. Exceptional points are numerically studied in atoms[60], quantum dots[61], molecular networks[62] and metamaterials[63, 64] etc.

Previously these exceptional points were thought of as merely mathematical constructs and known as branch points in the complex plane of a double pole of the S matrix. It has been shown that in addition to the first order pole due to resonances, a second order pole emerges in the Green's function due to the coalescence of eigenstates which leads to patterns resembling Fano-Feshbach resonances[65]. For specific parameter values systems containing exceptional points exhibit interesting physics including divergent Petermann factor[66, 67], loss-induced revival of lasing[68], single mode-lasers[69, 70],

dark-state lasers[71], coherent absorption[72], stopping light in systems prepared at exceptional points[73] and unidirectional light propagation[74–76]. In an open quantum system embedded in the continuum of scattering wave-functions it is possible for the states to couple via the environment thus causing the external mixing of states. The observable effects of external mixing and the non-hermitian degeneracies on the resonance structure has been explored in two and three level systems coupled with the existence of nonlinear terms in the Schrödinger's equation term for general non-hermitian dynamics[77]. It has also been shown that while the exceptional points do not influence the dynamics of open quantum system in a one channel case it does have observable effects for two or more channel cases[77]. It is shown that in the vicinity of exceptional points the Schrödinger's equation contains nonlinear terms[49]. Moving away from the exceptional points gets rid of this nonlinearity. In reference [78], the analytical and numerical results of eigenfunctions/eigenvalues of a non-hermitian hamiltonian, phase rigidity, bi-orthogonality and the influence of exceptional points on physical observables is discussed.

The topological properties of exceptional points have been studied before [79]. It has been shown that by adiabatically encircling the exceptional point in parameter space the eigenvalues/eigenvectors can be permuted i.e the eigenvalues do not traverse in a closed curve in this case. This only happens when encircling the exceptional point. For a symmetric hamiltonian $H|\psi\rangle = \varepsilon|\psi\rangle$ and $\langle\psi^*|H = \varepsilon\langle\psi^*|$. Therefore the normalization is $\langle\psi^*|\psi\rangle$ which is a complex number. To facilitate a smooth transition from closed to open quantum systems the constraint is $\langle\psi_i^*|\psi_j\rangle = \delta_{ij}$. This implies $\mathrm{Im}(\langle\psi_i^*|\psi_j\rangle = 0)$. This condition implies that unlike hermitian quantum mechanics, here, the phase between two states is not rigid as this condition corresponds to a rotation. This also allows two wave functions to strongly interfere when the states are not orthogonal everywhere. This is one of the key differences in hermitian and non-hermitian physics. Far from the exceptional points the two eigenvectors are almost orthogonal just as for a hermitian system but at the exceptional point the two eigenvectors are not linearly independent. This is very important as it implies that as we approach the exceptional point, the phase (or angle) between the eigenvectors changes i.e the phase is not rigid. This differs from hermitian Hamiltonians where the eigenvectors are always orthogonal. This non-rigidity of the phase is quantitatively measured by the phase-rigidity[78] defined as

$$r_i = \frac{\langle\phi_i^*|\phi_i\rangle}{\langle\phi_i|\phi_i\rangle}, \quad 0 < r_i < 1, \tag{4.17}$$

and r_i measures the ratio of the c-product(which is defined to maintain orthogonality and closure properties of non-degenerate eigenvectors) and the inner product of a wavefunction. This ratio can be used to pinpoint the location of exceptional points in a system as it tends to zero as the system approaches the exceptional points. We can see that $r_i = 1$ for hermitian systems (since $\langle \phi_i^* | = \langle \phi_i |$). This phase rigidity definition is only applicable to symmetric systems. Later we have provided a general definition which is applicable to all cases and reduces the used definition in case of symmetric hamiltonians.

All of the studies described above make use of symmetric ($H = H^{\mathrm{T}}$) non-hermitian Hamiltonians. In this chapter we investigate an open 4-level system to propose an experiment to observe an exceptional point. Then we investigate a damped two-level system interacting with a circularly polarised light as described by an asymmetric non-hermitian Hamiltonian. This is a simple enough system to be studied analytically while complicated enough to exhibit a rich variety of behaviors. This system exhibits a ring of exceptional points in the parameter space of the real and imaginary dipole couplings where within the ring the energy eigenvalue of the system doesn't change. This leads to unstable regions inside the exceptional ring which is shown using a linear stability analysis. These unstable regions are unique to gain-loss systems and have the surprising property that no matter how small the gain/loss ratio, the gain always prevails at long times. We also report on eigenvalue switching, phase-rigidity and dynamics of the system around the exceptional points. We highlight that some of these properties are different than those in the widely studied case of symmetric non-hermitian Hamiltonians. In the next section we'll describe the properties of exceptional points in detail.

4.2 Properties of exceptional points

Mathematically speaking, exceptional points are the degeneracies of non-hermitian hamiltonians where not only the eigenvalues but also the eigenvectors coalesce. The effective hamiltonian has a singularity at these points but physically speaking these points are not distinguishable from neighbouring points by dramatic effects on observable quantities. Therefore, they are mostly known as true crossing points in relation to avoided level crossing phenomenon or branch points(level repulsion and width bifurcation) in physical literature. Coalescing eigenvectors doesn't imply a reduction in number of eigenvectors, instead an associated eigenvector appears due to Jordan chain relations at the singular

point.

Consider a general two level non-hermitian hamiltonian-

$$H = \begin{bmatrix} \omega_1 & \Omega_1 \\ \Omega_2 & \omega_2 \end{bmatrix}, \tag{4.18}$$

where $\omega_{1,2}$ are the energy levels of the closed system and $\Omega_{1,2}$ are the coupling strengths. All the terms are allowed to be complex. The eigenvalues of this hamiltonian are complex -

$$\lambda_{1,2} = \frac{\omega_1 + \omega_2}{2} \pm \frac{\sqrt{(\omega_2 - \omega_1)^2 + 4\Omega_1\Omega_2}}{2}, \tag{4.19}$$

and the corresponding eigenvectors are -

$$v_{1,2} = \begin{bmatrix} \frac{\omega_1 - \omega_2 \pm \sqrt{(\omega_2 - \omega_1)^2 + 4\Omega_1\Omega_2}}{2\Omega_2} \\ 1 \end{bmatrix}. \tag{4.20}$$

. There are some special cases that occur frequently in real systems -

1. If the term in the square root of (4.19) is real and positive then increasing the magnitude of coupling causes the real part of the eigenvalues to bifurcate i.e. level repulsion.

2. If the term in the square root of (4.19) is real and negative then the imaginary part of the eigenvalues bifurcates and the real part does not change. This is known as width bifurcation and changes the lifetime of the states.

3. If the term in the square root of (4.19) is zero then this is an exceptional point i.e non-hermitian degeneracy. At this point both the eigenvalues and the eigenvectors coalesce.

The condition for exceptional point is thus -

$$\begin{aligned} (\omega_2 - \omega_1)^2 &= -4\Omega_1\Omega_2, \\ \omega_2 - \omega_1 &= \pm 2i\sqrt{\Omega_1\Omega_2}. \end{aligned} \tag{4.21}$$

This is not possible with a hermitian system which has $\omega_{1,2}$ real and $\Omega_1^* = \Omega_2$. The later condition implies that $\Omega_1\Omega_2$ is always positive therefore right hand side of (4.22) is imaginary while the left hand side is real. Thus a hermitian system cannot satisfy the

exceptional point condition.

From Eqs. 4.19, 4.20 and 4.22 we see that at exceptional points, the eigenvalues and eigenvectors are identical for both states i.e. even the eigenvectors have coalesced. If $\Omega_1 = \Omega_2$ i.e. if the hamiltonian is symmetric, then the eigenvectors are independent of any parameters -

$$\begin{bmatrix} \pm i \\ 1 \end{bmatrix}. \tag{4.22}$$

Since the only requirement that we set for this calculation was that the hamiltonian must be symmetric, this result is invariant to all orthogonal transformation or any transformation that preserves the symmetry of the hamiltonian i.e. this result is true irrespective of the basis. Note that there is no orthogonal transformation between $\begin{bmatrix} i \\ 1 \end{bmatrix}$ and $\begin{bmatrix} -i \\ 1 \end{bmatrix}$. So at the exceptional point the eigenvector is either $\begin{bmatrix} i \\ 1 \end{bmatrix}$ or $\begin{bmatrix} -i \\ 1 \end{bmatrix}$. This introduces a chirality(handedness) in the system that can be observed experimentally[80].

Assuming that the hamiltonian is in the $\begin{bmatrix} i \\ 1 \end{bmatrix}$ state the left eigenvector corresponding to this state is $\begin{bmatrix} i & 1 \end{bmatrix}$. Notice that the norm between these states vanishes. This is often referred to as self-orthogonality. It is this vanishing of the norm that reduces a high dimensional system to fewer dimensions in the vicinity of EP.

One of the main differences in hermitian and non-hermitian quantum mechanics is that the phases between the states does not remain constant in the latter. It changes dramatically when approaching an exceptional point.

$$\frac{d|\phi\rangle}{dt} = \frac{-i}{\hbar} H|\phi\rangle, \tag{4.23}$$

$$\frac{d\langle\psi|}{dt} = \frac{i}{\hbar} H^\dagger \langle\psi|. \tag{4.24}$$

$$\tag{4.25}$$

Therefore,

$$\frac{d\langle\psi|\phi\rangle}{dt} = \frac{-i}{\hbar} \langle\psi|H - H^\dagger|\phi\rangle. \tag{4.26}$$

We can see that for a hermitian system this rate of change of phase between two states is zero while for a non-hermitian system it is non-zero thus proving that the phase between the states doesn't remain constant in a non-hermitian system and it varies with the inner

product of the non-hermitian part of the hamiltonian. This phase change is quantified by phase rigidity as defined in (4.17). It has been shown that the Schrödinger's equation contains nonlinear terms when the phase rigidity is less than one i.e. near exceptional points[48]. Exceptional points also exhibit topological properties which results in swapping of eigenvalues when encircling the exceptional point in parameter space. If the parameters are varied in such a way so as to traverse a closed loop in the parameter space then the eigenvalues also form a closed loop in general but this doesn't happen when an exceptional point is encircled. This can be illustrated by considering a two level hamiltonian -

$$H = \begin{bmatrix} -1 & \Omega \\ \Omega & 1 \end{bmatrix}, \tag{4.27}$$

The eigenvalues are -

$$\lambda_{1,2} = \pm\sqrt{1+\Omega^2}, \tag{4.28}$$

The exceptional points of this system are at $\Omega = \pm i$ Now if Ω is adiabatically varied so as to encircle the exceptional point i.e. $\Omega = i + re^{i\theta}$ where, r is the radius of the circle and $\theta \in [0, 2\pi)$. Assuming that the radius is small enough $(r << 2)$ i.e taking the limit that $r/2 \to 0$

$$\begin{aligned}
\lambda_{1,2} &= \pm\sqrt{1+\Omega^2}, \\
&= \pm\sqrt{1+(i+re^{i\theta})^2}, \\
&= \pm\sqrt{1+(-1)+r^2e^{2i\theta}+2ire^{i\theta}}, \\
&= \pm\sqrt{r^2e^{2i\theta}+2ire^{i\theta}}, \\
&= \pm\sqrt{r}e^{\frac{i\theta}{2}}\sqrt{re^{i\theta}+2i}, \\
&\approx \pm\sqrt{2r}e^{\frac{i\theta}{2}}\sqrt{i}, \\
&\approx \pm\sqrt{2r}e^{\frac{i\theta}{2}}e^{\frac{i\theta}{4}}, \\
&\approx \pm\sqrt{2r}e^{\frac{i\theta}{2}+\frac{i\theta}{4}}.
\end{aligned} \tag{4.29}$$

Encircling means that θ changes by 2π. This leads to switching of the eigenvalues as can be seen from (4.29). We see that for the eigenvalues to return to the original state θ has to change by 4π. Similarly eigenvectors also permute when encircling the exceptional points but for eigenvectors the encircling has to be done 4 times to return to the original

state due to a geometric phase acquired by the state during each loop[81, 82].

$$[\psi_1, \psi_2] \xrightarrow{\text{loop}} [\psi_2, -\psi_1] \xrightarrow{\text{loop}} [-\psi_1, -\psi_2] \xrightarrow{\text{loop}} [-\psi_2, \psi_1] \xrightarrow{\text{loop}} [\psi_1, \psi_2] \tag{4.30}$$

Quasi-statically demonstrating this 'flip' property in the instantaneous eigenbasis i.e. a system that starts with one eigenstate ends in the other eigenstate after a loop around the EP is possible. This means repeating the same experiment with slightly different parameter value (constant for each experiment but varying between the experiments) till it completes a loop around the exceptional point and measuring the eigenvalues at each independent experiment. This when plotted with against the varying parameter values will demonstrate the "flip" property. On the other hand, dynamically(performing single experiment with parameters varying with time) demonstrating this property is not possible. This is because adiabatically looping around the exceptional point is not possible as non-adiabatic effects are not negligible in this case. Due to the non-zero non-adiabatic effects the system is unable to perform adiabatic flip for both the initial eigenstates. Only one of the eigenstates behaves adiabatically while others do not. This leads to a chiral topological effect i.e whatever the initial state is, when we encircle an EP we always end up in the same state depending on whether we're going clockwise or anti-clockwise irrespective of the initial state [83]. At the EP the hamiltonian considered there is -

$$H = \begin{bmatrix} -1 & i \\ i & 1 \end{bmatrix}. \tag{4.31}$$

The eigenvalues of this hamiltonians are 0 and the eigenvectors are $\begin{bmatrix} i \\ 1 \end{bmatrix}$ i.e it is at the exceptional point. The way to dynamically loop around this exceptional point is to vary the coupling(off-diagonal terms) and the diagonal terms in a loop. Therefore, the hamiltonian will become -

$$H = \begin{bmatrix} -1 + r_1 \sin(\frac{2\pi t}{T} + \pi) & i + r_1 \cos(\frac{2\pi t}{T} + \pi) \\ i + r_1 \cos(\frac{2\pi t}{T} + \pi) & 1 - r_1 \sin(\frac{2\pi t}{T} + \pi) \end{bmatrix}, \tag{4.32}$$

where varying t from 0 to T will complete the loop. Using this hamiltonian and the Bloch equations, the populations for these states is calculated. Since we are interested in the population of the instantaneous eigenstates, these populations were projected onto that basis and the logarithm of the population with respect to variation in time was plotted.

We show this behaviour in a four level system in the next section.

Another interesting property of exceptional points is the effect of a small perturbation on the states. Since the hamiltonian is non-diagonalisable at the exceptional point we can write it in the normal Jordan form -

$$H_{nh} = \begin{bmatrix} E_0 & A_0 \\ 0 & E_0 \end{bmatrix}. \tag{4.33}$$

The perturbation matrix is described by -

$$H_1 = \begin{bmatrix} E_1 & A_1 \\ B_1 & E_1 + \Delta E_1 \end{bmatrix}. \tag{4.34}$$

The perturbed hamiltonian is then - $H = H_{nh} + \varepsilon H_1$, where ε is the perturbation strength. The energy level splitting in this case is -

$$\Delta E_{nh} = \sqrt{\varepsilon\sqrt{\varepsilon}(\Delta E_1)^2 + 4A_0B_1 + 4\varepsilon A_1B_1}. \tag{4.35}$$

For a degenerate hermitian system -

$$H_h = \begin{bmatrix} E_0 & 0 \\ 0 & E_0 \end{bmatrix}. \tag{4.36}$$

The energy splitting with the same perturbation as above is -

$$\Delta E_h = \varepsilon\sqrt{(\Delta E_1)^2 + 4A_1B_1}. \tag{4.37}$$

We see that the energy splitting of of non-hermitian system at exceptional point ((4.35)) is proportional to the square root of perturbation strength provided $B_1 \neq 0$. For hermitian systems the energy splitting is proportional to ε ((4.37)). Therefore we get larger splitting for small perturbations at exceptional points. This means for small enough perturbations the energy splitting is larger than a general hermitian system. This has potential for enhanced sensitivity based applications as discussed in[84–86]. For an n^{th} level system the splitting is proportional to the n^{th}-root. A recent paper shows that even though we get larger splitting at the exceptional point it doesn't translate directly to enhanced precision of sensors i.e complex energy splitting at EP is not a good estimate of precision

of exceptional point sensors [87]

Next we discuss two non-hermitian systems that we explored in detail. We'll start with a 4-level system to demonstrate some of the properties of exceptional points and investigate signatures of exceptional points in the absorption spectrum. After this section we present our findings on two-level asymmetric non-hermitian system i.e lossy two level system interacting with circularly polarised light.

4.3 4-level non-hermitian system

We have chosen a doubly degenerate 4-level system to explore the properties and signature of exceptional points that can be verified experimentally. There are several reasons to choose this system -

1. Most of the literature on EP is focussed on two-level systems due to the ability to calculate analytical results in simpler cases, therefore, we focussed on a higher level system to understand the effect of EP on such systems and potentially find higher level EPs where more than two eigenstates might coalesce. Another motivation was to observe the behaviour of the neighbouring states of the two states involved in the exceptional points.

2. Our aim is to study a real system rather than a toy problem so that the theory could be falsified. This system was chosen after discussing with our collaborators at University of Surrey and can be experimentally realised in optics using appropriate parameters.

3. This particular 4-level system has simpler analytical expressions for eigenvalues compared to other 3-level systems we thought of. It is also flexible enough to be turned into a two level system with appropriate parameters.

In this section. we mention key results in the investigation of exceptional points in a 4-level system. Fig. 4.1 shows the physical system.

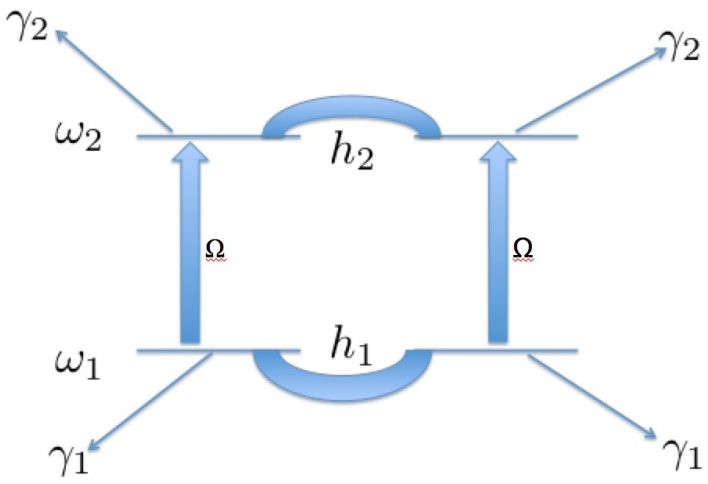

Figure 4.1: Level scheme and couplings in our system

The Hamiltonian of our four level system is :

$$\frac{\mathscr{H}}{\hbar} = \begin{bmatrix} \omega_1 - i\gamma_1 & h_1 & \Omega & 0 \\ h_1 & \omega_1 - i\gamma_1 & 0 & \Omega \\ \Omega & 0 & \omega_2 - i\gamma_2 & h_2 \\ 0 & \Omega & h_2 & \omega_2 - i\gamma_2 \end{bmatrix}$$

where $\omega_{1,2}$ are the energy levels, $\gamma_{1,2}$ are the lifetime of the eigenstates in the absence of any couplings, h_2, h_1 and Ω are the coherent hopping and dipole couplings as shown in Fig. 4.1. The dipole coupling Ω corresponds to the continuous wave field and is chosen to be on-resonance with the uncoupled two-level transitions.

There are seven energy(frequency)/time scales in this problem -

1. ground state and excited state frequencies - ω_1, ω_2
2. hopping strength between ground states and between excited states - h_1, h_2
3. ground and excited state lifetime - γ_1, γ_2
4. Rabi frequency - Ω

Clearly, we could set $\omega_1 = 0$ and then scale all the parameters by any one of the others without losing generality leaving us with five parameters. We choose, for now, to retain all seven, to keep clear the relationship with the physics. As we shall see below only certain energy differences turn out to be important. If we derive the Bloch equations from this Hamiltonian we obtain population and polarisation equations which have identifiable

decays related to the hopping and damping in a form identical to that we would find if we introduced them phenomenologically, after deriving the coherent terms in the Bloch equations.

4.3.1 Theoretical analysis

In this section we explore the nature of the exceptional points in the system. The eigenvalues of the above Hamiltonian are :

$$\lambda_{1,2} = \frac{\omega_1+\omega_2-h_1-h_2}{2} - i\frac{\gamma_1+\gamma_2}{2} \pm \frac{\sqrt{[\omega_2-\omega_1-h_2+h_1-i(\gamma_2-\gamma_1)]^2+4\Omega^2}}{2},$$

$$\lambda_{3,4} = \frac{\omega_1+\omega_2+h_1+h_2}{2} - i\frac{\gamma_1+\gamma_2}{2} \pm \frac{\sqrt{[\omega_2-\omega_1+h_2-h_1-i(\gamma_2-\gamma_1)]^2+4\Omega^2}}{2}.$$

Assuming that all parameters are real, the condition for four eigenvalues to coalesce in a 3^{rd} order exceptional point(4 state coalescing) is $h_1 = h_2 = 0$, $\omega_1 = \omega_2$ and $2\Omega = |\gamma_1 - \gamma_2|$. This implies a system of two identical but uncoupled two level systems and since $\omega_1 = \omega_2$ i.e. we need 4 degenerate levels. Therefore, this case is of little interest to us.

For $\omega_1 \neq \omega_2$, we only see the lowest order exceptional points for this hamiltonian i.e only 2 eigenstates coalesce. Again assuming that all parameters are real, the necessary condition for the existence of the exceptional point is when the expression under the square root is zero, i.e.

$$\omega_2 - \omega_1 - (h_2 - h_1) = 0, \tag{4.38}$$

$$2\Omega = |\gamma_1 - \gamma_2|, \tag{4.39}$$

for λ_1 and λ_2 to coalesce or

$$\omega_2 - \omega_1 + (h_2 - h_1) = 0, \tag{4.40}$$

$$2\Omega = |\gamma_1 - \gamma_2|, \tag{4.41}$$

for λ_3 and λ_4 to coalesce.

These conditions imply that in order to find an exceptional point $\omega_2 - \omega_1 = \pm(h_2 - h_1)$ or

physically the differential hopping strength matches the energy gap. We'll now focus our attention to $e_{1,2}$ eigenvalues to explore the concept of level repulsion and width bifurcation. Focussing on $\lambda_{1,2}$ we assume that $\omega_2 - \omega_1 - (h_2 - h_1) = 0$, then we obtain -

$$\lambda_{1,2} \;=\; \omega_1 - h_1 - i\frac{\gamma_1+\gamma_2}{2} \pm \frac{\sqrt{4\Omega^2-(\gamma_2-\gamma_1)^2}}{2},$$

- If $2\Omega > |\gamma_1 - \gamma_2|$,the term in the square root is positive and hence the square root is real. Then, increasing Ω or decreasing $|\gamma_1 - \gamma_2|$ means real part of λ_1 and λ_2 bifurcates while the imaginary part remains the same. This is known as level repulsion. Similar conditions for λ_3 and λ_4 can be derived.

- If $2\Omega < |\gamma_1 - \gamma_2|$, the term in the square root is negative and hence the square root is imaginary. Then decreasing Ω or increasing $|\gamma_1 - \gamma_2|$ means the imaginary part of λ_1 and λ_2 bifurcates while the real part remains the same. This is known as width bifurcation. This results in the appearance of a long lived states with a short lived one. Similar conditions for λ_3 and λ_4 can be derived.

- For a balanced gain-loss system $\gamma_1 = -\gamma_2$, If $2\Omega > |\gamma_1 - \gamma_2|$ then all the eigenvalues are real for all values of Ω. This means above a certain critical value of Ω, the system has completely real spectrum. This is an example of non-hermitian system with real spectrum thus proving that hermiticity is only a sufficient condition for real observables but not a necessary one.

We now look at how these eigenvalues coalesce as a function of the various parameters. For clarity we have chosen a set of parameter values so all the features appear clearly on the same pictures, we will present more realistic parameters in the next section. Figure 4.2 shows how the real and imaginary part of the eigenvalues behave as a function of coupling Ω(field strength), and we see that the two eigenvalues coalesce at the exceptional point for Ω=0.05.

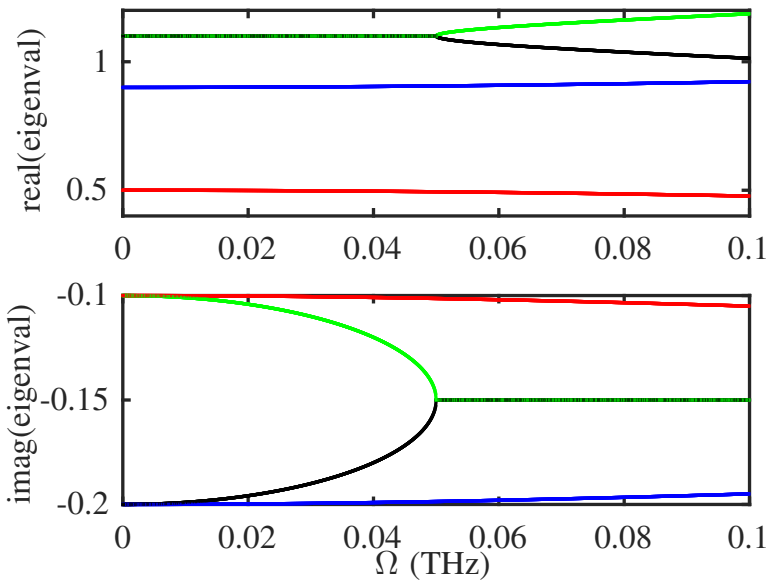

Figure 4.2: Real and imaginary part of the eigenvalues vs coupling strength(Ω). All the parameters are in THz units. The parameters are : $\omega_1 = 0.8, \omega_2 = 1, \gamma_1 = 0.1, \gamma_2 = 0.2, h_1 = 0.3, h_2 = 0.1$. The exceptional point is at Ω=0.05.

It is interesting to note the behaviour of the eigenvalues above and below the exceptional point. When Ω is small, the real part of the relevant eigenvalues are equal but the imaginary parts are different. Decreasing Ω, further bifurcates the imaginary part of the participating eigenvalues. This is known as width bifurcation. The lifetime of the participating states changes substantially near the exceptional point while the other neighbouring states do not show much sensitivity to the exceptional point. At the exceptional point the real as well as imaginary parts are equal. After the exceptional points as we increase the coupling strength Ω, the real part of the relevant eigenvalues bifurcates(level repulsion) but the imaginary parts remain the same. This behaviour can be used to identify the exceptional point in an experiment. In an ideal case, we expect to see a peak in the spectrum splitting in two peaks as Ω is increased and these two peaks will have same width after the exceptional point - we will discuss this in more detail below. We also note that the other pair of eigenvalues remains unaffected by the exceptional point.

Figure 4.3 shows how the eigenvalues change as a function of hopping coupling h_1. The exceptional points will appear when the energy difference $\omega_1 - \omega_2 = \pm(h_1 - h_2)$ or when $h_1 = \omega_1 - \omega_2 \pm h_2$ i.e. at $h_1 = -0.1, 0.3$ when $\omega_1 = 0.8, \omega_2 = 1$ and $h_2 = 0.1$. This means we see two exceptional points when varying h_1 compared to one exceptional point when varying Ω. When $h_1 = 0.3$, e_1 and e_2 coalesce while e_3, e_4 coalesces when $h_1 = -0.1$. Figure 4.3 confirms this calculation. Here also we notice a nonlinear change in the lifetime

of the participating states in the vicinity of the exceptional point.

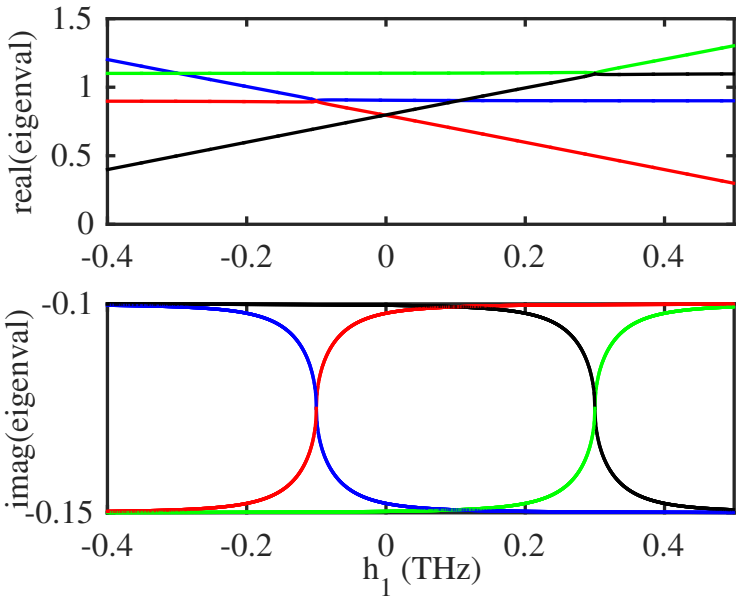

Figure 4.3: eigenvalues vs coupling strength(h_1). All the parameters are in THz units. The parameters are : $\omega_1 = 0.8, \omega_2 = 1, \gamma_1 = 0.1, \gamma_2 = 0.15, h_2 = 0.1, \Omega = 0.025$. We can see that 2 eigenvalues coalesce at h_1=0.3 and h_1=-0.1

4.3.2 Encircling EP and phase rigidity

In this section we investigate what happens when we dynamically encircle an exceptional point i.e we change the parameters with time in a loop around the exceptional point and track the populations of the four levels. As mentioned in the Introduction this encircling is different than quasi statically encircling the exceptional point in which case there is always a eigenstate flip involved with the encirclement. In this case, we're dynamically (parameters changing with time) going to encircle the exceptional point. In this case we always end in the same state(going clockwise) regardless of the initial conditions as mentioned in the Introduction. We always end up in the other eigenstate if going anticlockwise. The hamiltonian for encircling the exceptional point is -

$$H = \begin{bmatrix} \omega_1 - i\gamma_1 & h_1 + r_1 \sin 2\pi t/T & \Omega + r_2 \cos 2\pi t/T & 0 \\ h_1 + r_1 \sin 2\pi t/T & \omega_1 - i\gamma_1 & 0 & \Omega + r_2 \cos 2\pi t/T \\ \Omega + r_2 \cos 2\pi t/T & 0 & \omega_2 - i\gamma_2 & h_2 \\ 0 & \Omega + r_2 \cos 2\pi t/T & h_2 & \omega_2 - i\gamma_2 \end{bmatrix} \quad (4.42)$$

where $r_{1,2}$ are the radius of the loop. Fig. 4.4 shows the logarithm of population in all 4 states in the instantaneous eigenbasis with time when looping around the exceptional point for two different initial conditions. The exceptional point is at $\Omega = 0.005$THz We see that whatever initial condition we start with the population always ends up in the same state (level 3 in this case) if we loop around the exceptional point in same way (clockwise).

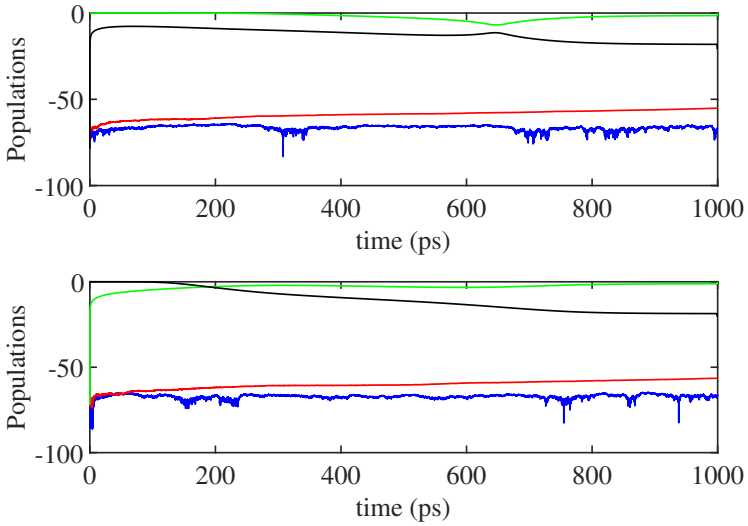

Figure 4.4: Logarithm of populations of states in instantaneous eigen-basis vs time for two different initial conditions. The parameters are $r_{1,2} = 0.001$THz, $\omega_1 = 10$THz, $\omega_2 = 0$THz,$h_1 = 5$THz, $\Omega = 0.005$THz, $h_2 = 15$THz, $\gamma_1 = 0.01$THz, $\gamma_2 = 0.02$THz and T=1000 ps. blue - level 1, red - level 2, green - level 3 and black - level4. Top figure : The initial condition is [0,0,1,0] i.e all the population resides in level 3. We see that at the end of the loop the maximum population still reside in level 3. Bottom Figure : The initial condition is [0,0,0,1] i.e all the population resides in level 4. We see that at the end of the loop the maximum population ends up in level 3.

After a long time though the population always ends up in the state with minimum loss i.e. state with lowest imaginary part of the eigenvalue. This can be seen in Fig. 4.5 where if we increase the encircling time around the EP by a factor of 10 we always end up in the level 2 state in the end.

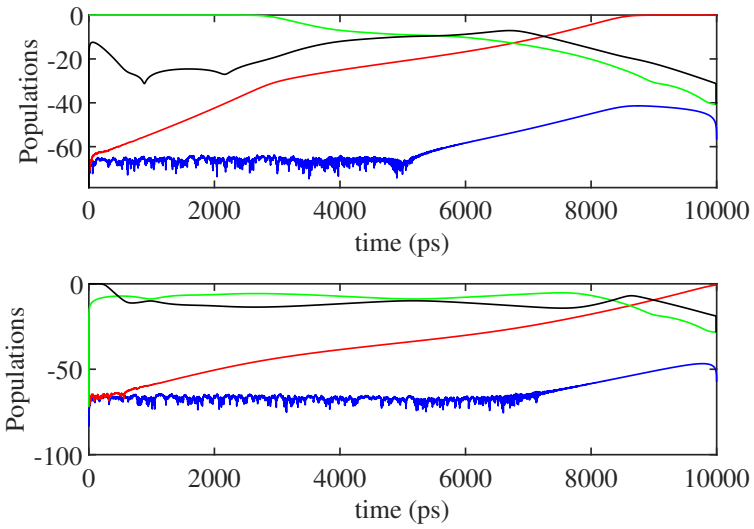

Figure 4.5: Logarithm of populations of states in instantaneous eigen-basis vs time for two different initial conditions. The parameters are $r_{1,2} = 0.001THz$, $\omega_1 = 10THz$, $\omega_2 = 0THz$,h_1=5 THz, $\Omega = 0.005THz$, h_2=15 THz, γ_1=0.01 THz, γ_2=0.02 THz and T=10000 ps. Blue - level 1, red - level 2, green - level 3 and black - level4. Top figure : The initial condition is [0,0,1,0] i.e all the population resides in level 3. We see that at the end of the loop the maximum population still reside in level 2. Bottom Figure : The initial condition is [0,0,0,1] i.e all the population resides in level 4. We see that at the end of the loop the maximum population ends up in level 2.

Fig. 4.4 and Fig. 4.5 show that there are three time intervals in play here. The first one is the initial time frame where population ratio doesn't swap between the states, the second one is the where the influence of exceptional point forces the population in one state only and the third one is where the final population resides in the longest-lived state of the system.

Fig. 4.6 shows the phase rigidity of all states with respect to the interaction term Ω. Notice that the exceptional point is at $\Omega = 0.005$THz and the phase rigidity of the involved eigen states reaches 0 at that point while the phase rigidity for the un-involved eigenstates remains at 1 at all times This can be used as a way to pinpoint the exceptional point location. We also notice that the phase rigidity tends to 1 between the two exceptional points as well as far from exceptional points.

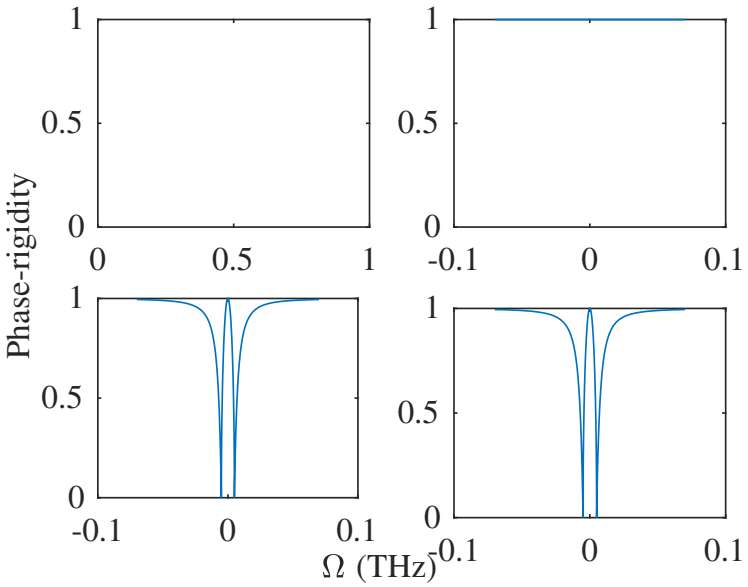

Figure 4.6: Phase rigidity as a function of Ω for all states. The phase rigidity of the state 1 (top left) and state 2 (top right) remains constant at one as expected because these states are not involved in the exceptional point. The exceptional point for states 3 (lower left)and 4 (lower right) exists at Ω = —0.005— THz as can be seen from the figure where the phase rigidity drops to 0 at these points.

In the next section we're going to investigate the signatures of exceptional points in the absorption spectrum and propose an experiment for the same.

4.3.3 Experiment

In this section, we suggest a method by which we can see the signature of the exceptional points in the spectrum. We continue as above to use parameters which allows the main features to be put on a single figure for clarity. Fig. 4.7 shows all the possible transition frequencies (differences in the real parts of the 4 eigenvalues) and how they change with changes in the coupling strength Ω. For h_1=h_2=Ω=0 i.e no applied field and no hopping couplings between degenerate levels, there is only one possible transition ω_2 - ω_1. For Ω=0 i.e zero applied field, the eigenvalues are :

$$\lambda_{1,2} = \omega_1 \pm h_1 - i\gamma_1, \tag{4.43}$$

$$\lambda_{3,4} = \omega_2 \pm h_2 - i\gamma_2. \tag{4.44}$$

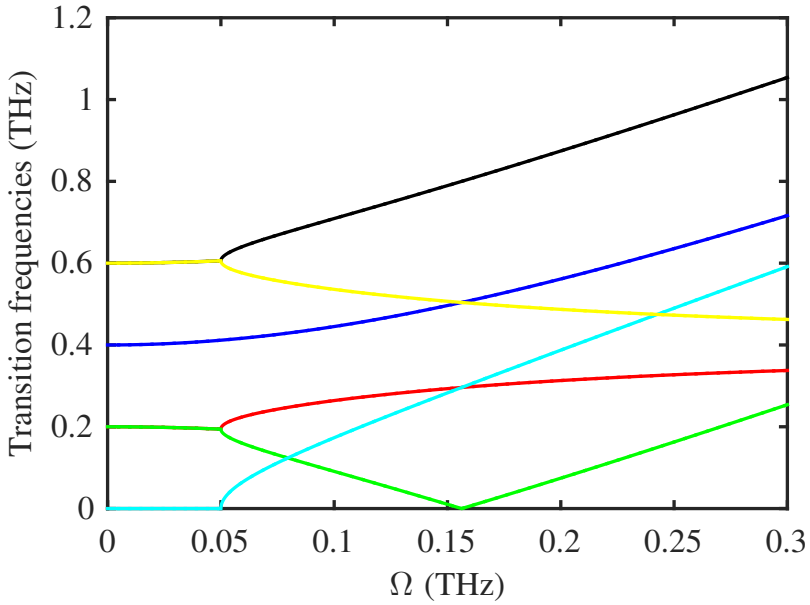

Figure 4.7: Transition frequencies (differences in the real part of the eigenvalues) vs coupling strength(Ω). All the parameters are in THz units. The parameters are : $\omega_1 = 0.8, \omega_2 = 1, \gamma_1 = 0.1, \gamma_2 = 0.2, h_1 = 0.3, h_2 = 0.1$.

Thus there are 6 possible transitions in general. In Fig. 4.7 we see only 4 distinct transitions at Ω=0. That's because for the parameters chosen i.e. $\omega_2 - \omega_1 = h_1 - h_2$ there are two degenerate transition pairs.

The bifurcation behaviour around Ω=0.05 (the exceptional point) is clear in the transition energies. For $\Omega < 0.05$ we have a four level system with two degenerate states so basically three peaks might be expected in the spectrum. Just after the point k=0.05 we have six different transition frequencies and we expect six peaks. This drastic change in the behaviour should be noticeable in the spectrum, assuming that the peaks are individually resolvable. We now address what might be seen for more realistic parameters.

4.3.4 Example with real parameters

We choose, ω_1=0 THz, ω_2=10 THz, $h_1 = 15$ THz, $h_2 = 5$ THz, $\gamma_1 = 0.01$ THz, $\gamma_2 = 0.02$ THz, which satisfies $\omega_2 - \omega_1 - (h_2 - h_1) = 0$, and the condition $2\Omega = |\gamma_1 - \gamma_2|$ will lead to an exceptional point at $\Omega = 0.005$THz.

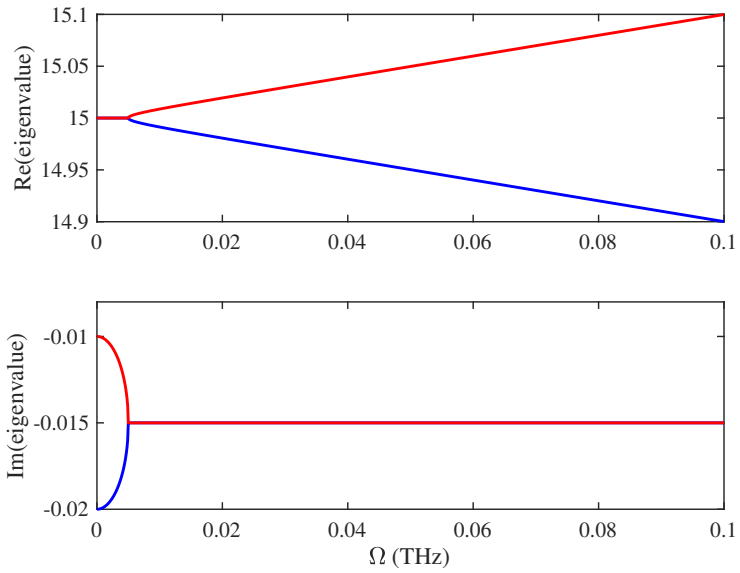

Figure 4.8: Real and imaginary parts of the eigenvalues vs coupling strength(Ω). Only the eigenvalues involved in the exceptional point are shown here.

Qualitatively, Fig. 4.8 shows the same behaviour as Fig. 4.2. Well beyond the exceptional point the magnitude of splitting for the real part of the eigenvalues is proportional to 2Ω as expected.

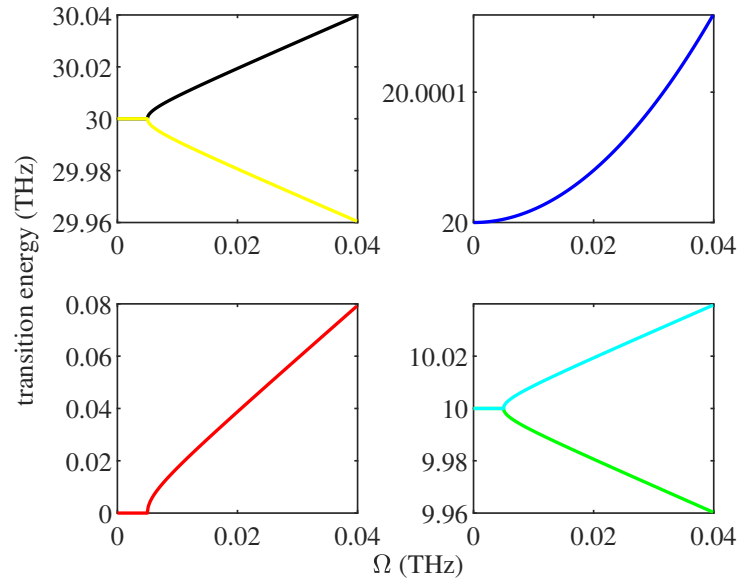

Figure 4.9: Transition frequencies corresponding to the above parameters. There are 4 panels corresponding to 4 different transition energy regions just so that the small splittings can be resolved.

Fig. 4.9 shows the transition frequencies as function of field strength (Ω) . As before the exceptional point is at $\Omega = 0.005$ THz.

The spectrum calculated for the parameters of Fig.4.9 is shown in Fig. 4.10. This is just a

proof of principle example to show that we can see the exceptional point in the spectrum. This is the general technique which might be useful in determining exceptional points experimentally. This spectrum is calculated by plotting the magnitude of the transition frequency with the field strength(Ω) and the position of the transition frequency. Each transition is treated as a lorentzian peaked at the real part of the transition frequency and the broadening corresponds to the imaginary part of the transition frequency. The magnitude of each transition is calculated using the relative magnitude of the lorentzian distribution i.e.

$$F \propto \frac{\mu\gamma}{(\omega-\omega_0)^2+\gamma^2}, \tag{4.45}$$

where, ω_0 is the real part of the eigenvalue, γ is the imaginary part, μ is the dipole strength and ω is the energy axis.

In this case(Fig.4.10) we have assumed the dipole strength to be 1 for all transitions thus overestimating the peak of each lorentzian at a particular parameter set. Accounting for the real dipole strength will let us get the correct spectrum where one or more transitions might be suppressed.

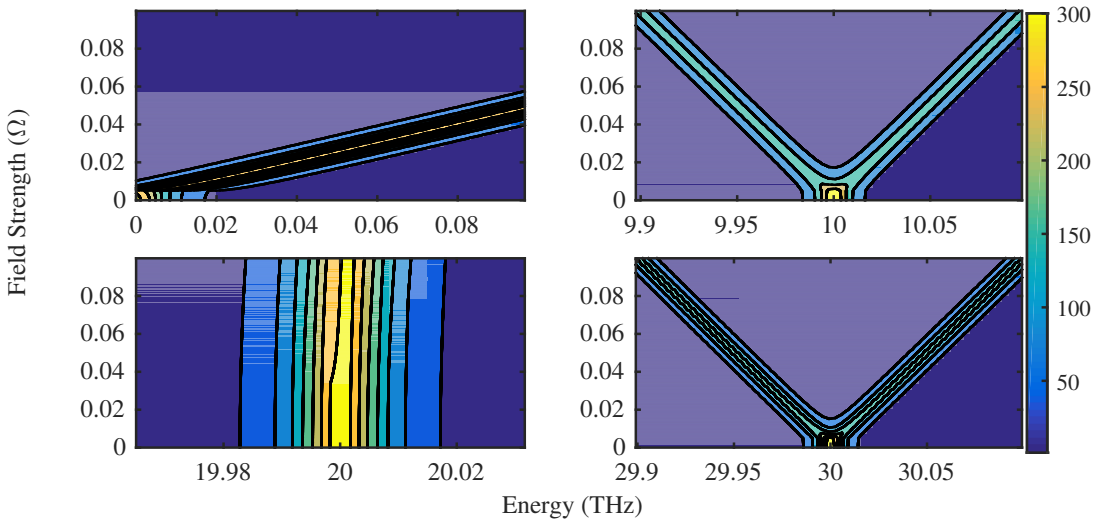

Figure 4.10: Proof of principle spectrum : magnitude and position of transition energy plotted as a function of coupling field strength. Each subplot shows a part of the spectrum where we expect a transition when dipole strength for every transition is set to 1. The parameters are as in Fig.4.9 i.e exceptional point at $\Omega = 0.005$

We now consider what one might expect if one tried to do an absorption measurement in this system using a weak probe of tuneable wavelength. This would be in addition to the c.w. amplitude field implied by Ω.

To calculate the expected absorption spectrum for this system we assume that before any probe light comes along the system will sit in the lowest state. Then the polarisations are calculated using Bloch equation simulations. The Fourier transforms of the polarisations return the correct spectrum for the given parameters. The magnitude of the transition is approximated as the peak value of the observed lorentzian while the transition frequency is the position of the peak value of the observed spectrum. Fig. 4.11 shows the correct spectrum for the parameters of Fig. 4.10.

Taking into account the dipole strength for each transition and looking into transitions from the ground state only we found out that only one transition is allowed rather than three transitions. Now the question is how can we use only one transition to find the exceptional point in the spectrum. Fortunately, in this case the transition that is allowed is the one that comes from the two states involved in the exceptional point, specifically the left splitting at the 30THz mark in Fig. 4.10. Now as we increase the field strength this transition frequency decreases i.e as field strength increases the splitting increases but since we're looking at the lower level of the two levels involved we see an inverse relation between field strength and this particular transition hence proving that it's the transition involved with the splitting. We can use this transition to determine the exceptional point because there'll be no change in the transition frequency before the exceptional point and then sudden change will appear just after the exceptional point as shown in the previous plots. This discrete change in the transition frequency will lead to a cusp kind of behaviour around the exceptional point rather than a smooth change in frequency. This point will become clear as we see the difference in Fig. 4.11 and Fig. 4.12. The change in the frequency is smooth in Fig. 4.12 thus indicating we're not at the exceptional point in contrast to the "sudden cusp kind of change" in Fig. 4.11.

Also peculiar is the spectrum away from the peak of the spectrum. We notice that in case of exceptional points(Fig. 4.11), the magnitude decreases with Ω till we reach the exceptional point and increases with Ω afterwards.

While in cases when we are away from the exceptional points we see a continuous increase in the magnitude. This behaviour can be explained by looking at the behaviour of eigenvalues before and after the exceptional point i.e the imaginary part changes before the EP and real part remains constant while the real part changes after the EP but the imaginary part remains constant. This implies that before the EP it's the imaginary part that determines the spectrum while the real part determines the spectrum after the EP. In

our case it turns out the imaginary part(<0) of the eigenvalues involved increases before the EP and therefore we see the decrease in magnitude of the spectrum before the EP as the magnitude is proportional to imaginary part. After the EP, the real part decreases and therefore we see an increase in the magnitude of the spectrum as it's inversely proportional to the square of the real part of the eigenvalues.

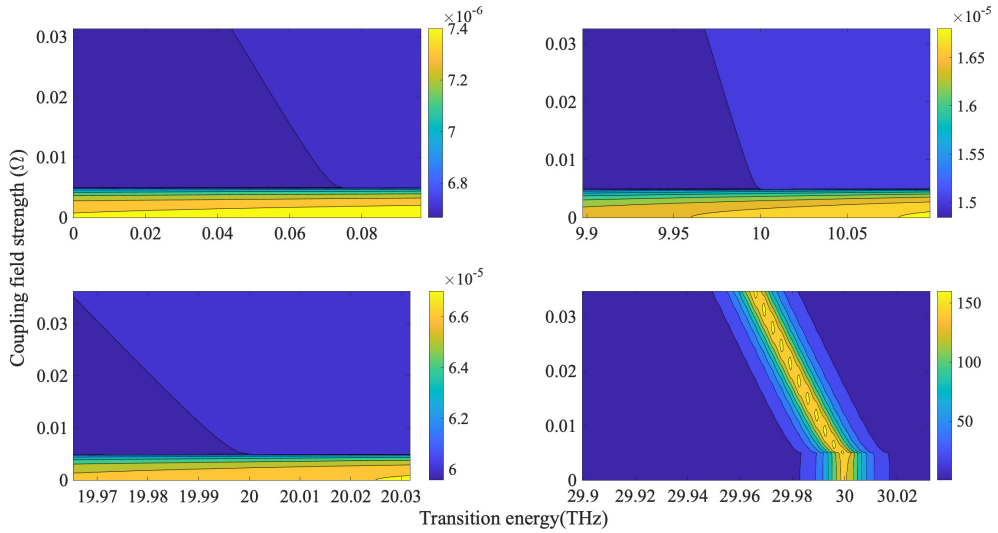

Figure 4.11: Spectrum as a function of field strength. Each subplot shows a part of the spectrum where we expect a transition when dipole strength for every transition is set to 1.The parameters are as in Fig.4.9 i.e exceptional point at $\Omega = 0.005$

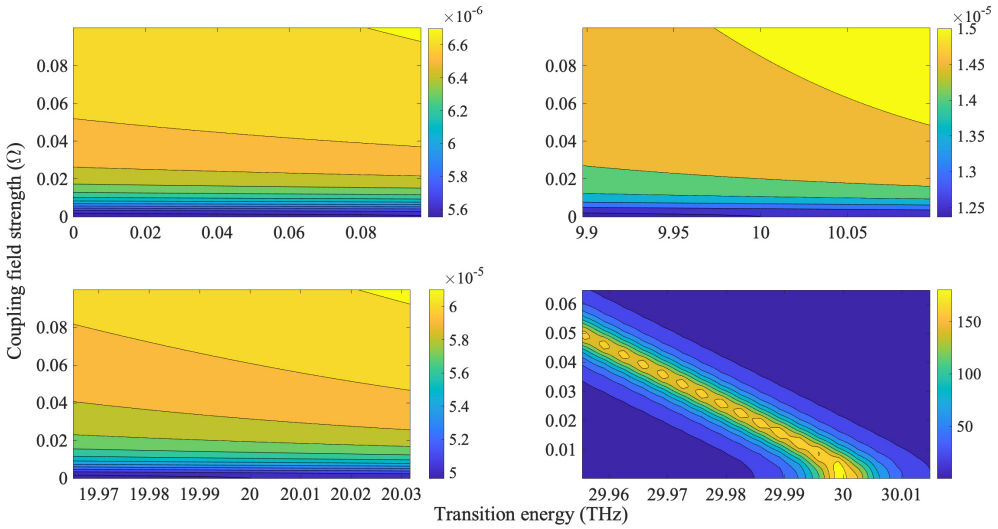

Figure 4.12: Spectrum as a function of field strength. Each subplot shows a part of the spectrum where we expect a transition when dipole strength for every transition is set to 1.The parameters are as in Fig.4.9 except $h_1 = 5.01$ therefore we're not at the exceptional point.

The magnitude involved here is very small compared to the peak of the spectrum but this serves as a strong signature of exceptional point. Comparing Fig.4.13 and Fig.4.11

tells that there's very negligible visible difference between the transition peaks at 30THz, but the behaviour away from the peak can be used to show that Fig.4.11 is the one that corresponds to the exceptional point (due to the magnitude being oscillatory in this case and continuously increasing in the other case.) Fig.4.14 shows the spectrum near the wings of the transition peak so as to ensure stronger measurable signal and also explains why this behaviour serves as a strong signal of the existence of the exceptional point. So this behaviour serves as an even stronger signature of exceptional point in our case.

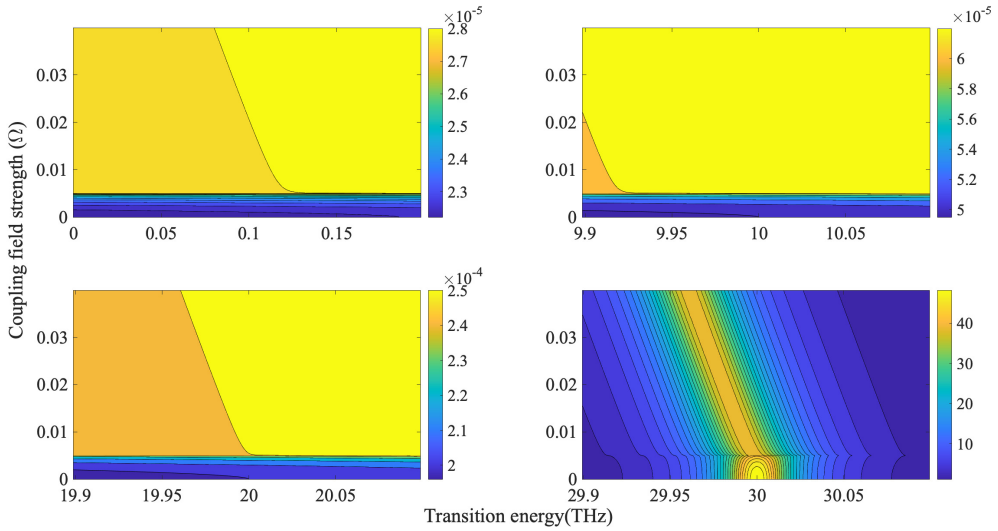

Figure 4.13: Spectrum as a function of field strength. Each subplot shows a part of the spectrum where we expect a transition when dipole strength for every transition is set to 1. The parameters are as in Fig.4.9 except $h_1 = 5.00001$ therefore we're not at the exceptional point.

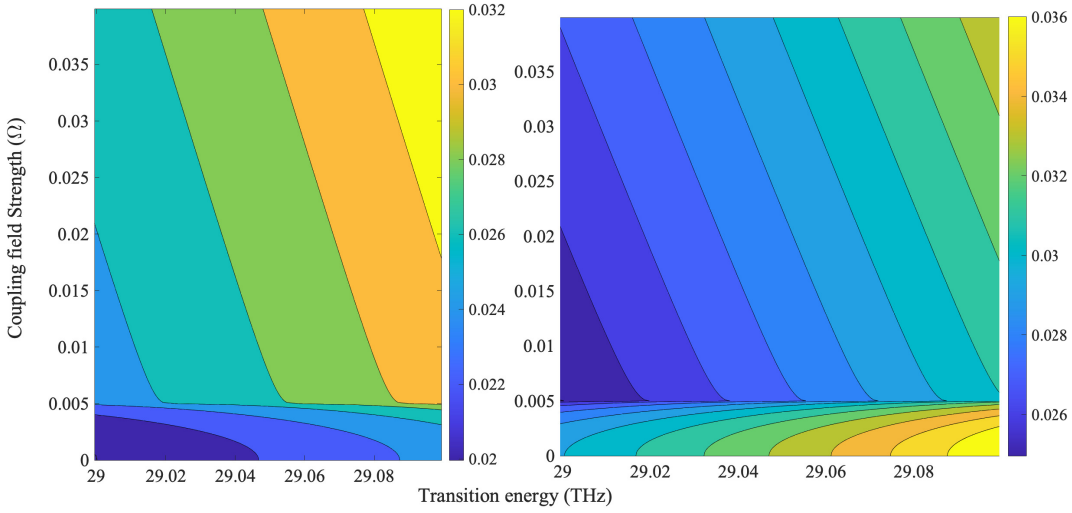

Figure 4.14: Spectrum as a function of field strength. The parameters are as in Fig.4.9 except a). $h_1 = 5.00001$ therefore not at the exceptional point b). $h_1 = 5$ therefore at the exceptional point.

Two different conditions when satisfied simultaneously leads to an exceptional point at $\omega_2 - \omega_1 = |h_1 - h_2|$. This implies that the transition frequency must be equal to the difference in the internal couplings. One way to ensure this is to add external couplingΔh_1 which we can control. Once we've achieved this condition then the other condition is quite simple to work with by changing the intensity to satisfy, $2\Omega = |\gamma_1 - \gamma_2|$. This implies we just need the field strength to be equal to the difference in the two decay processes - when the decay rate is quite small we can get the exceptional point at low intensities also as is shown in Fig. 4.8

4.3.5 Optical gain-loss

We can also do the same calculations for the case when $\gamma_2 = -\gamma_1$ i.e optical gain loss system. This will lead to higher order exceptional points and completely real eigenvalues depending on the parameter range. A 2^{nd} order exceptional point can be identified at $\omega_1 = \omega_2$, $h_1 = h_2$ and $2\Omega = |\gamma_1 - \gamma_2|$.
Physically, this will correspond to a linear chain of 4 particles with nearest neighbour coupling h_1 and next nearest neighbour coupling Ω as shown in Fig. 4.15.

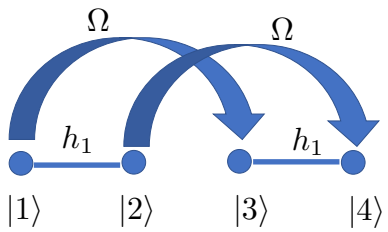

Figure 4.15: 4 level system with above-mentioned parameters.

We noticed that most of the systems studied in context of non-hermitian physics are symmetric so next we focussed on an asymmetric two-level optical system to investigate the differences between the two and explored exceptional rings (explained in next section) in a real optical system.

4.4 Exceptional points in a two level atom interacting with circularly polarised light

We investigated a damped two-level system interacting with a circularly polarised light as described by an asymmetric non-hermitian Hamiltonian. This is a simple enough system to be studied analytically while complicated enough to exhibit a rich variety of behaviors. This system exhibits a ring of exceptional points in the parameter space of the real and imaginary dipole couplings where within the ring the energy eigenvalue of the system doesn't change. This leads to unstable regions inside the exceptional ring which is shown using a linear stability analysis. These unstable regions are unique to gain-loss systems and have the surprising property that no matter how small the gain/loss ratio, the gain always prevails at long times. We also report on eigenvalue switching, phase-rigidity and dynamics of the system around the exceptional points. We highlight that some of these properties are different than those in the widely studied case of symmetric non-hermitian Hamiltonians. The coherent time evolution of a two level system under external perturbations can be described by the optical Bloch equations. There are many systems where the selection rules for excitation is $\Delta J_z = \pm 1$ and these transitions are driven by elliptically(or circularly) polarised light. We study a two level system interacting with a circularly polarised light which can be described in the rotating frame by the Hamiltonian[88],

$$H_h = \hbar \begin{bmatrix} 0 & \Omega_r - i\Omega_i \\ \Omega_r + i\Omega_i & \Delta \end{bmatrix}, \tag{4.46}$$

where Δ is the detuning frequency between the transition and laser energies and Ω_r, Ω_i are the real and imaginary parts of the dipole (Rabi) coupling. This Hamiltonian is self-adjoint, thus hermitian and therefore has real spectrum. Adding diagonal decay (or gain) to this Hamiltonian leads to a asymmetric non-hermitian Hamiltonian,

$$H_{nh} = \hbar \begin{bmatrix} -i\gamma_1 & \Omega_r - i\Omega_i \\ \Omega_r + i\Omega_i & \Delta - i\gamma_2 \end{bmatrix}, \tag{4.47}$$

where γ_1, γ_2 are the (positive or negative) interactions with the external bath as indicated in Fig. 4.16. The Bloch equations for this system can be derived as usual from the

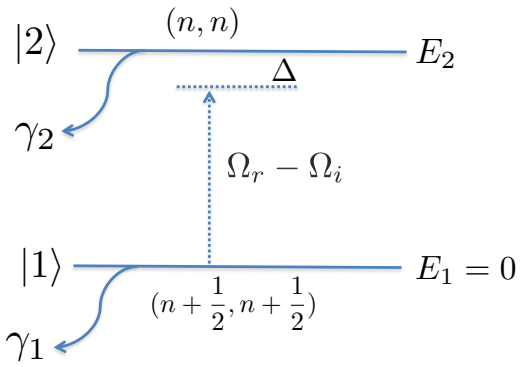

Figure 4.16: Schematic of a two level system interacting with left circularly polarised light $(\Omega_r - i\Omega_i)$. Decays out of the system are captured by $\gamma_{1,2}$.

quantum Liouville equation as,

$$\begin{bmatrix} \dot{n}_1 \\ \dot{n}_2 \\ \dot{P}_r \\ \dot{P}_i \end{bmatrix} = - \begin{bmatrix} 2\gamma_1 & 0 & 2\Omega_i & 2\Omega_r \\ 0 & 2\gamma_2 & -2\Omega_i & -2\Omega_r \\ -\Omega_i & \Omega_i & \gamma_1+\gamma_2 & \Delta \\ -\Omega_r & \Omega_r & -\Delta & \gamma_1+\gamma_2 \end{bmatrix} \begin{bmatrix} n_1 \\ n_2 \\ P_r \\ P_i \end{bmatrix}, \tag{4.48}$$

where $n_{1(2)}$ are the populations in the ground and excited states and $P_{r(i)}$ are the real and imaginary parts of the polarisation. The remaining terms are as defined in the Hamiltonian above. As expected population decays appear in the diagonal elements of the equations of motion, in the same way as if they had been introduced phenomenologically. In contrast to the optical Bloch equations with linearly polarised light, we see that, both the real and imaginary parts of the polarisation directly drive the populations.

We now explore the exceptional points and excitation dynamics of H_{nh} and make comparisons with related symmetric cases.

4.5 Exceptional ring and phase rigidity

The eigenvalues of H_{nh} are complex and given by

$$\begin{aligned} \varepsilon^{\pm} &= \frac{\Delta - i(\gamma_1+\gamma_2)}{2} \\ &\quad \pm \frac{\sqrt{(\Delta - i(\gamma_2-\gamma_1))^2 + 4(\Omega_r^2+\Omega_i^2)}}{2}. \end{aligned} \tag{4.49}$$

Exceptional points arise for parameters for which the term under the square root goes to zero i.e

$$\Delta = 0 \qquad \text{and} \qquad \Omega_r^2 + \Omega_i^2 = \frac{(\gamma_2 - \gamma_1)^2}{4}. \tag{4.50}$$

These conditions correspond to on-resonance excitation and a matching of the optical Rabi coupling (Ω) and the differential gain/loss rate from the two levels. For these parameter values, the two eigenvectors collapse into each other and the matrix is non-diagonalisable having only one eigenvector. For a fixed γ_1 and γ_2 (4.50) describes a circle in the (Ω_r, Ω_i) parameter space of radius $|\gamma_2 - \gamma_1|/2$, also known as an exceptional ring.

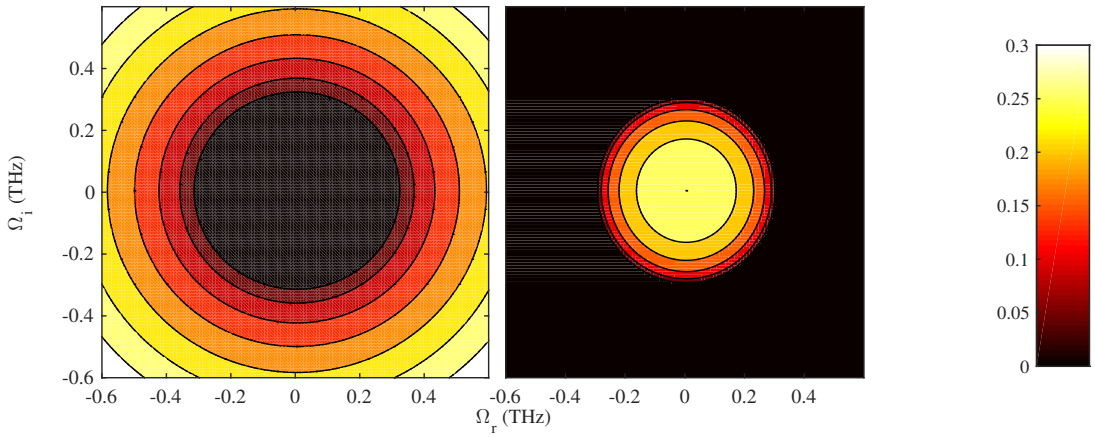

Figure 4.17: Real (left panel) and imaginary (right panel) part of one of the eigenvalues of H_{nh} plotted in (Ω_r, Ω_i) parameter space with Δ=0 THz and $\gamma_1 = 0.3$ THz and $\gamma_2 = -0.3$ THz . We can clearly see the exceptional ring at $|\Omega| = (\gamma_2 - \gamma_1)/2$.

Fig. 4.17 shows that inside the ring the real part of the eigenvalues is zero but the imaginary part varies, while outside the ring the imaginary part is constant and the real part varies, consistent with Eqs. (4.49) and (4.50).

One of the interesting property of exceptional points is that quasi-statically encircling the exceptional point once, in a three dimensional parameter space $(\Delta, \Omega_r, \Omega_i)$ with either Ω_r or Ω_i fixed, leads to the swapping of eigenvalues. This is due to the fact that instantaneous eigen-basis of non-hermitian systems is not single valued when there is an exceptional point inside the loop[83].

At every fixed value of (Ω_r, Ω_i), H_{nh} has two exceptional points depending on whether $\gamma_2 - \gamma_1$ is positive or negative. The eigenvectors at these two exceptional points are given

by V_{nh}.

$$V_{nh} = \frac{1}{\sqrt{2}} \begin{bmatrix} \pm\frac{(\Omega_i + i\Omega_r)}{\sqrt{\Omega_r^2 + \Omega_i^2}} \\ 1 \end{bmatrix}. \tag{4.51}$$

It has been shown that any real symmetric two-level system will have chiral eigenvalues [80], at the exceptional point, of the form-

$$V_h = \frac{1}{\sqrt{2}} \begin{bmatrix} \pm i \\ 1 \end{bmatrix}, \tag{4.52}$$

We notice that while V_{nh} depends on the ellipticity of the light V_h is independent of that. This parameter independence of the eigenvector is a property of any symmetric non-hermitian two level system. V_{nh} becomes equivalent to V_h when $\Omega_i = 0$ THz as the hamiltonian becomes symmetric in this case.

As mentioned briefly above the relation between phases of the eigenvectors is not rigid in non-hermitian systems. Far from an exceptional point, the states are almost orthogonal but as the states approach the exceptional point they become increasingly linearly dependent and hence their relative phase changes. This property is quantitatively defined by phase-rigidity, (4.17). It measures the ratio of the c-product and inner product of a wavefunction. This ratio can be used to pinpoint the location of exceptional points in a system as it tends to zero as the system approaches the exceptional points. We can see that $r_i = 1$ for hermitian systems. For asymmetric, non-hermitian hamiltonians the left and right eigenvectors are not simply related and so the question of the definition of phase rigidity in such systems arises. The most general way of normalising a basis can be described by

$$\langle \psi_i | \phi_j \rangle = \delta_{ij}, \tag{4.53}$$

where $\langle \psi_i |$ is the left eigenvector and $|\phi_j\rangle$ is the right eigenvector. In the case of hermitian systems, $\langle \psi_i | = \langle \phi_i |$, therefore we conventionally define normalisation as $\langle \phi_i | \phi_j \rangle = \delta_{ij}$. In case of symmetric non-hermitian systems, $\langle \psi_i | = \langle \phi_i^* |$, therefore we define normalisation as $\langle \phi_i^* | \phi_j \rangle = \delta_{ij}$,. In case of asymmetric non-hermitian systems, we don't have either of those conditions mentioned above.

A more general definition of phase rigidity calculated using left and right eigenvectors is

$$r_i = \frac{\langle \psi_i | \phi_i \rangle}{\langle \psi_i^* | \phi_i \rangle}. \tag{4.54}$$

We now compare the two phase rigidity measures (4.17) and (4.54) or H_{nh} and a comparator symmetrized version namely

$$H'_{nh} = \hbar \begin{bmatrix} -i\gamma_1 & |\Omega_r - i\Omega_i| \\ |\Omega_r + i\Omega_i| & \Delta - i\gamma_2 \end{bmatrix}. \tag{4.55}$$

This Hamiltonian has exactly the same energy spectrum as H_{nh} i.e the eigenvalues and EPs are identical in parameter space. As H'_{nh} is symmetric its eigenvectors correspond to V_h in (4.52).

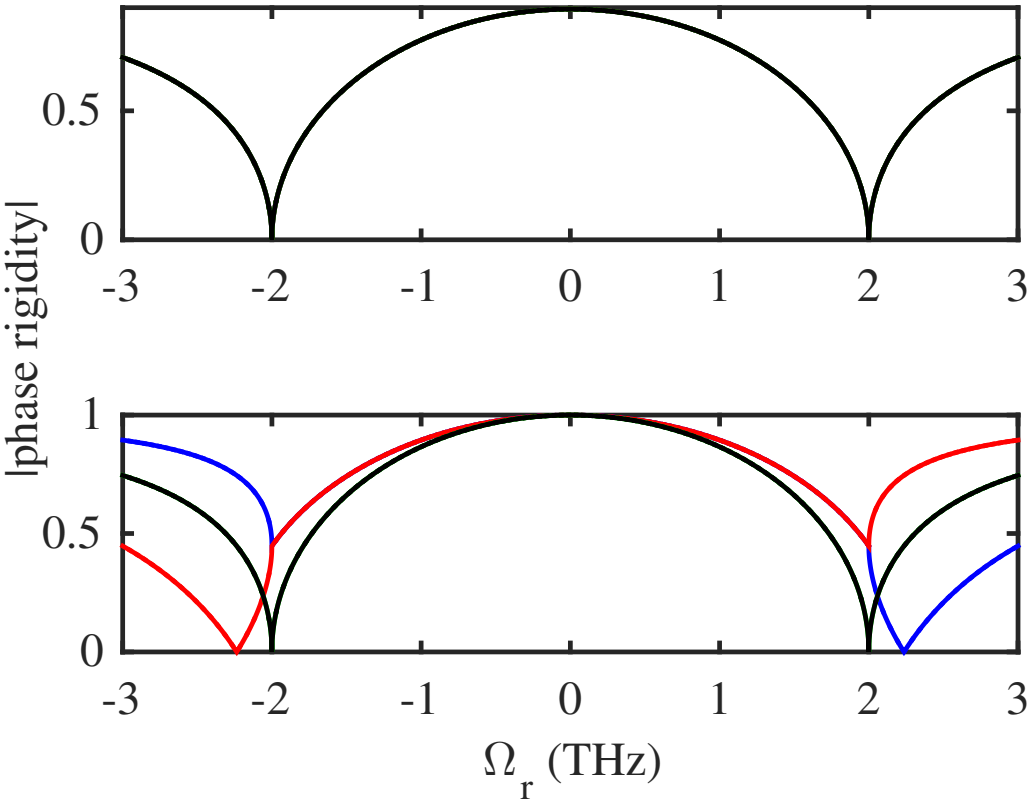

Figure 4.18: The phase-rigidity for H'_{nh} (upper panel) and for H_{nh} (lower panel). Parameters are $\Omega_i = 1\,\text{THz}$, $\gamma_2 = 4.4721\,\text{THz}, \gamma_1 = 0\,\text{THz}$. The exceptional points are at $\Omega_r = \pm 2\,\text{THz}$. The phase-rigidity in red and blue is calculated using each eigenvector using (4.17))). The phase rigidity in black is calculated using bi-orthogonal product definition of phase rigidity ((4.54))). The figure is explained in the text below.

As can be seen in the upper panel of Fig. 4.18, both definitions (as expected) produce identical results for symmetric Hamiltonians with all curves precisely overlapping. In the lower panel, we can see that the bi-orthogonal product definition of phase rigidity ((4.54)) leads to the correct calculation of phase rigidity and thereby correctly identifies EP location at $\Omega_r = \pm 2\,\text{THz}$. In contrast the original definition ((4.17)) leads to an incorrect

identification of EP as well as asymmetry when calculated using each eigenvector. In symmetric case, the phase-rigidity as defined in (4.17) reaches zero when $\Omega_r = \gamma_2/2$ i.e it in effect ignores the contribution of Ω_i thus failing to correctly identify the exceptional points in the system. The asymmetric nature of phase rigidity(blue and red) in the lower panel of Fig. 4.18 is due to the asymmetry of the hamiltonian which leads to different relationships amongst the eigenvectors for parameters in between and outside the exceptional points(± 2 THz). Between the exceptional points the eigenvectors are complex conjugate of each other thus leading to identical measure of phase rigidity. Outside the exceptional point region, the eigenvectors are different and not conjugate pairs which leads to different behaviour on either side of the exceptional points. This problem does not arise for symmetric hamiltonians as can be seen from upper panel in Fig. 4.18. We conclude that the bi-orthogonality-based definition of phase rigidity ((4.17) works well in all cases and is an appropriate metric for the identification of EPs.

4.6 Dynamics

In this section, we present the effects of the exceptional ring on the dynamics and stability of the system.

4.6.1 Comparison between symmetric and asymmetric system

We first compare the dynamics produced by H_{nh} and H'_{nh}, two systems with identical spectra and EPs potentially different dynamics induced by the asymmetric nature of the coupling in H_{nh}. From H'_{nh} we obtain the Bloch equations,

$$\begin{bmatrix} \dot{n}'_1 \\ \dot{n}'_2 \\ \dot{P}'_r \\ \dot{P}'_i \end{bmatrix} = - \begin{bmatrix} 2\gamma_1 & 0 & 0 & 2|\Omega| \\ 0 & 2\gamma_2 & 0 & -2|\Omega| \\ 0 & 0 & \gamma_1+\gamma_2 & \Delta \\ -|\Omega| & |\Omega| & -\Delta & \gamma_1+\gamma_2 \end{bmatrix} \begin{bmatrix} n'_1 \\ n'_2 \\ P'_r \\ P'_i \end{bmatrix}, \tag{4.56}$$

which should be compared to (4.48). We solve the Bloch equations numerically in both cases. The dynamics are shown in Fig. 4.19 and clearly the dynamics of both Hamiltonians is different even though they have the same eigenvalues. The origin of this difference is that the basis states for the two matrices are different even though their eigenspectra are identical. Interestingly, when the initial condition is $[1 \;\; 0]$ or [0 1] i.e if we start with full

population in one of the states the dynamics is same in both cases. The origin of this can be found by comparing the relevant Bloch equations of motion (Eqs. (4.48) and (4.56)) since for such initial conditions the driving terms are (and remain) identical.

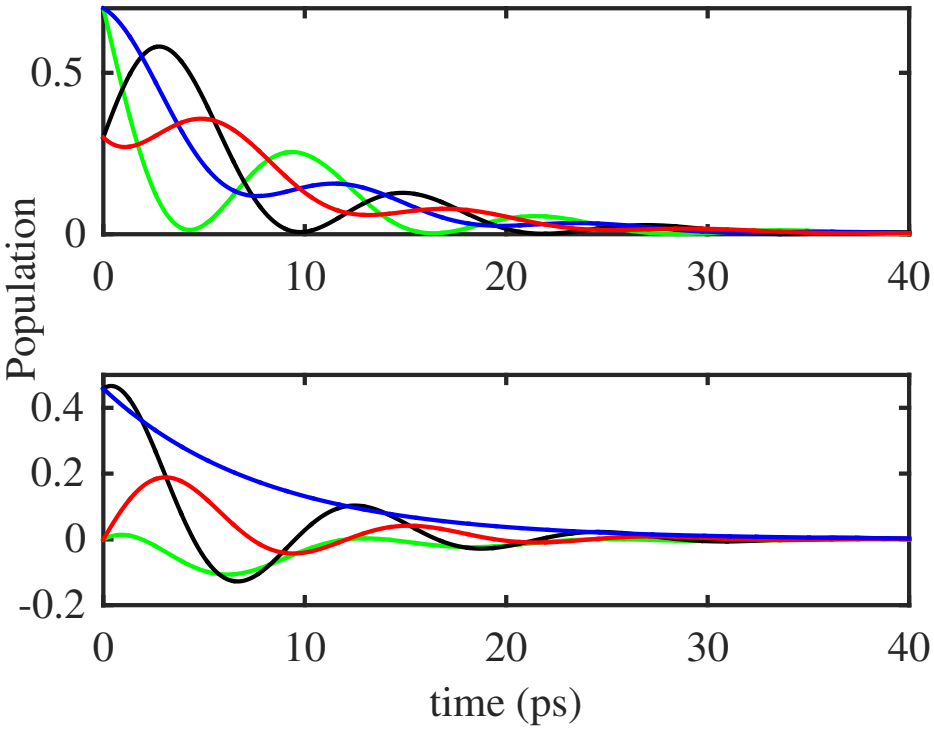

Figure 4.19: Populations and polarisation dynamics obtained from the solution of the Bloch equations for the initial conditions $[n_1 = 0.7, n_2 = 0.3, P_R = 0.4583, P_I = 0]$. The parameters are Δ=0 THz, $\gamma_1 = 0.025$ THz, $\gamma_2 = 0.1$ THz, $\Omega_r = 0.08$ THz and Ω_i=0.25 THz. Blue and red curves are for H'_{nh} while green and black for H_{nh}. Population in ground state (blue, black) and excited state (red, green). Polarisation - real (blue, black) and imaginary (red, green).

4.6.2 Instability ring

In this section we show the existence of an instability ring inside an exceptional ring in an optical gain-loss system. In this ring, however small the gain/loss ratio is, the system always runs away driven by the small gain. This has potential application in systems with high decay rates. We perform linear stability analysis of the Schrödinger equation to find the instability ring in our system. For the non-hermitian Hamiltonian, H_{nh} ((4.47)), expressing the dynamics in the eigenbasis we obtain for the amplitudes C_1 and C_2,

$$\begin{bmatrix} \dot{C}_1 \\ \dot{C}_2 \end{bmatrix} = -i \begin{bmatrix} -i\gamma_1 & \Omega_r - i\Omega_i \\ \Omega_r + i\Omega_i & -i\gamma_2 \end{bmatrix} \begin{bmatrix} C_1 \\ C_2 \end{bmatrix}. \tag{4.57}$$

Since the Schrödinger equation is linear, the Jacobian can be written as

$$J = \begin{bmatrix} -\gamma_1 & -i\Omega_r - \Omega_i \\ -i\Omega_r + \Omega_i & -\gamma_2 \end{bmatrix},$$

and its eigenvalues are

$$\lambda^{\pm} = \frac{-(\gamma_1+\gamma_2)}{2} \pm \frac{\sqrt{(\gamma_2-\gamma_1)^2 - 4(\Omega_r^2+\Omega_i^2)}}{2}. \tag{4.58}$$

For the system to be stable, all the eigenvalues of the Jacobian should be negative. Where at least one of the eigenvalues of the Jacobian is positive, i.e. when

$$\Omega_r^2 + \Omega_i^2 < -\gamma_1\gamma_2, \tag{4.59}$$

the solution will be unstable to small perturbations. For this inequality to be valid, γ_1 and γ_2 must have opposite signs i.e it should be a gain-loss system. So the instability ring exists only in a gain-loss system. This instability ring exists similarly in the symmetric Hamiltonian H'_{nh} with $|\Omega|$ couplings and the stability condition remains the same as the asymmetric case.

Comparing (4.59) with the exceptional ring equality ((4.50)), we can see that the exceptional ring is always larger than the instability ring. Both rings exactly coincide when the system has balanced gain and loss ($\gamma_1 = -\gamma_2$). Fig. 4.20 shows the ground state population (the energy level connected to the sink) of the system inside and outside the instability ring. In this figure, the loss parameter(γ_1) is 10 times greater than the gain parameter(γ_2). The instability ring in this case exists at $\Omega_r = 0.0316\,\text{THz}$. We can see that inside the ring (blue) the state ends up gaining exponentially as time passes while for parameters outside the ring the system decays. We can also see that further we move inside the ring, faster the gain rate is. This can be seen by comparing blue curves in the lower and upper panels. The lower panel shows that the outside the ring the population decays exponentially with time. Here too, the further we move outside the ring, faster the decay is.

Thus even in a case such as this when the decay rate is 10 times larger than the gain rate the system can exhibit a runaway unstable behaviour.

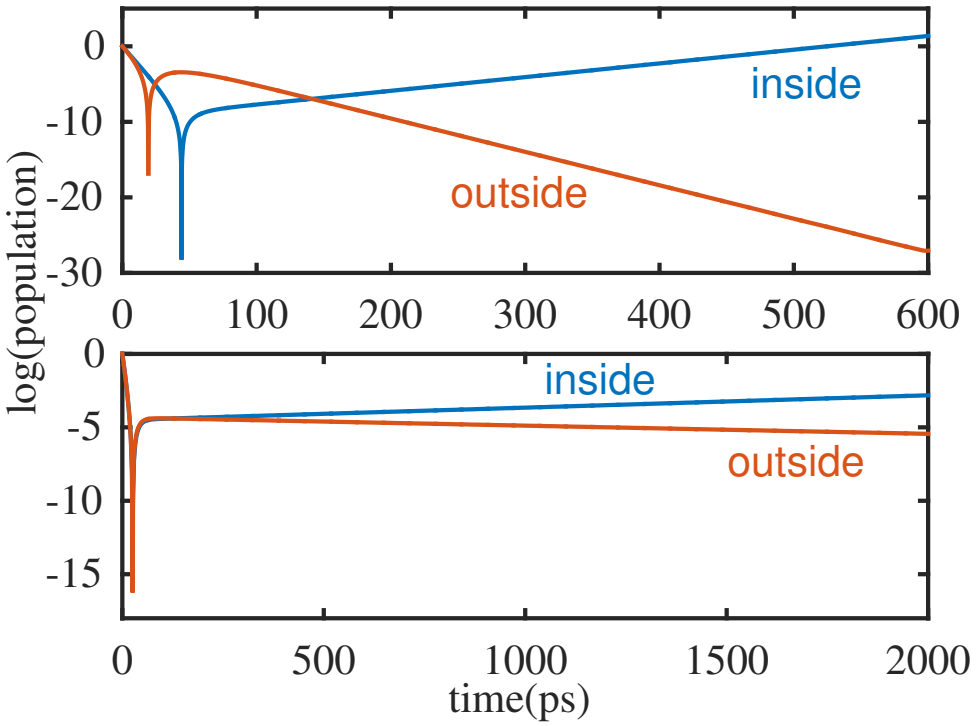

Figure 4.20: Population of ground state with time for a gain-loss system. The parameters are: Initial condition $[C_1 = 1,\ C_2 = 0]$, $\Omega_i = 0.001$ THz, $\gamma_1 = 0.1$ THz,$\gamma_2 = -0.01$ THz. The instability ring is at $\Omega_r = 0.0316$ THz. Upper Panel - far inside the boundary of the stability ring ($\Omega_r = 0.01$ THz) and far outside the ring boundary ($\Omega_r = 0.05$ THz). Lower Panel - close inside the boundary of the ring ($\Omega_r = 0.031$ THz) and just outside the ring ($\Omega_r = 0.032$ THz). Note the difference in time scales in upper and lower panels.

4.7 Experimental validation

This system can be experimentally investigated using a two-level atom and circularly polarised light. Fixing Ω_r and setting $\Delta = 0$ THz, i.e. resonant excitation and varying Ω_i within the exceptional ring (e.g. by changing the intensity of that component) will lead to no changes in the positions of the absorption spectrum peaks as the real parts of the eigenvalues do not change within the exceptional ring (see Fig 4.17). The measured absorption peaks will get broadened however as the imaginary part of the eigenvalues do change within the exceptional ring. So small changes in intensity won't affect the spectrum until a critical value is reached. After that point, further increases will lead to splitting of the peaks peak but no further broadening as the real parts of the eigenvalues split outside the exceptional ring but the imaginary parts there become constant. Whether this is observable obviously depends on finding a system which sharp enough peaks to resolve the splitting. Another experiment might be encircling the exceptional point in Ω_r, Δ space i.e intensity of light and the detuning space. Extracting the eigenvalues from the spectrum

[60] generated by this experiment will show the switching of the eigenvalues.

4.8 Conclusions

We investigated a non-hermitian four level system with first order exceptional point. We simulated some of the known properties if exceptional points in this system and suggested an experiment to observe exceptional points in the atomic spectrum. We then investigated a simple yet rich non-symmetric non-hermitian model system that can be experimentally verified using circularly polarised light interacting with a two level system. We studied properties of phase-rigidity, self-orthonormality and topological properties around the exceptional points. We showed, by comparing with similar symmetric non-hermitian Hamiltonians, that so long as the correct general definition of phase-rigidity is used, it can alway correctly identify the location of EPs. We also described an instability ring inside the exceptional ring where gain always wins regardless of a large loss channel present in the system. This has potential applications in systems with high decay rates because even a small gain can compensate for huge losses in the system thus controlling the dynamics.

Chapter 5

Conclusions and further work

We started with photon echo dynamics in the case of overlapping pulses to control the position and magnitude of the echo to some extent. We have shown that the position and magnitude of the photon echo is highly sensitive to the interference between the two pulses. Therefore, choosing the right parameters will allow the experimentalist a better grasp on the position of the echo and a better signal to noise ratio which would be useful for measuring short T_2 time. Then we collaborated with an experimental group to falsify this hypothesis which resulted in an inconclusive result due to experimental difficulty of observing photon echo in Si:Bi systems.

We also investigated the failure to observe electromagnetically induced transparency in an experiment by our collaborators and suggested the parameter guideline for which the experiment can succeed in future. We showed that the application of short pump in the EIT experiment was the reason for the unsuccessful observation of EIT because long pump and relatively short probe pulses are needed for observation of EIT in three-level V systems. The energy splittings can still be seen with short pump(in population vs probe detuning plots) but that is partly because of the direct pumping due to short pump.

We then investigated lossy systems with non-hermitian quantum mechanics. Firstly, we investigated a lossy three-level Λ system by defining a non-hermitian hamiltonian(where the losses are encoded as imaginary part of the eigenvalues of non-interacting hamiltonian) and reproduced the known results of population variation with time and the coherent population trapping phenomenon. Secondly, we investigated the general properties of exceptional points on a two and four level systems. We proposed an experiment to observe exceptional points in a four-level non-hermitian system. Thirdly we investigated a two level system interacting with circularly polarised light. We modelled this hamiltonian

as a non-symmetric and non-hermitian hamiltonian. We then discovered a region in the parameter space where even a very small gain to loss ratio would result in a higher signal over the course of time i,e, no matter how small the gain is, it always wins. This has potential to be useful in experiments which suffer from low signal to loss ratio or high decay rates.

To conclude, we have investigated various regimes of experimental difficulty in two, three and four level systems and provided potential solutions. to these cases.

There are a few ideas on which to expand this work -

1. Collaboration with an experiment group to check the the existence of the instability ring. In my opinion the experimental validation of existence of instability ring will encourage researchers to experiment on lossy systems in such regime and might lead to interesting physics due to the presence of exceptional points.

2. Studying photon echo in optical gain-loss system inside the instability ring to achieve a higher signal to noise ratio. This will be very useful in the case of high decay rates in the systems. We might get a better signal or the results may even change entirely due to the presence of gain, exceptional points and the instability ring. I think it will be an interesting project as here we'll be connecting the unknown regime of instability rings and less known regime of exceptional points with the well known phenomena of photon echo.

3. A broader project would be the investigation of the effect of exceptional points on the well known optical phenomenas like EIT, photon echo, coherent population trapping, optical sensors, atomic clocks, quantum memories, quantum transport in ordered/disordered systems. etc.

4. Adiabatically encircling an exceptional point in clockwise direction results in the system being in the same eigenstate indifferent to the initial state. The same happens for anticlockwise direction but results in the system being in the other eigenstate irrespective of the initial state. This might be useful in preparing the system in a particular state i.e. initial state preparation.

5. Investigate experimentally known measurable properties of exceptional points such as topological effect around the exceptional points and its potential applications (e.g may define a logic gate(AND/OR/XOR) etc), phase rigidity as well as unknown properties/observable effects of exceptional points on real systems.

References

[1] Rolf Landauer. Irreversibility and heat generation in the computing process. *IBM journal of research and development*, 5(3):183–191, 1961.

[2] Ivan Oliveira, Roberto Sarthour Jr, Tito Bonagamba, Eduardo Azevedo, and Jair CC Freitas. *NMR quantum information processing*. Elsevier, 2011.

[3] Bruce E Kane. A silicon-based nuclear spin quantum computer. *nature*, 393(6681): 133–137, 1998.

[4] Gavin W Morley, Petra Lueders, M Hamed Mohammady, Setrak J Balian, Gabriel Aeppli, Christopher WM Kay, Wayne M Witzel, Gunnar Jeschke, and Tania S Monteiro. Quantum control of hybrid nuclear–electronic qubits. *Nature materials*, 12(2): 103–107, 2013.

[5] Gavin W Morley, Marc Warner, A Marshall Stoneham, P Thornton Greenland, Johan van Tol, Christopher WM Kay, and Gabriel Aeppli. The initialization and manipulation of quantum information stored in silicon by bismuth dopants. *Nature materials*, 9 (9):725–729, 2010.

[6] MH Devoret and RJ Schoelkopf. Superconducting circuits for quantum information: an outlook. *Science*, 339(6124):1169–1174, 2013.

[7] John F Cochran and DE Mapother. Superconducting transition in aluminum. *Physical Review*, 111(1):132, 1958.

[8] Richard E George, Wayne Witzel, H Riemann, NV Abrosimov, N Nötzel, Mike LW Thewalt, and John JL Morton. Electron spin coherence and electron nuclear double resonance of bi donors in natural si. *Physical review letters*, 105(6):067601, 2010.

[9] M Belli, M Fanciulli, and NV Abrosimov. Pulse electron spin resonance investigation

of bismuth-doped silicon: Relaxation and electron spin echo envelope modulation. *Physical Review B*, 83(23):235204, 2011.

[10] Gary Wolfowicz, Stephanie Simmons, Alexei M Tyryshkin, Richard E George, Helge Riemann, Nikolai V Abrosimov, Peter Becker, Hans-Joachim Pohl, Stephen A Lyon, Mike LW Thewalt, et al. Decoherence mechanisms of 209 bi donor electron spins in isotopically pure 28 si. *Physical Review B*, 86(24):245301, 2012.

[11] SJ Balian, MBA Kunze, MH Mohammady, GW Morley, WM Witzel, CWM Kay, and TS Monteiro. Measuring central-spin interaction with a spin bath by pulsed endor: Towards suppression of spin diffusion decoherence. *Physical Review B*, 86 (10):104428, 2012.

[12] Pierre-André Mortemousque, Simon Berger, Takeharu Sekiguchi, Christophe Culan, Robert G Elliman, and Kohei M Itoh. Hyperfine clock transitions of bismuth donors in silicon detected by spin-dependent recombination. *Physical Review B*, 89(15): 155202, 2014.

[13] J Vanier. Atomic clocks based on coherent population trapping: a review. *Applied Physics B*, 81(4):421–442, 2005.

[14] Sungkun Hong, Michael S Grinolds, Linh M Pham, David Le Sage, Lan Luan, Ronald L Walsworth, and Amir Yacoby. Nanoscale magnetometry with nv centers in diamond. *MRS bulletin*, 38(02):155–161, 2013.

[15] Erwin L Hahn. Spin echoes. *Physical Review*, 80(4):580, 1950.

[16] Herman Y Carr and Edward M Purcell. Effects of diffusion on free precession in nuclear magnetic resonance experiments. *Physical review*, 94(3):630, 1954.

[17] Minhaeng Cho, Norbert F Scherer, Graham R Fleming, and Shaul Mukamel. Photon echoes and related four-wave-mixing spectroscopies using phase-locked pulses. *The Journal of Chemical Physics*, 96(8):5618–5629, 1992.

[18] RM Macfarlane, RM Shelby, and RL Shoemaker. Ultrahigh-resolution spectroscopy: Photon echoes in yal o_3:pr^{3+} and la f_3: Pr^{3+}. *Physical Review Letters*, 43(23):1726, 1979.

[19] SA Moiseev and W Tittel. Temporal compression of quantum-information-carrying photons using a photon-echo quantum memory approach. *Physical Review A*, 82(1): 012309, 2010.

[20] Ferenc Mezei. Neutron spin echo: a new concept in polarized thermal neutron techniques. *Zeitschrift für Physik*, 255(2):146–160, 1972.

[21] Saul Meiboom and David Gill. Modified spin-echo method for measuring nuclear relaxation times. *Review of Scientific Instruments*, 29(8):688–691, 1958.

[22] Nicolas Sangouard, Christoph Simon, Mikael Afzelius, and Nicolas Gisin. Analysis of a quantum memory for photons based on controlled reversible inhomogeneous broadening. *Physical Review A*, 75(3):032327, 2007.

[23] Sergey A Moiseev. Photon-echo quantum memory with complete use of natural inhomogeneous broadening. *Physical Review A*, 83(1):012307, 2011.

[24] Alexander I Lvovsky, Barry C Sanders, and Wolfgang Tittel. Optical quantum memory. *Nature photonics*, 3(12):706–714, 2009.

[25] Jérôme Ruggiero, Jean-Louis Le Gouët, Christoph Simon, and Thierry Chanelière. Why the two-pulse photon echo is not a good quantum memory protocol. *Physical Review A*, 79(5):053851, 2009.

[26] Byoung S Ham. Control of photon storage time using phase locking. *Optics express*, 18(2):1704–1713, 2010.

[27] Byoung S Ham. On-demand control of photon echoes far exceeding the spin coherence constraint via coherence swapping between optical and spin transitions. *arXiv preprint arXiv:1010.4870*, 2010.

[28] Morgan P Hedges, Jevon J Longdell, Yongmin Li, and Matthew J Sellars. Efficient quantum memory for light. *Nature*, 465(7301):1052–1056, 2010.

[29] Leslie Allen and Joseph H Eberly. *Optical resonance and two-level atoms*. Dover, 1975.

[30] B N Murdin, Juerong Li, M L Y Pang, E T Bowyer, K L Litvinenko, S K Clowes, H Engelkamp, C R Pidgeon, I Galbraith, NV Abrosimov, et al. Si: P as a laboratory

analogue for hydrogen on high magnetic field white dwarf stars. *Nature Communications*, 4:1469, 2013.

[31] KL Litvinenko, ET Bowyer, PT Greenland, N Stavrias, Juerong Li, R Gwilliam, BJ Villis, G Matmon, MLY Pang, B Redlich, et al. Coherent creation and destruction of orbital wavepackets in si: P with electrical and optical read-out. *Nature communications*, 6, 2015.

[32] Wim P de Boeij, Maxim S Pshenichnikov, and Douwe A Wiersma. Short-time solvation dynamics probed by phase-locked heterodyne detected pump-probe. *Chemical physics letters*, 247(3):264–270, 1995.

[33] Wim P de Boeij, Maxim S Pshenichnikov, and Douwe A Wiersma. Phase-locked heterodyne-detected stimulated photon echo. a unique tool to study solute—solvent interactions. *Chemical physics letters*, 238(1-3):1–8, 1995.

[34] R Yano and H Shinojima. Coherent population control and three-pulse photon echoes: Their dependence on phase of excitation pulse. *Physica B: Condensed Matter*, 407 (2):246–249, 2012.

[35] Leslie Allen and Joseph H Eberly. *Optical resonance and two-level atoms*, volume 28. Courier Corporation, 1987.

[36] Petr M Anisimov, Jonathan P Dowling, and Barry C Sanders. Objectively discerning autler-townes splitting from electromagnetically induced transparency. *Physical review letters*, 107(16):163604, 2011.

[37] L Giner, L Veissier, B Sparkes, AS Sheremet, A Nicolas, OS Mishina, M Scherman, S Burks, I Shomroni, DV Kupriyanov, et al. Experimental investigation of the transition between autler-townes splitting and electromagnetically-induced-transparency models. *Physical Review A*, 87(1):013823, 2013.

[38] Surajit Sen, Tushar Kanti Dey, Mihir Ranjan Nath, and Gautam Gangopadhyay. Comparison of electromagnetically induced transparency in lambda, cascade and vee three-level systems. *Journal of Modern Optics*, 62(3):166–174, 2015.

[39] Hartmut Haug and Stephan W Koch. *Quantum Theory of the Optical and Electronic Properties of Semiconductors: Fivth Edition*. World Scientific Publishing Company, 2009.

[40] Stephen E Harris. Lasers without inversion: Interference of lifetime-broadened resonances. *Physical review letters*, 62(9):1033, 1989.

[41] Bruce W Shore. *Manipulating quantum structures using laser pulses*. Cambridge University Press, 2011.

[42] Carl M Bender. Making sense of non-hermitian hamiltonians. *Reports on Progress in Physics*, 70(6):947, 2007.

[43] Miloslav Znojil et al. Three-hilbert-space formulation of quantum mechanics. *SIGMA. Symmetry, Integrability and Geometry: Methods and Applications*, 5:001, 2009.

[44] Ali Mostafazadeh. Pseudo-hermitian representation of quantum mechanics. *International Journal of Geometric Methods in Modern Physics*, 7(07):1191–1306, 2010.

[45] George Gamow. Zur quantentheorie des atomkernes. *Zeitschrift für Physik A Hadrons and Nuclei*, 51(3):204–212, 1928.

[46] Arnold JF Siegert. On the derivation of the dispersion formula for nuclear reactions. *Physical Review*, 56(8):750, 1939.

[47] I Rotter. A continuum shell model for the open quantum mechanical nuclear system. *Reports on Progress in Physics*, 54(4):635, 1991.

[48] Ingrid Rotter. A non-hermitian hamilton operator and the physics of open quantum systems. *Journal of Physics A: Mathematical and Theoretical*, 42(15):153001, 2009.

[49] Nimrod Moiseyev. *Non-Hermitian quantum mechanics*. Cambridge University Press, 2011.

[50] M Avinun-kalish, M Heiblum, O Zarchin, D Mahalu, and V Umansky. Crossover from'mesoscopic'to'universal'phase for electron transmission in quantum dots. *Nature*, 436(7050):529–533, 2005.

[51] Amnon Aharony and Shingo Katsumoto. Focus on interference in mesoscopic systems. *New Journal of Physics*, 9(5), 2007.

[52] Gregor Hackenbroich. Phase coherent transmission through interacting mesoscopic systems. *Physics Reports*, 343(6):463–538, 2001.

[53] Markus Müller and Ingrid Rotter. Phase lapses in open quantum systems and the non-hermitian hamilton operator. *Physical Review A*, 80(4):042705, 2009.

[54] Hichem Eleuch and Ingrid Rotter. Open quantum systems and dicke superradiance. *The European Physical Journal D*, 68(3):74, 2014.

[55] Robert H Dicke. Coherence in spontaneous radiation processes. *Physical Review*, 93 (1):99, 1954.

[56] Gonzalo A Álvarez, Ernesto P Danieli, Patricia R Levstein, and Horacio M Pastawski. Environmentally induced quantum dynamical phase transition in the spin swapping operation. *Journal of Chemical Physics*, 124(19):194507, 2006.

[57] Horacio M Pastawski. Revisiting the fermi golden rule: Quantum dynamical phase transition as a paradigm shift. *Physica B: Condensed Matter*, 398(2):278–286, 2007.

[58] Konstantin G Zloshchastiev and Alessandro Sergi. Comparison and unification of non-hermitian and lindblad approaches with applications to open quantum optical systems. *Journal of Modern Optics*, 61(16):1298–1308, 2014.

[59] Tosio Kato. *Perturbation theory for linear operators*, volume 132 of *Grundlehren der mathematischen Wissenschaften*. Springer-Verlag, Berlin, 1966.

[60] Holger Cartarius, Jörg Main, and Günter Wunner. Exceptional points in atomic spectra. *Physical review letters*, 99(17):173003, 2007.

[61] Yin Huang, Yuecheng Shen, Changjun Min, and Georgios Veronis. Switching of the direction of reflectionless light propagation at exceptional points in non-pt-symmetric structures using phase-change materials. *Optics express*, 25(22):27283–27297, 2017.

[62] Choloong Hahn, Youngsun Choi, Jae Woong Yoon, Seok Ho Song, Cha Hwan Oh, and Pierre Berini. Observation of exceptional points in reconfigurable non-hermitian vector-field holographic lattices. *Nature communications*, 7:12201, 2016.

[63] Yi-Fan Zhu, Xue-Feng Zhu, Xu-Dong Fan, Bin Liang, Xin-Ye Zou, Jing Yang, and Jian-Chun Cheng. Non-hermitian acoustic metamaterial for the complete control of sound by accessing the exceptional points. *arXiv preprint arXiv:1605.04765*, 2016.

[64] Ming Kang, Weiren Zhu, Hui-Tian Wang, and Malin Premaratne. Spawning a ring of exceptional points from a metamaterial. *Optics express*, 25(15):18265–18273, 2017.

[65] Walter Dieter Heiss and Günter Wunner. Fano-feshbach resonances in two-channel scattering around exceptional points. *The European Physical Journal D*, 68(10):284, 2014.

[66] Soo-Young Lee, Jung-Wan Ryu, Jeong-Bo Shim, Sang-Bum Lee, Sang Wook Kim, and Kyungwon An. Divergent petermann factor of interacting resonances in a stadium-shaped microcavity. *Physical Review A*, 78(1):015805, 2008.

[67] AM Van der Lee, NJ Van Druten, AL Mieremet, MA Van Eijkelenborg, ÅM Lindberg, MP Van Exter, and JP Woerdman. Excess quantum noise due to nonorthogonal polarization modes. *Physical Review Letters*, 79(22):4357, 1997.

[68] B Peng, ŞK Özdemir, S Rotter, H Yilmaz, M Liertzer, F Monifi, CM Bender, F Nori, and L Yang. Loss-induced suppression and revival of lasing. *Science*, 346(6207): 328–332, 2014.

[69] Liang Feng, Zi Jing Wong, Ren-Min Ma, Yuan Wang, and Xiang Zhang. Single-mode laser by parity-time symmetry breaking. *Science*, 346(6212):972–975, 2014.

[70] Hossein Hodaei, Mohammad-Ali Miri, Matthias Heinrich, Demetrios N Christodoulides, and Mercedeh Khajavikhan. Parity-time–symmetric microring lasers. *Science*, 346(6212):975–978, 2014.

[71] H Hodaei, AU Hassan, WE Hayenga, MA Miri, DN Christodoulides, and M Khajavikhan. Dark-state lasers: mode management using exceptional points. *Optics Letters*, 41(13):3049–3052, 2016.

[72] Yong Sun, Wei Tan, Hong-qiang Li, Jensen Li, and Hong Chen. Experimental demonstration of a coherent perfect absorber with pt phase transition. *Physical Review Letters*, 112(14):143903, 2014.

[73] Tamar Goldzak, Alexei A Mailybaev, and Nimrod Moiseyev. Light stops at exceptional points. *Physical review letters*, 120(1):013901, 2018.

[74] A Guo, GJ Salamo, D Duchesne, R Morandotti, M Volatier-Ravat, V Aimez, GA Siviloglou, and DN Christodoulides. Observation of p t-symmetry breaking in complex optical potentials. *Physical Review Letters*, 103(9):093902, 2009.

[75] Zin Lin, Hamidreza Ramezani, Toni Eichelkraut, Tsampikos Kottos, Hui Cao, and Demetrios N Christodoulides. Unidirectional invisibility induced by p t-symmetric periodic structures. *Physical Review Letters*, 106(21):213901, 2011.

[76] Liang Feng, Ye-Long Xu, William S Fegadolli, Ming-Hui Lu, José EB Oliveira, Vilson R Almeida, Yan-Feng Chen, and Axel Scherer. Experimental demonstration of a unidirectional reflectionless parity-time metamaterial at optical frequencies. *Nature materials*, 12(2):108, 2013.

[77] Hichem Eleuch and Ingrid Rotter. Resonances in open quantum systems. *Physical Review A*, 95(2):022117, 2017.

[78] Hichem Eleuch and Ingrid Rotter. Nearby states in non-hermitian quantum systems i: Two states. *The European Physical Journal D*, 69(10):229, 2015.

[79] Dieter Heiss. Mathematical physics: Circling exceptional points. *Nature Physics*, 12 (9):823, 2016.

[80] WD Heiss and HL Harney. The chirality of exceptional points. *The European Physical Journal D-Atomic, Molecular, Optical and Plasma Physics*, 17(2):149–151, 2001.

[81] WD Heiss. Repulsion of resonance states and exceptional points. *Physical Review E*, 61(1):929, 2000.

[82] WD Heiss. Phases of wave functions and level repulsion. *The European Physical Journal D-Atomic, Molecular, Optical and Plasma Physics*, 7(1):1–4, 1999.

[83] Raam Uzdin, Alexei Mailybaev, and Nimrod Moiseyev. On the observability and asymmetry of adiabatic state flips generated by exceptional points. *Journal of Physics A: Mathematical and Theoretical*, 44(43):435302, 2011.

[84] Jan Wiersig. Enhancing the sensitivity of frequency and energy splitting detection by using exceptional points: application to microcavity sensors for single-particle detection. *Physical Review Letters*, 112(20):203901, 2014.

[85] Jan Wiersig. Sensors operating at exceptional points: general theory. *Physical Review A*, 93(3):033809, 2016.

[86] Zhong-Peng Liu, Jing Zhang, Şahin Kaya Özdemir, Bo Peng, Hui Jing, Xin-You Lü, Chun-Wen Li, Lan Yang, Franco Nori, and Yu-xi Liu. Metrology with pt-symmetric

cavities: enhanced sensitivity near the pt-phase transition. *Physical review letters*, 117(11):110802, 2016.

[87] W Langbein. No exceptional precision of exceptional point sensors. *arXiv preprint arXiv:1801.05750*, 2018.

[88] G Slavcheva and Ortwin Hess. Dynamical model of coherent circularly polarized optical pulse interactions with two-level quantum systems. *Physical Review A*, 72(5): 053804, 2005.